Alma Mater Studiorum – Università di Bologna

DOTTORATO DI RICERCA IN

Automotive per una Mobilità Intelligente

Ciclo 34

Settore concorsuale: 09/C1 – MACCHINE E SISTEMI PER L'ENERGIA E L'AMBIENTE

Settore scientifico disciplinare: ING-IND/08 – MACCHINE A FLUIDO

Investigation of innovative combustion systems for reduced fuel consumption and increased specific power production

Presentata da: Guido Federico Scocozza

Coordinatore Dottorato

Prof. Ing. Nicolò Cavina

Supervisore

Prof. Ing. Nicolò Cavina

Esame finale anno 2022

Abstract

This work resumes a wide variety of research activities carried out with the main objective of increasing the efficiency and reducing the fuel consumption of Gasoline Direct Injection engines, especially under high loads. For this purpose, two main innovative technologies have been studied, Water Injection and Low-Pressure Exhaust Gas Recirculation, which help to reduce the temperature of the gases inside the combustion chamber and thus mitigate knock, being this one of the main limiting factors for the efficiency of modern downsized engines that operate at high specific power.

A prototypal Port Water Injection system was developed and extensive experimental work has been carried out, initially to identify the benefits and limitations of this technology. This led to the subsequent development and testing of a combustion controller, which has been implemented on a Rapid Control Prototyping environment, capable of managing water injection to achieve knock mitigation and a more efficient combustion phase.

Regarding Low-Pressure Exhaust Gas Recirculation, a commercial engine that was already equipped with this technology was used to carry out experimental work in a similar fashion to that of water injection. Another prototypal water injection system has been mounted to this second engine, to be able to test both technologies, at first separately to compare them on equal conditions, and secondly together in the search of a possible synergy. In this engine, the exhaust gas cooling effect of both technologies has been analysed and modelled and the main causes of this have been identified.

Additionally, based on experimental data from several engines that have been tested during this study, including both GDI and GCI engines, a real-time model (or virtual sensor) for the estimation of the maximum in-cylinder pressure has been developed and validated. This parameter is of vital importance to determine the speed at which damage occurs on the engine components, and therefore to extract the maximum performance without inducing permanent damages.

Contents

List of Figures

List of abbreviations

AKI	Anti-Knock Index
BDC	Bottom Dead Centre
BMEP	Brake Mean Effective Pressure
BSFC	Brake Specific Fuel Consumption
CA	Crank Angle
CAN	Controller Area Network
CFD	Computational Fluid Dynamics
COV	Coefficient Of Variation
CR	Compression Ratio
DWI	Direct Water Injection
ECU	Engine Control Unit
EGT	Exhaust Gas Temperature
EOI	End Of Injection
GCI	Gasoline Compression Ignition
GDI	Gasoline Direct Injection
HP-EGR	High-Pressure Exhaust Gas Recirculation
HRR	Heat Release Rate
IMEP	Indicated Mean Effective Pressure
ISFC	Indicated Specific Fuel Consumption
IVC	Intake Valve Closing
KLSA	Knock Limited Spark Advance
LP-EGR	Low-Pressure Exhaust Gas Recirculation
MAP	Manifold Absolute Pressure
MAPO	Maximum Amplitude Pressure Oscillation
MBT	Maximum Brake Torque
MFB50	Mass Fraction Burned 50%
NA	Naturally Aspirated
NEDC	New European Driving Cycle
NL	Net Load
OEM	Original Equipment Manufacturer
Pmax	Maximum in-cylinder Pressure

RCP	Rapid Control Prototyping
RMSE	Root Mean Square Error
RON	Research Octane Number
RT	Real Time
SA	Spark Advance
SCR	Selective Catalyst Reduction
SI	Spark Ignition
SOI	Start Of Injection
SiL	Software in the Loop
TPC	Total Percentage Correction
WI	Water Injection
WICC	Water Injection Combustion Controller
WICM	Water Injection Combustion Model
aTDC	after Top Dead Centre
λ	Lambda

Introduction

During the last decades, the development of Internal Combustion Engines in the automotive industry has focused its efforts on reducing pollutant emissions and increasing engine efficiency [1–3]. These goals have been imposed by more and more stringent vehicle homologation regulations, and researchers and OEMs have followed different approaches to guarantee their fulfilment. In the case of Spark Ignition (SI) engines, such goals have been achieved by combining complex aftertreatment systems with several technologies such as downsizing [4], gasoline direct injection [5], turbocharging [6] and variable valve timing [7]. The most common approach has been that of engine downsizing [4–8]. The reduction of engine displacement forces the engine to deliver higher specific-power outputs and operate towards a more efficient region on the fuel consumption map during the homologation cycles. As a matter of fact, smaller turbocharged engines generate a higher Brake Mean Effective Pressure (BMEP) when compared to a Naturally Aspirated (NA) engine for equal torque delivery. Another effective way to improve engine efficiency is to increase compression ratio [9]. In present times, the automotive industry is also heavily investing in the development of fully electric vehicles, but the sudden transition to this alternative powertrain solution might not be as advantageous as expected when considering both economic aspects as well as comprehensive emission reductions [10].

Turbocharged downsized SI engines with high compression ratio represent the most common choice that is able to achieve high efficiency at mid and high loads [11]. This allows for reduced fuel consumption and at the same time greater performance than a NA engine with equivalent displacement [12]. Turbocharged engines present higher in-cylinder pressure when compared to NA engines, contributing to an overall increase in thermal efficiency but the ever-present restraints of knock, pre-ignition, and Exhaust Gas Temperature (EGT) limits are more critical than in the case of a NA engine.

One of the main parameters that influences engine efficiency is combustion phase, which can be represented by the Mass Fraction Burned 50% (MFB50) parameter, which corresponds the crankshaft angle (CA) at which 50% of the total mass of fuel has been burned, and it is typically expressed in terms of CA degrees after Top Dead Center (aTDC). The main engine control parameter that influences MFB50 is Spark Advance (SA), having a direct impact on the angular position of such combustion phase. It is known that an MFB50 of around 8 CA degrees aTDC typically corresponds to maximum energy conversion efficiency, so that the pressure in the cylinder can transfer as much positive work as possible to the piston. The combustion phase that maximizes efficiency corresponds to maximum torque production, and it is often called Maximum Brake Torque (MBT), shown in Figure 0.1, but this is not always achievable because of a pathological combustion mode called knock. Knock is one of the main limiting factors for increasing the combustion efficiency at high load, and it consists in the autoignition of end gases in the unburned region after the spark event, where temperature is high enough to generate self-ignition before they are reached by the flame front initiated by the spark. Knock can cause significant damage to the engine components, as recently demonstrated also by Ceschini et al [13]. Anticipated combustion phases, or close to MBT, generate higher pressure and

temperature in the combustion chamber, leading to higher knock tendencies and thus not making MBT always achievable at high loads. For this reason, a knock limit may be imposed in terms of how close the combustion phase can get to MBT, to prevent knock insurgence and the corresponding damages to the engine components. One of the most common solutions to prevent knock while still achieving high torque production, is to retard the combustion phase and to increase the intake air quantity. This approach may avoid knock damage but typically leads to reaching the EGT limit imposed by the turbine, since a retarded combustion is less efficient, leading to hotter exhaust gases. The region in between these two limits is the allowed operating region, as shown in Figure 0.1. To mitigate knock and lower EGT, the traditional strategy is to operate with values of lambda (λ) lower than one (rich mixture), so that the extra fuel that evaporates after being injected absorbs heat and reduces the combustion chamber temperature. This approach does not require any additional engine components but has a direct impact on fuel consumption and pollutant emissions. Several technologies are being considered to avoid or reduce the need of the traditional mixture enrichment strategy. The most promising solutions are based on the application of cooled Low-Pressure Exhaust Gas Recirculation (LP-EGR) [14–16] and/or Water Injection (WI) [17–20]. LP-EGR consists of the recirculation of exhaust gases extracted after the turbine and reinserted into the intake system before the compressor. In this way, an extra mass of inert gas is added to the cylinder that absorbs heat and helps lower the temperature of combustion gases. WI is based on the same principle of absorbing heat and thus lowering the combustion temperature, but it uses water that is injected into the intake manifold or directly inside the cylinder as a cooling agent. Furthermore, future emissions regulations like Euro 7 will impose the usage of a stoichiometric mixture in the entire operating range, eliminating the possibility of adopting the traditional component-protection approach based on mixture enrichment [21,22]. For this reason, it results imperative to develop substitutive technologies and strategies such as those mentioned above, that work towards the widening of the allowed operation region, to extract higher torque from the engine.
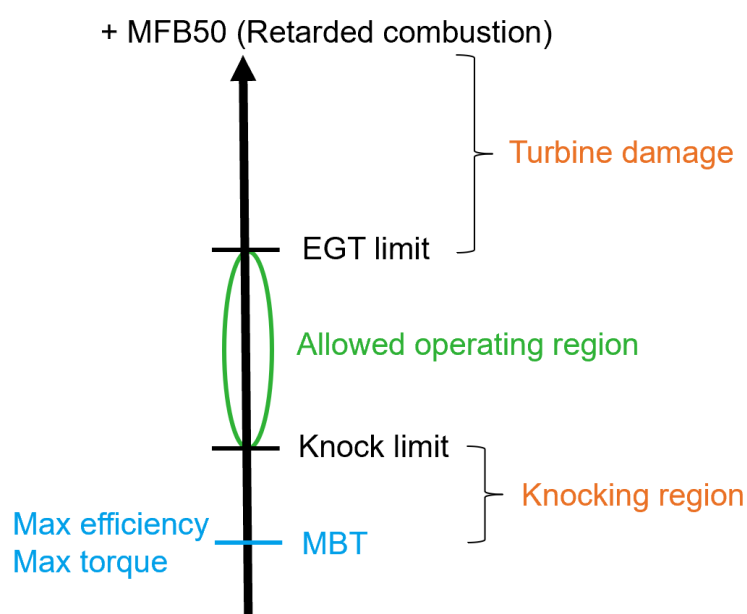
Figure 0.1 - Summary of modern engine's combustion challenges at high loads.

This work focuses on the experimental study of both WI and LP-EGR and the development and implementation of a control strategy capable of managing WI to mitigate knock and achieve a close to MBT combustion phase for increased efficiency. LP-EGR has been investigated as a substitute or complement to WI, while also searching for a synergy between the two technologies. Additional studies regarding the possibility to measure MFB50 with on-board available sensors and the development of a virtual sensor to estimate the maximum in-cylinder pressure have been conducted. The latter is useful to complement the implementation of the WI and LP-EGR solutions towards on-board applications. The dissertation is subdivided into the following chapters:

- *Chapter 1* focuses on the experimental investigation of the main implications of WI on the most relevant combustion parameters, using two different engine setups, a first prototypal one and a second one that is closer to a production application. The development and Real Time (RT) validation of a WI knock control strategy is shown. The second engine possesses both WI and LP-EGR so this setup is mainly used to explore the implications of WI and compare them directly on the same engine to those of LP-EGR.

- *Chapter 2* reports the results from experimental work on the second engine that was used in the previous chapter, to explore the advantages of LP-EGR and its limitations. These results allow for a direct comparison with the results observed when using WI, mainly in terms of how these affect combustion phase and EGT, for which control-oriented models have been developed. Finally, experimental work is carried out in search of a possible synergy between the two technologies.

- *Chapter 3* explores the possibility of utilizing the already on-board available accelerometric signal, typically used for knock detection, for the estimation of MFB50. This is a key study that would fully allow the on-board implementation of the WI knock controller discussed on Chapter 1.

- *Chapter 4* shows the development and broad validation of a virtual sensor for estimating the maximum in-cylinder pressure on several Gasoline Direct Injection (GDI) engines and a Gasoline Compression Ignition (GCI) engine. This model is key to understand the stresses to which the engine components are being subjected when MBT is approached.

1   Water Injection

WI is a technology that has been a subject of study for some time now, but the recent emissions regulations accelerated the need to explore the feasibility of implementing it on production engines. The injection of water inside the combustion chamber (either via port- or direct-injection) leads to a significant delay of the combustion phase and to a mitigation of knock tendency. The degree of these effects is directly related to the injected quantity of water (typically expressed in terms of water-to-fuel mass ratio). As several researchers have discussed [23–27], the explanation is related to the action of water as heat sink inside the combustion chamber, in a similar way as EGR and liquid fuel in presence of rich mixtures. In fact, the gas temperature inside the cylinder can be reduced due to the high enthalpy of vaporization and thermal capacity of water, resulting in a reduction of knock tendency [28]. As a consequence, combustion phase closer to MBT is allowed without incurring in mechanical damages and resulting in higher efficiency. A further benefit is the associated reduction of exhaust gas temperature which helps to avoid mixture enrichment, in other words, the waste of fuel is prevented.

      Khatri et al [1] have studied the benefits of WI in terms of knock suppression and found that, as shown in Figure 1.1, the usage of RON95 fuel plus WI can replace RON98 gasoline, and that a torque increase of up to 6% could be achieved because of the possibility of reaching closer to MBT combustion phase. To be able to reach stoichiometric operation for the different fuels and maximize torque, Khatri had to use water/fuel ratios of up to 0.9, as shown in Table 1.1, observing an increase of combustion duration of up to 12%.
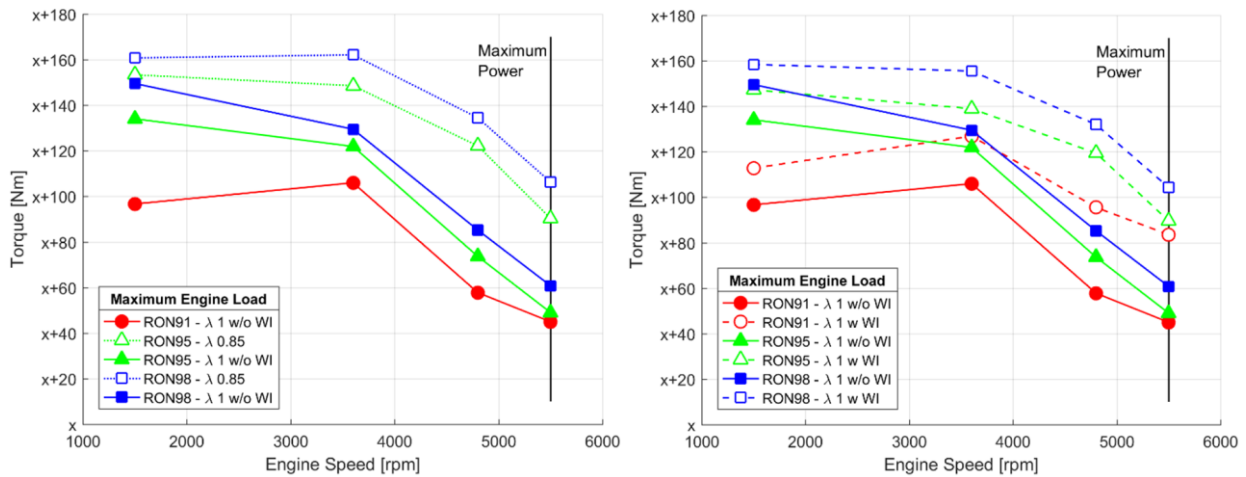
Figure 1.1 - Improvement in engine torque using stoichiometric and non/stoichiometric mixture of RON91, RON95 and RON98 fuels with (w) relative to without (w/o) water injection (WI). Source [1].

Table 1.1 - Water/fuel ratios, expressed as a fraction, to maximize torque for indicated fuels. Source [1].

Engine Speed	W/F Ratio		
	RON91	RON95	RON98
1500	0.84	0.53	0.73
3600	0.54	0.70	0.71
4800	0.87	0.74	0.77
5500	0.89	0.72	0.80
Overall Avg.	0.80	0.67	0.75

Other authors like Thewes et al [29] have combined WI with Miller cycle at high Compression Ratios (CR) of 14.7, achieving an Indicated Specific Fuel Consumption (ISFC) as low as 210g/kWh while also using water/fuel ratios around 0.8. They have also tested this combination in driving cycles, such as the New European Driving Cycle (NEDC), the Worldwide harmonized Light vehicles Test Cycle (WLTC) and the standardized random test RTS95, observing a fuel consumption reduction of 1.49%, 0.94% and 0.92% respectively, when compared to a non-WI alternative, as shown in Figure 1.2. However, during these tests they have seen high water consumption of up to 3.39L/100km which they consider to be excessive for production purposes due to short water refilling intervals and propose to address this with several exhaust water recovery technologies [30–32]. Thewes also suggests that WI can generate even greater benefits when coupled with EGR, for a synergic effect and to help reduce water consumption but does not carry out studies on this topic.
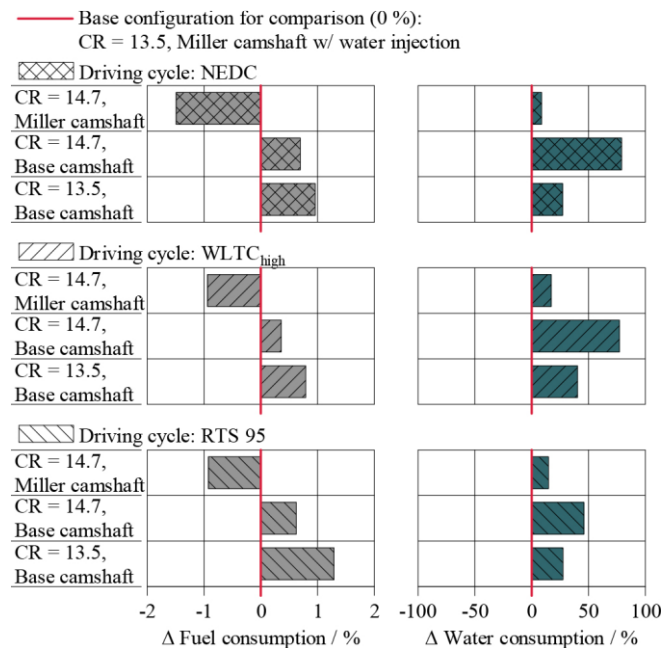
Figure 1.2 - Differences of fuel (left) and water consumption (right) compared to CR = 13.5, Miller camshaft, and water injection. Source [29].

Barros et al [33] have used WI on a GDI engine with the objective of investigating how much net thermal efficiency could be obtained with stoichiometric mixtures at Knock Limited Spark Advance (KLSA) conditions, when compared to a baseline case with non-stoichiometric operation without WI. They have tested the before mentioned conditions with different fuels, each with its own Research Octane Number (RON), that they call Anti Knock Index (AKI). Figure 1.3 shows some of the results obtained by Barros, where net thermal

efficiency has increased from around 25% in the case of the baseline (black line) to close to 34% in the case of the stoichiometric operation with WI at KLSA (red line), in the range between 3000rpm and 4000rpm and full load. At the same time, they have seen that high water/fuel ratios of up to 3 were necessary to obtain the cooling that was needed to ensure such stoichiometric full load operation with an MBT combustion phase (for example the engine point at 2000rpm from Figure 1.3 that required a 200°C EGT cooling, seen in the EGT difference between the red and the blue lines), but they believe that a better atomization of the WI would help reduce water consumption.
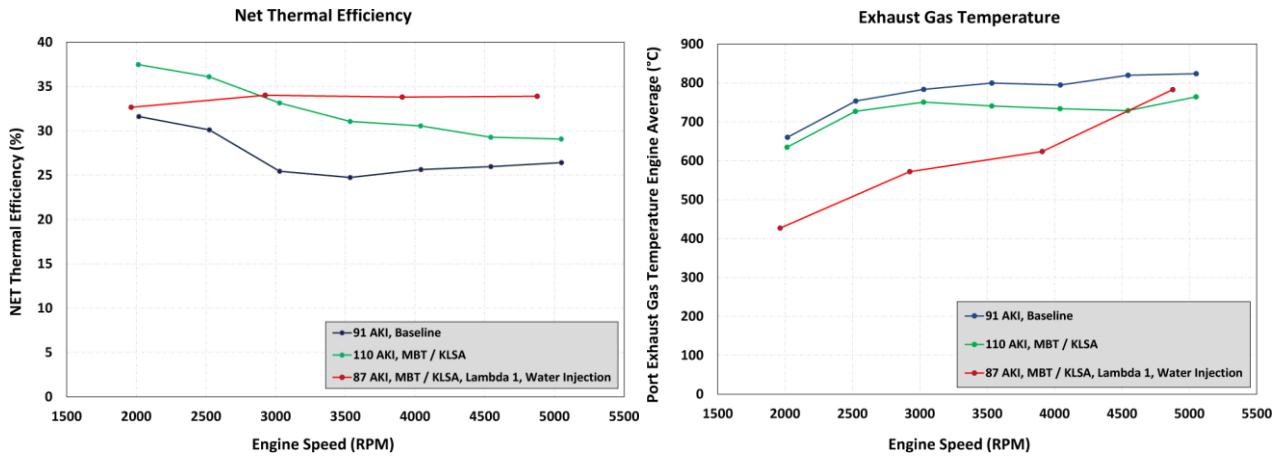
Figure 1.3 - Net Thermal Efficiency and exhaust gas temperature at full load. Source [33].

Iacobacci et al [34] were also able to use WI to mitigate knock and achieve MBT, obtaining an increase in IMEP that ranges from 3% to 7.3% when compared to the reference gasoline case while also observing an EGT cooling between 25°C to 50°C with water/fuel ratios of 0.3. Figure 1.4 shows some of the results obtained by Iacobacci in which it is clear how increasing water/fuel ratio shifts the SA/MFB50 correlation and allows for closer to MBT combustion phase. At the same time, maximum in-cylinder pressure seems to be almost only dependent on MFB50, regardless of the presence of WI.
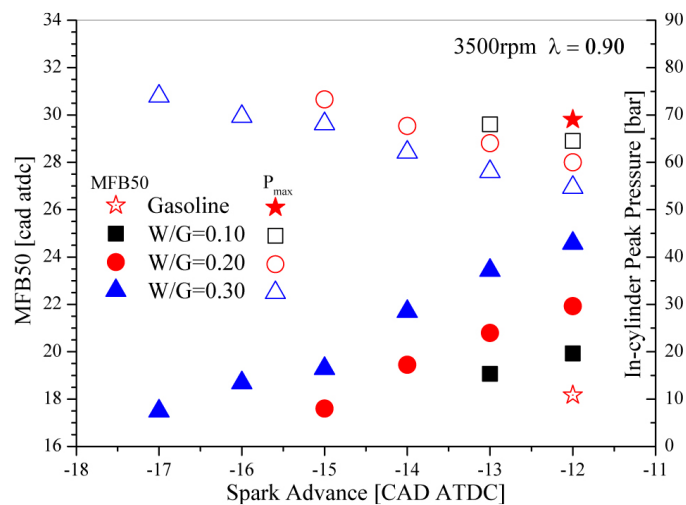
Figure 1.4 - Effects of water injection on combustion phasing and in-cylinder peak pressure at 3500rpm. Source [34].

Cordier et al [19] tested Direct Water Injection (DWI) systems at 100bar on a GDI engine achieving close to 40% efficiency at 2000rpm and 17bar IMEP. Falfari et al [25] have conducted CFD studies to compare Port WI (PWI) to DWI and concluded that given the lower attitude of water to atomize when compared to gasoline, it is key to optimize injection pressure, especially in PWI. They have also underlined that in the case of PWI, injection must occur as close as possible to the intake valve, for water evaporation to occur inside the cylinder as much as possible and achieve a greater gas cooling effect.

WI has been an object of study at the University of Bologna for several years [20,35], in collaboration with the industrial partner Marelli. The author of this work, together with Mr. Ranuzzi and Mr. Brusa, has carried out many experimental campaigns to explore the main implications of a PWI on combustion dynamics [36,37]. Even though DWI can potentially achieve higher benefits than PWI, this latter has been chosen for the WI prototypal setup that was used in this work because the engine modifications that were necessary to implement a DWI system were out of the possibilities of the laboratory of the university. On the other hand, PWI required to build a custom intake manifold to accommodate the water injectors and the presence of a 3D printer at the university made this possible. The main aim of these studies was to understand how the technology could be used to mitigate knock and allow for a combustion phase closer to that of maximum efficiency. As already mentioned, these effects become relevant when the engine operates at high load and high power, therefore WI is a strategic technology when coupled with downsizing and turbocharging in SI engines.

From the results of the authors presented at the beginning of this chapter [1,19,23–29,33,34], the benefits of WI have been well identified, but to take full advantage of the technology for on-board application, it is imperative to develop a control strategy able to manage the water/fuel ratio to obtain the most benefits in terms of efficiency and knock mitigation, while limiting as much as possible the amount of water injected. The novel contribution of this PhD research activity is the development of combustion models capable of predicting the effects of WI and their implementation in a RT control strategy, called WI Combustion Controller (WICC). The WICC was developed and initially tested on a Rapid Control Prototyping (RCP) environment, while always considering the constraints associated to its direct implementation on a production ECU. The most relevant model introduced in this chapter was that used by the controller, capable of calculating the necessary SA angle to obtain the desired MFB50, while accounting for the delaying effects of WI. To achieve these goals a simple approach was proposed, called WI Combustion Model (WICM). The concept of combustion model generally implies algorithms with high level of complexity, such as the ones based on neural networks or multidimensional Computational Fluid Dynamics (CFD), all methods conflicting with RT control constraints [38–43]. The simplicity of WICM is based on its semi-empirical and analytical nature and is a key feature for its implementation on a RT controller. In case of WI, the model is also able to consider the effect of a given water/fuel ratio. Through this configuration a separate management of the water/fuel ratio and MFB50 has been easily implemented, enabling to develop a knock controller that makes use of WI to keep a fixed combustion phasing target.

In the following paragraphs, the potential of the WICC is investigated by an experimental validation on a real engine using a RCP environment. At first, a complete description of the experimental set-up is presented and an overview of the layout of the WICC is provided. Then, the validation of the controller is shown and the performance of the controller in real conditions is discussed. After this, a second engine was equipped with a WI system, being this a prototype with characteristics closer to that of a possible large scale production engine. In this second setup, WI is no longer controlled with the RCP hardware but via a standard Marelli production ECU where the previous WICC had been implemented, reinforcing the concept of close to production approach. Additional experimental campaigns have been carried out on this second engine, leading to a wider understanding of the impact of WI and allowing the author to compare it to the complementary technology that is LP-EGR (discussed in Chapter 2), given that the engine was already equipped with such a system.

The main findings regarding the advantages and limitations of the WI technology are finally described. Most of the results of this part of the dissertation have been published by the author in [35, 36].

1.1   First Prototypal WI engine setup

The first experimental tests were carried out with the scope of identifying the main effects of WI on combustion and developing a WICM and WICC based on a prototype WI system designed at the university. This latter was installed on a commercial 4-cylinder VW TSI turbocharged GDI engine whose main geometric parameters are summarized in Table 1.2. Valve timing has been kept fixed during all the tests that have been carried out on this engine.

Table 1.2 - Main engine specifications.

Displaced volume	1389.9 cc (4 cylinder)
Stroke	75.6 mm
Bore	76.5 mm
Connecting Rod	144 mm
Compression ratio	10:1
Number of Valves	4
Exhaust Valve Open	580° BTDC @0.1 mm lift
Exhaust Valve Close	356° BTDC @0.1 mm lift
Inlet Valve Open	358° BTDC @0.1 mm lift
Inlet Valve Close	132° BTDC @0.1 mm lift

The original engine's intake manifold has been replaced by a prototype 3D printed manifold that was designed specifically to host the PWI system, as shown in Figure 1.5. The water injectors were provided by Marelli and correspond to those used in conventional vehicles for the injection of urea in Selective Catalyst Reduction (SCR) systems. Two water pumps were installed to ensure that the necessary flow was met in all conditions while being able to keep water injection within the duration of the opening of the intake valves. To ensure this, water rail pressure was kept in the range of 10bar to 20bar.
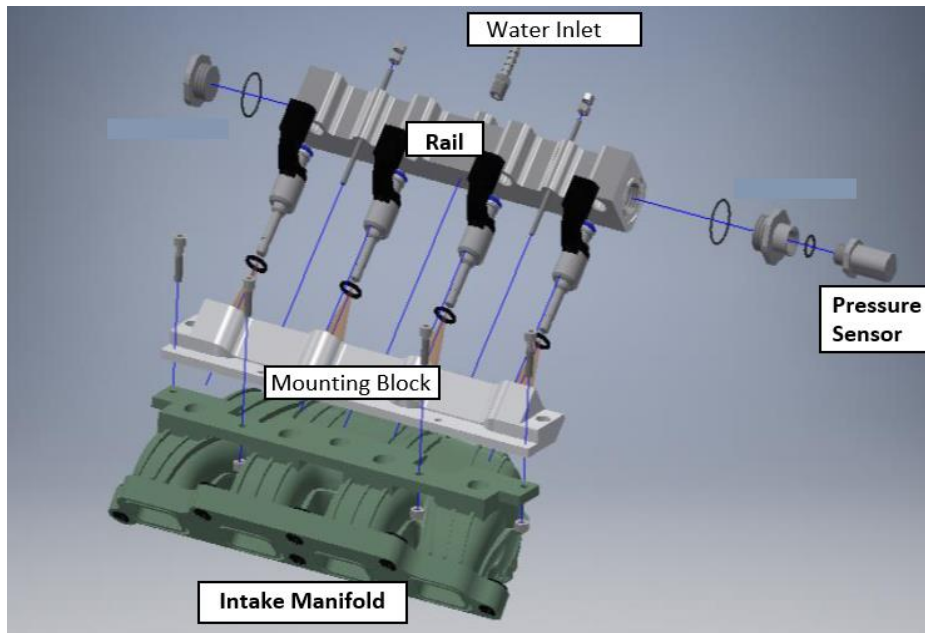
Figure 1.5 - Prototype port water injection system.

The engine was equipped with an in-cylinder pressure sensor for each cylinder and the in-cylinder pressure signal was sampled at 200 kHz. The two main indexes obtained from this signal were the knock intensity and MFB50 angle position. For knock intensity measurement, the Maximum Amplitude Pressure Oscillation (MAPO) index has been considered [44]. MAPO is defined as the maximum amplitude of the oscillations of the filtered in-cylinder pressure signal (for which a high-pass filter with a 5 kHz cut-off frequency has been used) and is calculated as follows:

$$MAPO = max|P_{filt}| \tag{1.1}$$

The statistical knock tendency is quantified by MAPO98. This number represents the value below which 98 percent of MAPO index values are contained, in a sorted set of consecutive combustion events over a buffer of 200 cycles [45–48]. MAPO98 is used (as opposed to using the MAPO value of every cycle) since it allows for the controller to react based on a knock tendency that has been consolidated along those 200 cycles and not just one cycle. Having said this, increasing the number of cycles in the buffer would lead to a more robust assessment of knock intensity but a slower response from the controller, reason why 200 cycles has been chosen for the buffer, as a compromise between robustness and fast response.

An RCP system has then been developed to manage the WI system during calibration campaign and to validate the model-based controller. A simplified scheme is displayed in Figure 1.6. During the tests, all the standard actuators of the engine have been managed by a development ECU. To manage the water injectors a dedicated WI controller has been developed using a RT hardware coupled with the ECU via Controller Area Network (CAN) communication protocols. As already mentioned, the amount of water being injected is typically represented by the water-to-fuel ratio called r and defined as shown in Equation (1.2).

$$r = \frac{m_w}{m_f} \tag{1.2}$$

Where m_w and m_f are the injected water and fuel mass per cycle, respectively. The basic algorithm designed for the RT machine was initially able only to compute the necessary water injection time to achieve the target r value that was externally defined by the test bench operator, as shown in Figure 1.7. To accomplish this goal, the hardware needs as inputs the values of RPM, fuel mass injected cycle-by-cycle and manifold pressure, all provided by the ECU via CAN, water rail pressure, provided by a dedicated sensor, and the desired r value, provided by the test bench system. The algorithm operates cycle-by-cycle for each cylinder trough three steps. At first, the water mass to be injected is defined as the product of fuel mass injected and r. Then, water mass and pressure drop between water rail and manifold are used together with the injector characteristic to define the injection duration. At last, using both engine toothed wheel and phasing signal and considering the Start of Injection (SOI) angle set by the test bench management system, the injection timing is calculated and sent in RT to the Digital/Analogue Converter to drive the port WI system. This is the configuration used during the calibration campaign.
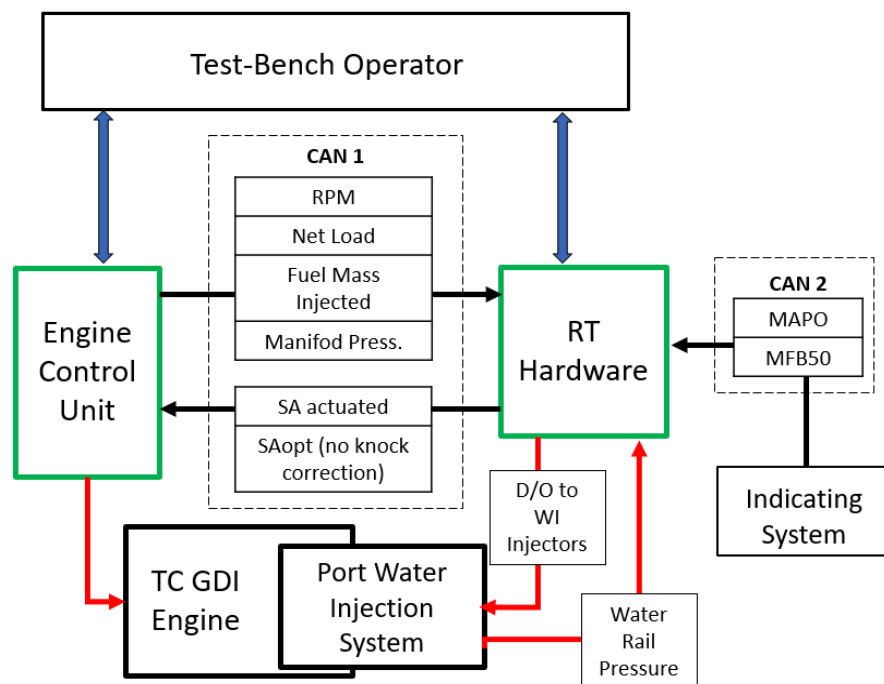
Figure 1.6 - Layout of Rapid Control Prototyping.

21

$$\Delta p = rail\ pressure - manifold\ pressure$$

- RPM
- Phase

ECU → Fuel mass [mg/cycle] → X → Water mass [mg/cycle] → (Injector Characteristic) → Injection duration [ms] → Timing of Injection → DO [V]

Test-bench Management → r target

Start of Injection
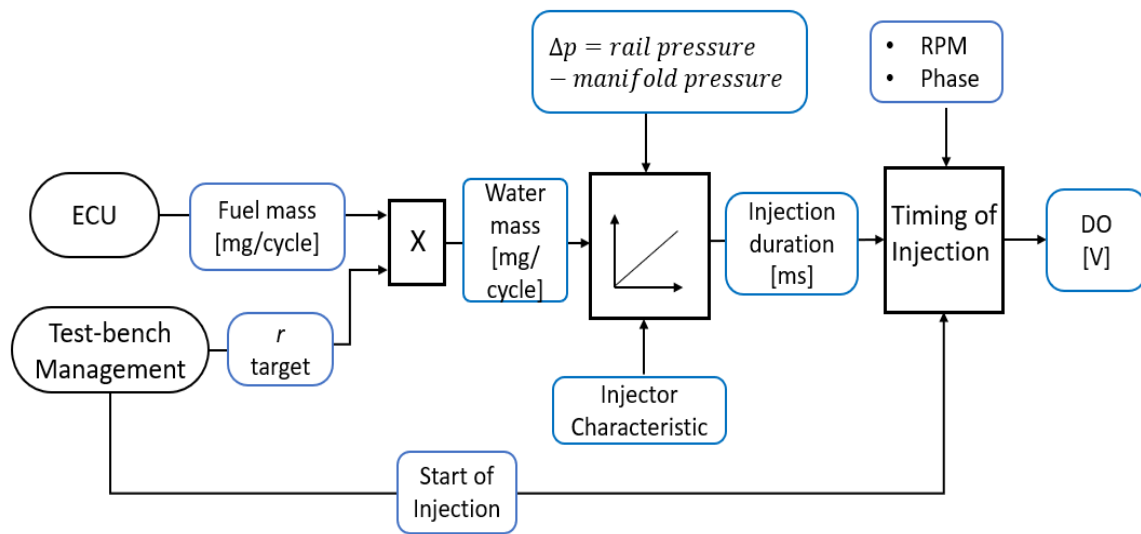
Figure 1.7 - Block diagram of the calculation of parameters involved in the WI system during calibration tests.

To test the WI controller, the algorithm developed in the Software in the Loop (SiL) has then been integrated in the RT code described in the previous section. After this upgrade, the controller calculates cycle-by-cycle the target *r* value and controls the WI system, and at the same time it calculates the new SA value and sends it to the ECU as a target via CAN.

1.2   WI Combustion Model

As stated at the beginning of this chapter, one of the main impacts of WI on combustion is that of generating a combustion delay that retards MFB50 when SA is kept constant. The explanation for this is that the injected water constitutes an extra mass that absorbs heat during combustion and thus lowers the temperature of the gases in the combustion chamber resulting in the reduction of the speed at which the flame propagates. For this reason, it is fundamental to find a way to model this relationship between MFB50 and SA, considering the effects of WI. An analysis on different ways to represent the MFB50/SA correlation has been carried out during this research activity, and a polynomial method demonstrated to be the most accurate and simple one. Figure 1.8 shows experimental data arising from tests on the previously described engine, in which it is clearly shown that there is a shift of the MFB50/SA curves when increasing the *r* value ("rxx" stands for the fraction between water and fuel mass, i.e. "r02" means that a water/fuel ratio of 0.2 has been used), meaning that to achieve a constant value of MFB50 there is the need to increase SA when more water is injected.

During the experimental activity, *r* was limited to a maximum value of 0.8, to limit the water consumption to quantities that may be compatible with on-board operation (either through a dedicated water tank that may be refilled by the user, or by recuperating it from exhaust gases) [29–32]. During the application of the WICC,

this *r* limit has been expanded to 1,1 to allow for the controller to add a maximum of 0.3 beyond the established 0.8 in case it was needed to further mitigate knock.
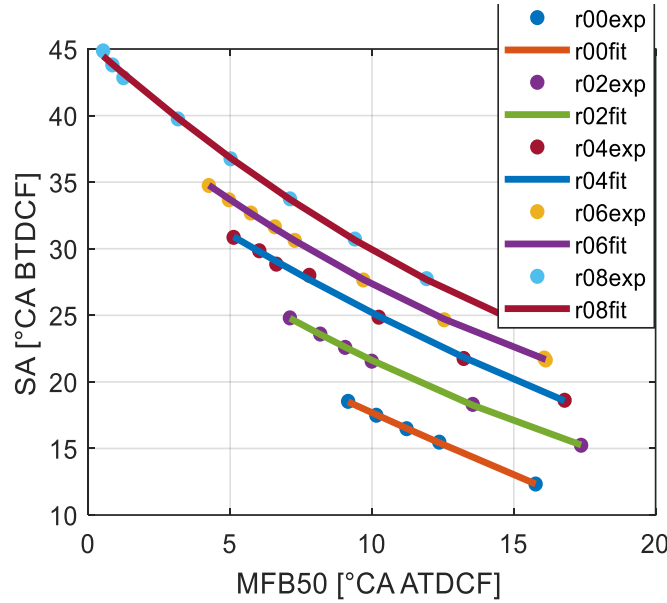
Figure 1.8 - Parabolic relationship between MFB50 and SA, at different values of r at 2500rpm and 1.2Net Load.

It has been verified that the relation between MFB50 and SA corresponds to a parabolic function that is described by Equation (1.3).

$$SA = a\,MFB50^2 + b\,MFB50 + c \tag{1.3}$$

At the same time, it was found that each parabolic coefficient a, b, c may also be expressed as a polynomial function of both RPM and load. Engine load is represented by the variable called Net Load (NL) which is defined by Equation (1.4).

$$NL = pressure_{manifold} * \eta_{intake} \tag{1.4}$$

Where η_{intake} is a factor that considers pressure drop within intake runners and valves. The formula for calculating η_{intake} cannot be disclosed because of confidential reasons. Experimental data show that there is a stronger dependence with RPM than with NL, reason why the polynomial function used to describe each parabolic coefficient a, b and c has finally been represented by Equation (1.5).

$$a = p_{00a} + RPM * p_{10a} + NL * p_{01a} + RPM * NL * p_{11a} + RPM^2 * p_{20a} \tag{1.5}$$
$$b = p_{00b} + RPM * p_{10b} + NL * p_{01b} + RPM * NL * p_{11b} + RPM^2 * p_{20b}$$
$$c = p_{00c} + RPM * p_{10c} + NL * p_{01c} + RPM * NL * p_{11c} + RPM^2 * p_{20c}$$

Where $p_{00}, p_{10}, p_{01}, p_{11}, p_{20}$, are called Surface Coefficients. As previously mentioned, WI has a significant influence on the MFB50/SA correlation, and the effect of *r* into the model is added by describing each surface coefficient p_{xx} as a linear function of water-to-fuel ratio. Equation (1.6) shows this linear function. Figure 1.9 shows the block diagram of the complete WICM with the polynomial method.

23

$$p_{xx} = o_{xx} + r * g_{xx} \qquad (1.6)$$
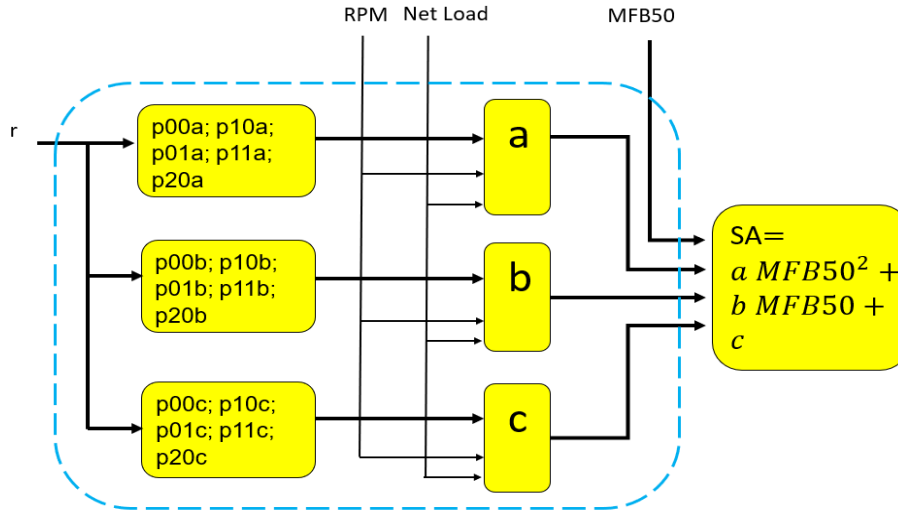
Figure 1.9 - Block diagram of Combustion Model with polynomial method.

This model is a key component of the WICC that is described in the following subsection, because it is the responsible of calculating the SA that should be applied to achieve a desired MFB50 target, to obtain maximum efficiency. To summarize, the inputs of the model are *r*, RPM, NL and MFB50 while the output is the required SA to satisfy the selected MFB50 target. All the inputs are already available as measurements on-board the vehicle, except for MFB50 that in this instance is measured through the in-cylinder pressure sensor, but chapter 4 of this thesis shows the results of a study from the author showing that it is possible to measure combustion phase using the already available accelerometer that is used for knock detection in on-board applications.

1.2.1   WICM calibration

The model required an experimental campaign to calibrate the surface coefficients $p_{00}, p_{10}, p_{01}, p_{11}, p_{20}$ for each parabolic coefficient a, b and c. At the same time, each surface coefficient is defined as a linear function depending on *r*, making a total of 30 coefficients to be determined during calibration. The least squares method has been used to solve the system of equations from which every coefficient of the model is obtained. During the experimental campaign, all the inputs and outputs of the model are recorded, generating a dataset. From each of the entries on the dataset, corresponding to a different configuration of input and output variables, the final system of equations is formed and solved with the least squares method.

During the development of the model, it has been chosen to concentrate the study on mid-high loads, since this is the engine operating region in which the application of WI was more relevant. Figure 1.10 displays

the grid of engine points that have been chosen for calibration and validation, exploring the range between 2500rpm and 4500rpm as regards engine speed, and between 1 and 1.8 NL as regards engine load.
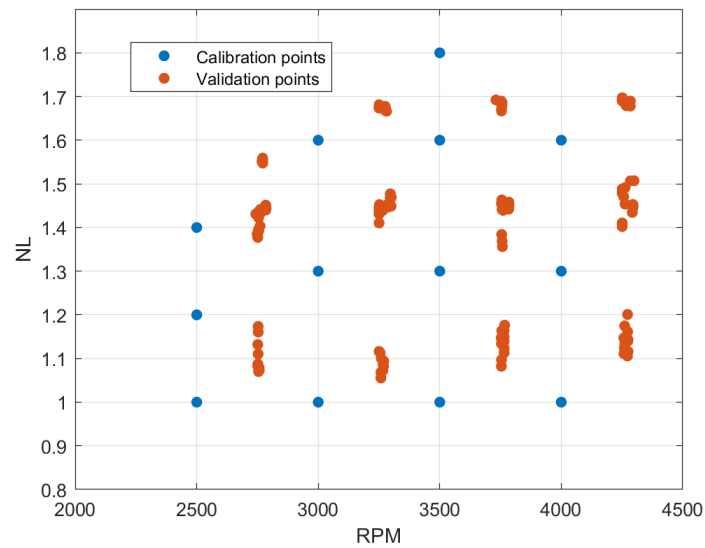
Figure 1.10 - Grid of engine points used for the calibration and validation of the WICM.

For each engine point displayed on Figure 1.10, a sweep of SA and *r* has been performed, like the one shown in Figure 1.8. The measurements that arise from each of the points shown in Figure 1.10 are the result of averaging 5 seconds of cycle-by-cycle data at the desired engine point, and then averaging the data from all four cylinders to obtain a measurement that represents the mean cylinder. This last procedure is done for each calibration and validation engine point. Considering that the objective of the Combustion Controller is to target as close as possible the optimum combustion phase (typically around MFB50 = 8 CA aTDC), if knock does not exceed the established threshold, the SA sweep in each point has been done in the proximity of the optimum MFB50, without surpassing the knock threshold. It has been observed that better calibration results were obtained while using a broader SA sweep with fewer elements inside it instead of a narrow sweep but with a fine step between each point in it. A step of 1.5 CA in SA has thus been used between each element in the SA breakpoints vector. Regarding WI, the values used for calibration vary between $0 \leq r \leq 0.8$ with a step of 0.2. In operating conditions in which it was observed that a certain value of *r* was enough to keep MFB50 at its optimum target value, while still being under the knock threshold, no higher amounts of water were used for calibration given the fact that the WICC would never apply such values of *r* in the open-loop branch.

1.2.2   WICM validation

To validate the model, using the calibration that arises from previously described procedure and with the points shown in Figure 1.10 in blue, SA and *r* sweeps were carried out in engine points that were different than those used for calibration and shown also in Figure 1.10 in red. For this validation, it was chosen to use a grid of points similar to that used for calibration but with an offset of 250rpm and 0.1 NL. This was done so that validation points would be in between the calibration points and not coincide with them, but still remain in the mid-high load region. The red points of Figure 1.10 show that during the experimental tests that were then used for validation, RPM and NL was not kept strictly constant for each point of the beforementioned gid, reason why the grid is made from groupings of points (which constitute the SA and *r* sweeps). The reason for this relies on the fact that a constant RPM and NL was desired during calibration in order to identify the parabolic relationship at each point, as shown in Figure 1.8 as an example, while the validation campaign was aimed to simply validate the model by comparing the measured SA and the estimated SA, as expressed by Equation (1.7). The validation process has been carried out offline, where the SA, *r*, MFB50, RPM and NL values registered on each engine point during the experimental tests were used as input to the model, to finally obtain the SA estimation from it. To quantify the precision of the model, the SA Error is calculated as the difference between the measured SA and the SA estimated by the model.

$$SA\ Error = SA_{measured} - SA_{model} \tag{1.7}$$

Validation results are shown in Figure 1.11 where the dashed lines of the first plot represent the self-imposed precision of ±1 CA when estimating SA, showing that the model could validate most of the engine points within such range. The RT validation of the model is presented in the following section.
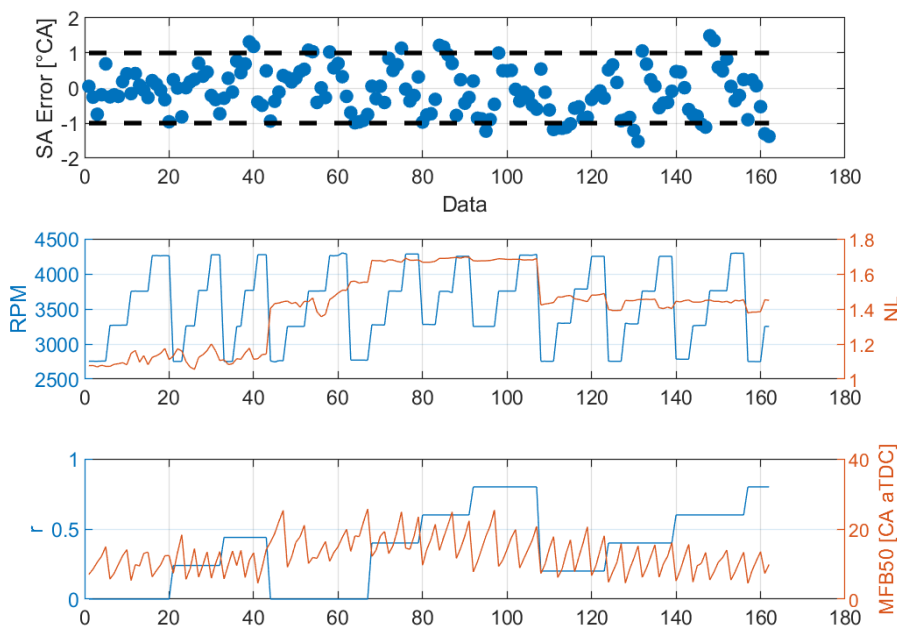
Figure 1.11 – Validation results of the WICM.

26

1.3 WI Combustion Controller

As stated previously, the main aim of the proposed WICC is that of controlling SA and r to achieve a certain MFB50 target that may otherwise not be possible because of knock constraints, thus increasing engine efficiency. The previously introduced model can be used throughout the entire operating range to control in closed-loop the combustion phase, even using WI when necessary to limit the knock intensity. Combustion phase control can therefore be achieved by providing an open-loop action, based on target maps of MFB50 and r, calculated to achieve maximum efficiency in the entire operating range. At the same time, with MFB50 and knock intensity (MAPO) measurements available, the control could be more accurate by adding closed-loop corrections on these. While the knock intensity is always measured on-board, and therefore is always available, as far as the MFB50 is concerned the controller has been developed to be able to add this correction in the case in which the MFB50 measurement is available on-board, as explained in the following paragraphs.

The controller was subdivided into three main parts as described below and shown in Figure 1.12:

- r Map and MFB50 Map are calibrated maps that provide a target value of r and MFB50 depending on RPM and NL.
- The WICM presented in the previous paragraph provides the required SA to obtain the MFB50 target, while considering the effects of r.
- r/SA Correction Management provides correction to the SA value computed by the model and to the r target (respectively called dSAPID and drPID). These corrections are oriented to keep knock index at a pre-defined threshold value (closed-loop on MAPO98), and to target the maximum efficiency combustion phase by achieving the pre-defined MFB50 (closed-loop on MFB50), if such measurement is available on-board.

This approach can effectively allow to manage r and MFB50 as independent variables. In fact, every correction imposed by drPID does not affect the final MFB50 because the WICM can take into account the variation of r and therefore modify accordingly the value of SA to achieve the MFB50 target.
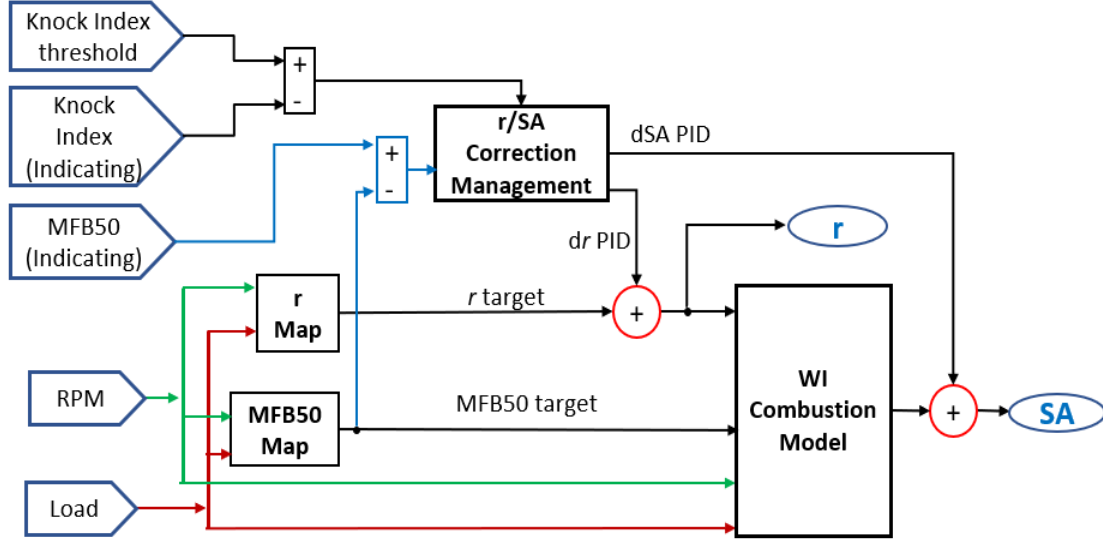
Figure 1.12 - WICC layout.

The MFB50 Map has been set as 8 CA aTDC in the entire operating range since this condition generally represents the maximum efficiency combustion phase and the objective of the controller is to get as close as possible to such condition. The *r* Map has been calibrated with the lowest *r* value that would guarantee the achievement of the desired 8 CA aTDC of combustion phase, while maintaining knock level on the limit of the admissible MAPO98 (MAPO98 threshold). The values of *r* used in this map do not exceed 0.8 because of the previously mentioned on-board application limitations, even though the maximum applicable *r* by the controller is 1.1 because the controller can add an extra 0.3 for additional knock mitigation. The following paragraphs describe in detail the strategy developed for the r/SA correction management.

This subsystem has been developed through two distinct stages. At first, a controller based on knock index has been designed to manage corrections of *r* (d*r*PID) and SA (dSAPID), as shown in Figure 1.13. As mentioned before, d*r*PID is considered by the WICM and therefore it does not affect the resulting MFB50. On the contrary, dSAPID is applied to the SA calculated by the model and can change the combustion phase from the target value (i.e., combustion efficiency may be sacrificed to avoid unacceptable knock levels). The management of d*r*PID and dSAPID is driven by the difference between of the measured knock index level, represented by MAPO98 in this study (but any index available on-board for such purpose may be used), and the corresponding threshold value. Such difference is defined in Equation (1.8).

$$MAPO98\ Error = MAPO98_{measured} - MAPO98_{threshold} \tag{1.8}$$

MAPO98 Error is translated into a proportional and integral correction through a gain scheduling PI structure. The resulting sum of the two contributions is then converted in a percentage value which represents the total amount of the correction also called Total Percentage Correction (TPC) as shown in Figure 1.13. This value is contained within a lower and an upper limit, as shown in the saturation block present in Figure 1.13. The lower limit is set to a negative value chosen so that the controller can reduce *r* and save water in the case

in which the *r* value that arises from the *r* Map is sufficient to guarantee a knock level below the threshold, since a negative TPC would imply negative d*r*PID correction. The upper limit of TPC is used to limit the maximum correction of d*r*PID and dSAPID with the aim to prevent the proportional part of the PI to apply excessive corrections during sudden changes in engine point. The value of TPC defines the way to split d*r*PID and dSAPID actuation according to the following strategy.

If TPC is lower than a calibrated value (HighTPC), MAPO98 is considered close to MAPO98 threshold and thus easily manageable by increasing or decreasing *r*. In this case d*r*PID is used as function of TPC to control knock, keeping dSAPID to 0 in order not to modify the resulting MFB50 and maintain maximum combustion efficiency. To achieve the optimal value of *r* in every condition, d*r*PID should be positive for TPC greater than 0 (meaning that MAPO98 is greater than threshold) and negative for negative TPC (meaning than MAPO98 is below threshold). The second condition is important to reduce the injected water mass when knock level is low enough to allow a reduction of *r* with respect to the open-loop mapped value and reduce water consumption. If TPC is greater than HighTPC, drPID remains fixed to a saturation value (which in this study was set to 0.3) and knock level is controlled by dSAPID that applies negative corrections to retard SA and move actual MFB50 to a delayed position. Furthermore, in case of high knock events on single cycles (MAPOcc) the TPC is forced to a minimum value by momentarily changing the lower saturation of TPC (Low Threshold displayed in Figure 1.13) to a value greater than zero. This strategy guarantees that a minimum correction of d*r*PID will be applied, meaning that it is mandatory for the controller to increase *r* to protect the engine. This is a safety strategy to activate a fast response in case of relevant risk. MAPOcc is also contained within a lower and an upper limit by using a saturation, which is done to prevent the controller from violent corrections that may arise from false measurements of MAPO on single cycles.
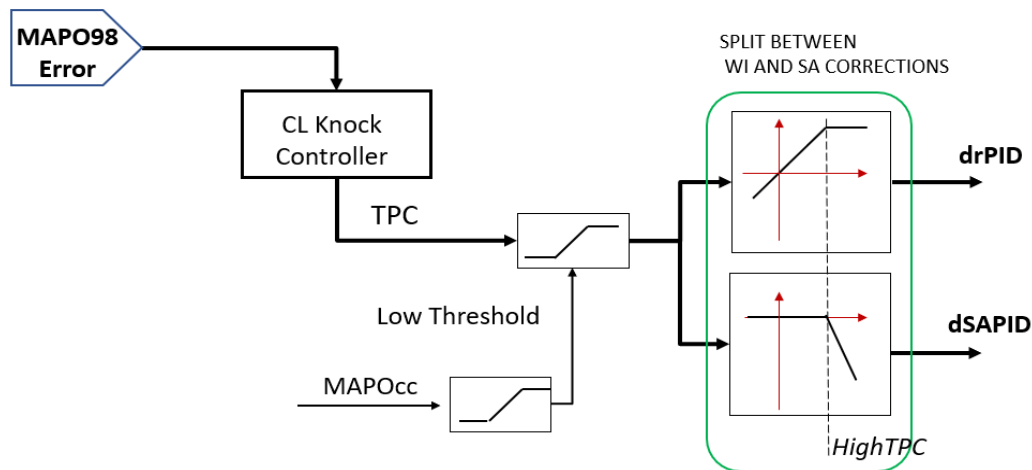
Figure 1.13 – Closed-loop management of r/SA of the knock branch of the WICC.

In a second stage, a new branch has been added in the controller to enable a closed-loop correction based on measured MFB50 values, as shown in Figure 1.14. Like for the case of MAPO98 Error and MAPO98 TPC, a MFB50 Error, shown in Equation (1.9), and a MFB50 TPC have been defined. The MFB50 TPC is

also contained within an lower and an upper limit to prevent the branch from introducing violent corrections during a sudden change in engine point. In this case, the saturations are set to a value so that when converted to dSAPIDmfb a maximum SA correction of ±5 CA can be applied, which should be sufficient given that the objective of this branch is to compensate for the imprecision of the open-loop model that in most cases should be contained within 1 CA. In this configuration dSAPID is the sum of the correction provided by the two branches, respectively defined as dSAPIDknock and dSAPIDmfb. These two terms operate independently, but TPC from knock branch can induce a lower saturation on the MFB50 TPC (Dis_mfbCL), concept that is explained into detail in the following paragraph.

$$MFB50\ Error = MFB50_{measured} - MFB50_{target} \qquad (1.9)$$

As explained previously, if knock level is high enough to produce a TPC that is higher than the High TPC, the SA correction from the knock branch (dSAPID knock) will make negative corrections of SA to retard combustion and lower knock level. Considering the controller layout from Figure 1.14 that includes the closed-loop branch of MFB50, if this last situation is present, when dSAPID knock tends to retard SA and consequently combustion phase, the MFB50 branch would see an increase in MFB50 Error that would conduce dSAPID mfb towards adding SA in order to remain on the MFB50 target imposed by the MFB50 Map. This situation would create a conflict between the two branches in which the knock branch would tend to retard SA to lower knock level while the MFB50 branch would tend to anticipate SA in order to remain on the MFB50 target. To prevent this, a saturation has been introduced in between the two branches in which if the TPC from the knock branch is above the High TPC value, an upper saturation to zero is applied to the MFB50 TPC to prevent this branch from applying any SA corrections and thus interfere with the SA correction that the knock branch applies to lower the knock level. This saturation is done gradually until knock TPC reaches the High TPC value.
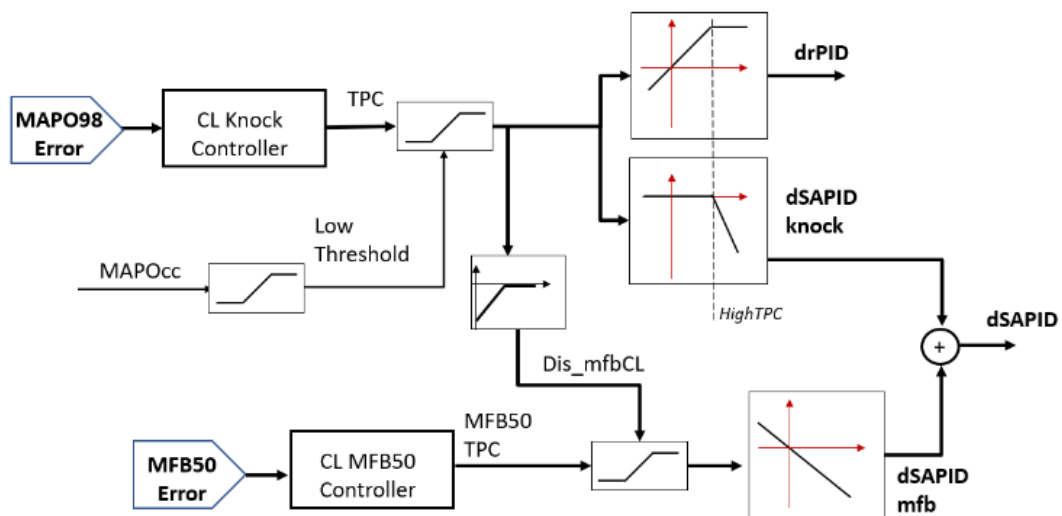
Figure 1.14 - Closed-loop management of r/SA on MAPO98 and MFB50.

1.3.1   WICC real-time validation

The validation of WICC has been carried on evaluating step by step the performance of every part of the whole system that has been described. Engine points different from those used for calibration have been used for validation while remaining inside the perimeter of the calibration region.

1.3.1.1   Open-loop on MFB50

At first, WICC has been tested disabling the entire r/SA correction management subsystem, to highlight the operation of WICM alone and validate its SA estimation in RT. In fact, in this configuration there are no corrections on r and SA and the controller works in total open-loop using just the inversed WICM.

As shown in Figure 1.15, the test is composed by two different stages. At first, from second 10 to second 45, steps of MFB50 target (by manually changing the values of the MFB50 Map) at a fixed value of r ($r$act) equal to 0 were forced. For each step, the model modifies the actuated SA (SAact) accordingly and can produce an actual measured MFB50 (MFB50 meas) close to the target within a range smaller than 1 CA. In the second stage, from second 45 to 75, the MFB50 target is set at a constant value and steps of r are applied. In this case, the model modifies SA to compensate the effect of water injection and the measured MFB50 remains close to the target. This constitutes part of the RT validation of the model, in which it has been observed that the WICM can correctly consider both variations of MFB50 target as well as the usage of WI at different values of r.
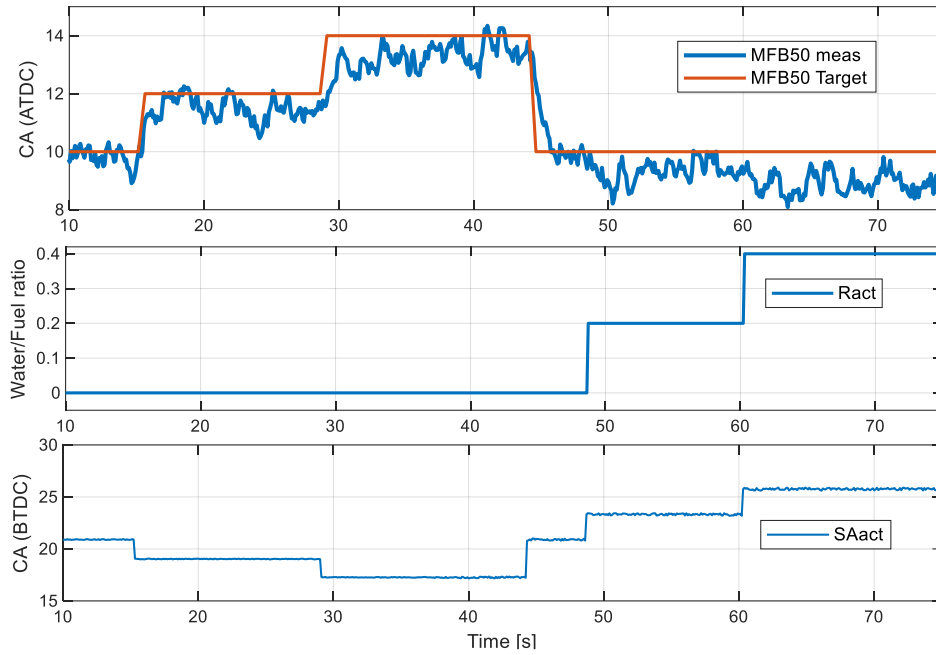
Figure 1.15 - Steady state at 3300rpm, 1.25NL. Cylinder 2 shown as example. The top plot shows the comparison between MFB50 measured and MFB50 target, the middle one presents the value of r actuated, and the bottom plot the SA calculated as model output to achieve the MFB50 target.

1.3.1.2   Closed-loop on MFB50

After the evaluation of model, the closed-loop on MFB50 branch has been tested. The procedure is similar to the previous one because the same steps of MFB50 target and *r* target are imposed, but this time at second 13.5 the MFB50 closed-loop branch is activated as displayed in Figure 1.16. When the closed-loop is activated, dSAmfb starts to apply the correction on SA provided by the model, and SAact becomes the sum of these two terms. From this instant, actual MFB50 is forced to follow the target value. The value of dSAmfb can also be used to evaluate the precision of the WICM in the defining of SA. It can be observed how dSAmfb applies mostly a correction below 1 CA, confirming the results seen on the validation of the open-loop configuration.

32
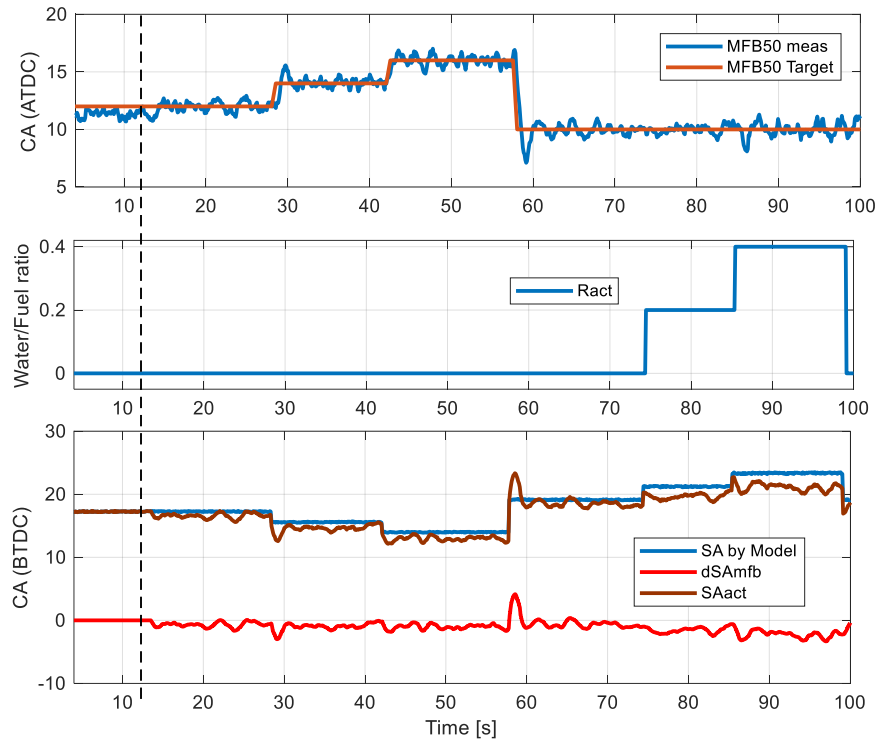
Figure 1.16 - Steady state at 2500rpm, 1.25NL. Cylinder 2 shown as example. At time 0 controller in open-loop. After second 13.5 the controller switches in closed-loop mode and the PI correction dSAmfb compensates the error on MFB50. SAact represents the sum of SAbyModel and dSAmfb.

1.3.1.3   Closed-loop on MFB50 and MAPO98

In the next figures, the behaviour of the closed-loop on r/SA management is displayed. Two different situations are presented, one in which the correction of WI (dr PID) does not saturate, considering a preestablished value of saturation of dr PID = 0.3 (making a total maximum r value of 1.1 which is still compatible with the on-board application limitations associated to water tank refilling), and two others in which it does.

MFB50meas corresponds to a moving average from cycle-by-cycle MFB50 measured angle while MFB50target is the value output by the MFB50 Map. $r$act and $r$map are the final r value actuated and r value obtained from the map, respectively. dr PID is the correction applied by the knock branch of the PID on actuated r, and dr PID sat is the previously mentioned saturation value imposed on the correction of r by the PID. SA act represents the final actuated SA, that is composed of the SA calculated by the WICM (SAmodel) and corrected by both dSAmfb and dSAknock that are the contributions of both closed-loop branches. MAPOcc indicates the cycle-by-cycle value while MAPO98 and MAPO98thr are the calculated 98th percentile and its threshold value, respectively.

Figure 1.17 displays a first test in which the controller operates in pure open-loop until second 18: SA is controlled solely by the model, and WI only by the r obtained from the rMAP. From second 18 onwards, both knock and MFB50 branches of the closed-loop are activated. It can be seen how shortly before activating

33

the closed-loop, knock is generally under threshold and MFB50 is slightly retarded. The response of the knock branch is an initial negative d*r* PID correction to reduce the amount of water injected to save water and have a knock level closer to the threshold, while the MFB50 branch applies positive correction (dSAmfb) to get closer to the MFB50 target, given the previous slightly retarded open-loop response. From there on, both branches continue to keep both knock and MFB50 on their target without saturating the d*r* PID, which keeps the quantity of water injected close to the one set by the *r*MAP. SA calculated by the model follows the trend of *r*act since it considers the effects of *r*, as previously clarified.
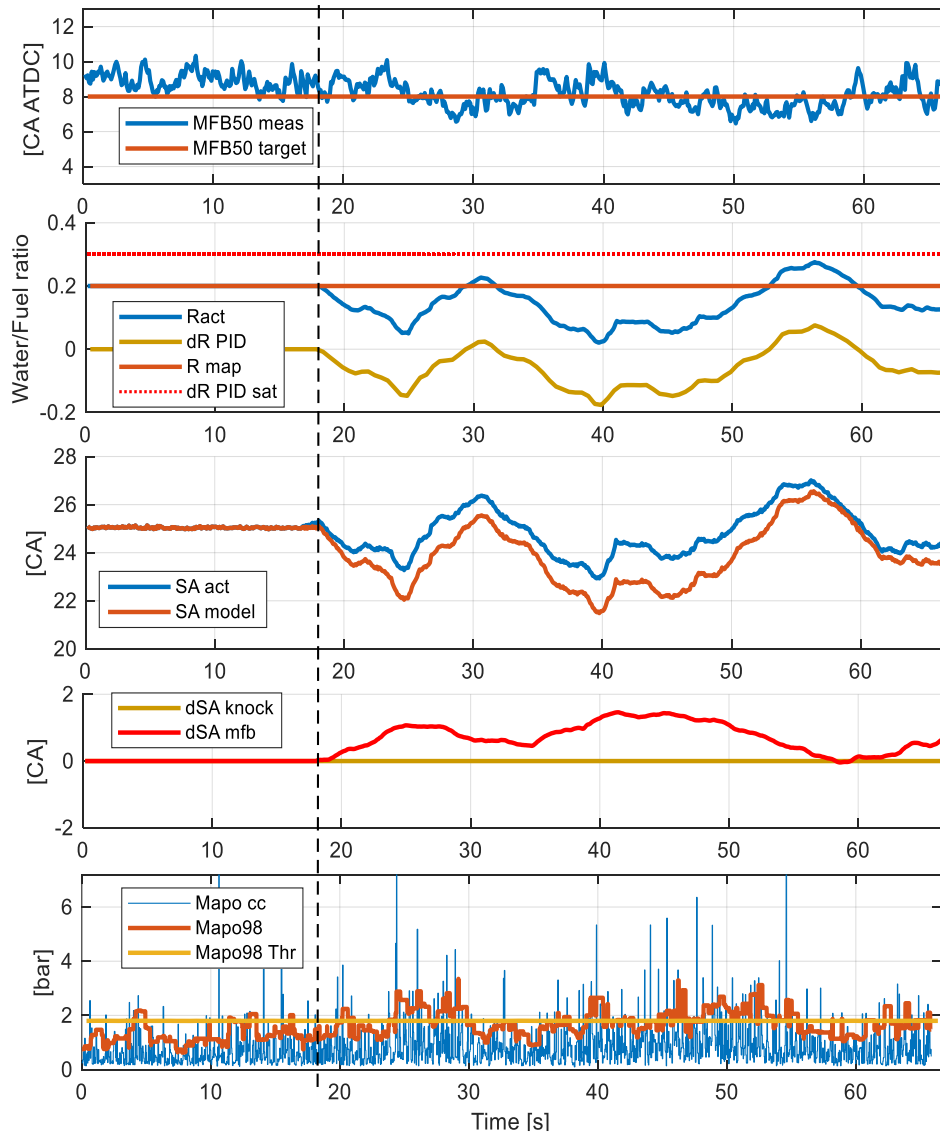
Figure 1.17 - Steady state at 2700rpm, 1.22NL. Cylinder 1 as an example. At second 18 the controller switches from open-loop to closed-loop: dSAmfb starts to compensate the CA50MFB error (as seen in Figure 1.16) and correction dR PID compensates R map (mapped value of r) to reduce the amount of injected water while respecting the MAPO98 threshold (Mapo98 Thr).

Figure 1.18 displays a second situation in which both closed-loop corrections are active from the start of the test. At second 13, a sudden change in MFB50 target is imposed to generate a high knock intensity with the intention of stimulating a response of the controller's knock branch. After second 13, SA changes instantly due to the model's reaction to the MFB50 target change, MFB50 is anticipated and knock level increases. The

34

knock branch reacts to lower knock by adding water, and quickly saturates at dr PID = 0.3. Due to the saturation of the dr PID contribution, the MFB50 branch is not allowed to add positive contributions to SA that would otherwise increase the knock level. From the moment in which dr PID saturates, the SA calculated by the WICM remains constant due to a constant MFB50 target and r map, given dr PID saturation, and the SA correction from the knock branch (dSAknock) starts to retard combustion until MAPO98 is lowered to respect the corresponding threshold. A delay of MFB50 with respect to the target is then generated, due to the priority to maintain MAPO98 at threshold.
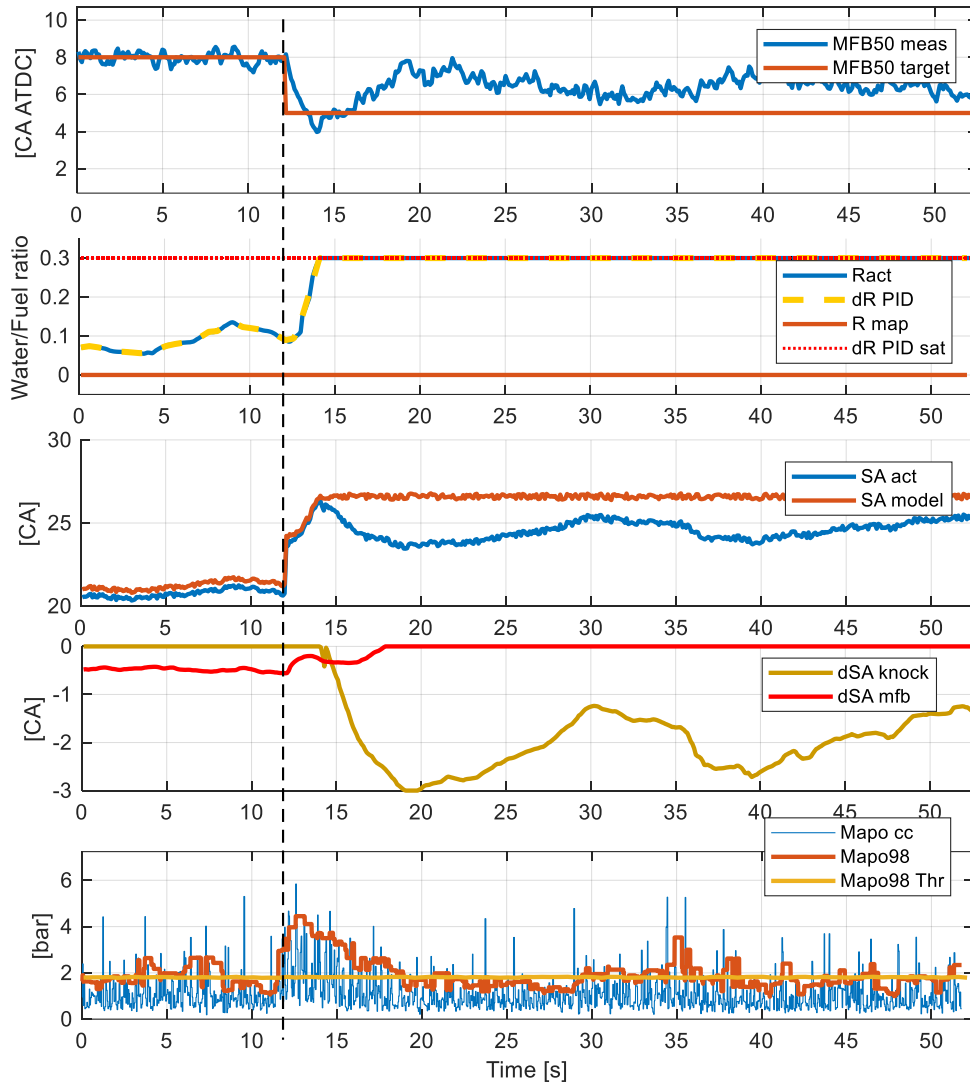
Figure 1.18 - Steady state at 2700rpm, 1.22NL. Cylinder 1 as an example. The controller is in closed-loop. After second 13 MFB50 target is forced to an advanced value to stimulate high knock tendency. After 2 seconds dR PID, attempting to compensate Ract, reaches saturation value (dR PID sat). After saturation, dSA mfb is limited to negative values and dSAknock starts to apply corrections on SAact to limit knock intensity, delaying MFB50.

Figure 1.19 presents a third situation in which the mapped value of r has been lowered with respect to the calibrated one to obtain a higher knock level, over the threshold of MAPO98. In this test the MFB50 branch is activated from the beginning and at second 35 also the knock CL branch is activated as well. This test proves that the knock branch can quickly lower MAPO98 to threshold when being activated in an over threshold

situation. In this case, after d*r* PID saturation around second 38, MFB50 can still be close to target since the amount of water injected at saturation is almost just enough to keep MAPO98 at threshold. This is also the reason why corrections of dSA knock are also small, less than 2 CA.
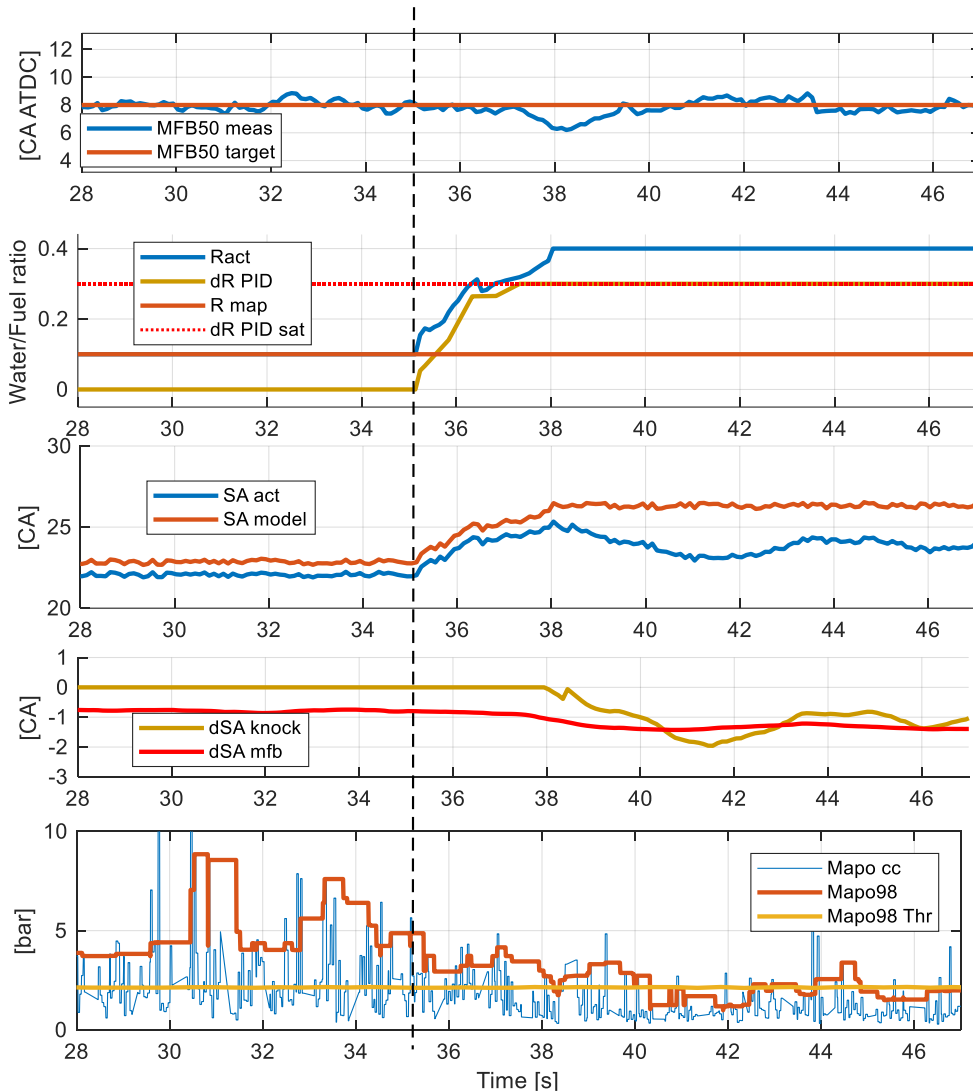
Figure 1.19 - Steady state at 3200rpm, 1.3NL. Cylinder 4 as an example. At time 0, the controller is in closed-loop only for MFB50 and knock index exceeds the threshold value. After second 38 even loop on Mapo98 is closed.

1.3.1.4   Controller response under transient conditions

To further explore the capabilities of the WICC, a transient situation was tested, reproducing a real situation in which there is a sudden change of load, and RPM increase gradually, as displayed in Figure 1.20. This can easily represent a real situation of a highway overtaking, in which the driver presses the accelerator pedal and the car gradually accelerates while RPM increase.
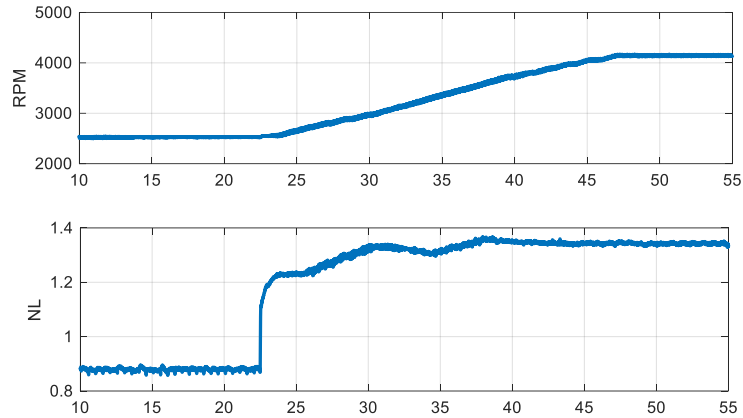
Figure 1.20 - Transient profile regarding engine speed and load.

Figure 1.21 displays how the controller can manage knock levels at MAPO98 threshold also under fast transient conditions. *r* map changes over time due to the everchanging engine point, and the knock branch does not saturate at any moment due to a well calibrated *r* MAP. d*r* PID adds corrections that keep *r* values close to mapped ones. This can also be noted by the fact that when the sudden change in load is applied, MAPO98 still stays at threshold and does not go over it, demonstrating the capabilities of the open-loop. Closed-loop works as it should, making small adjustments to keep MAPO98 and MFB50 at target, being mostly a result of the integral part of both branches of the PID.
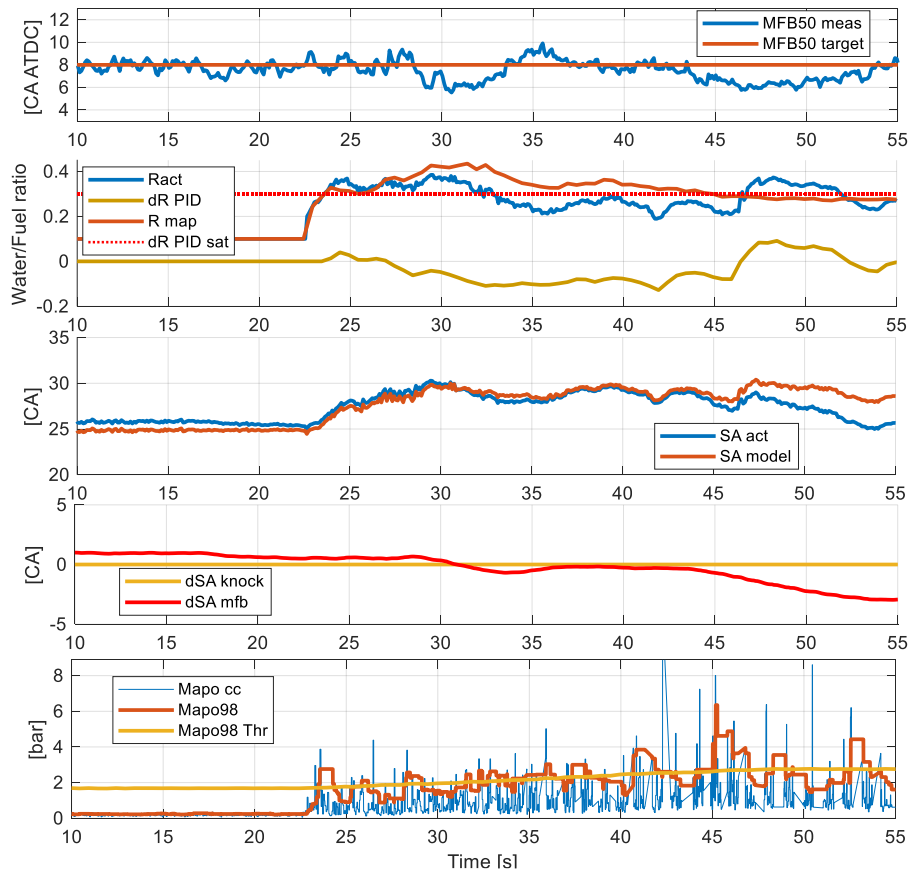
Figure 1.21 - Response of the WICC to the transient test. Cylinder 1 is shown as an example.

1.3.1.5   Analysis of the benefits on fuel consumption

The performance of the Combustion Controller can be also quantified in terms of fuel consumption savings. WI is utilized to mitigate knock while allowing for greater values of SA. When not using WI, it is necessary to enrich the mixture to achieve these same goals, with the inevitable associated increase in fuel consumption.

To evaluate this fuel consumption difference, two tests were made, one with WI and another without. Both tests were conducted at 2700rpm and 1.45 NL. In the case of WI, a value of $r = 0.8$ was used to mitigate knock as much as possible and SA was set so that MFB50 was as close as possible to the optimal value of 8 CA aTDC, while remaining below an established MAPO98 limit value of 2 bar. The test without WI was conducted with the base calibration of the engine which uses a similar principle, in which λ and SA are calibrated to keep the combustion phase as close as possible to optimal MFB50, while guaranteeing knock intensity below the 2 bar MAPO98 limit.

The results are summarized in Table 1.3. and it can be observed how the tests with WI present an improvement in fuel consumption of about 16% compared to the tests without WI, given mainly by the difference in λ and the achievement of a more efficient combustion phase.

Table 1.3 - Fuel consumption of test with WI and without WI at 2700rpm, 1.45NL.

	With WI	Without WI
Water / Fuel ratio (*r*)	0.8	0
MFB50 [CA ATDC]	12	18
MAPO98 [bar]	1.9	2
Lambda	1	0.89
EGT [°C]	786	818
Indicated Torque [Nm]	185	187
Fuel Consumption [kg/h]	11.3	13.5
Indicated Specific Fuel Consumption [g/kWh]	216	257

1.4   Second WI engine setup

As exposed in the previous sections, the engine with the first prototypal WI setup was used mainly for the development of both the WICM and WICC. With the objective of applying the WI technology and the WICC towards a more on-board oriented application, the industrial partner Marelli developed a WI system that was mounted on a different engine that was completely controlled by an OEM ECU without the need of the RCP. The setup was made in a way that all the components used were commercially available and eventually ready for an on-board application, remaining as an economically plausible solution in case of becoming a system ready for large scale production.

This second engine has been used mainly for the further investigation of the effects and drawbacks of WI on a close to production setup (less prototypal) and to compare these to those of the alternative technology of LP-EGR that was already part of the OEM equipment of the engine to which this WI system was added. This second engine was a 2L turbocharged GDI engine whose main characteristics are summarized in Table 1.4.

Table 1.4 - Main characteristics of the engine used on the second WI setup

Engine displacement	1995 cc
Number of cylinders	4
Bore	84 mm
Stroke	90 mm
Compression ratio	10:1
Number of valves per cylinder	4

The equipment used for the indicating measurements was similar to that of the first engine, using in-cylinder piezoelectric pressure sensors in each cylinder, and the pressure signals were acquired at a frequency of 200kHz using AVL's IndiCom indicating system. The pressure signal was used for the calculation of the main combustion indexes such as MAPO, MFB50, IMEP, maximum in-cylinder pressure (Pmax), among others. Brake Specific Fuel Consumption (BSFC) has also been measured, for which an AVL fuel balance was used to measure fuel flow.

Figure 1.22 shows a simplified scheme of the experimental setup with the main sensors and actuators used on this second engine. For the determination of the EGT, a thermocouple has been installed in the exhaust manifold before the turbine inlet. An oxygen sensor mounted before the catalyst was used for λ measurement and mixture control. A second oxygen sensor was mounted on the intake manifold, used for the determination of the EGR ratio, concept that is described more into detail in the following chapter that discusses LP-EGR and the experimental tests carried out on this engine to explore such technology. As regards the WI system, it consists of a port WI configuration with individual injectors for each intake runner. A water rail pressure of 7 bar was utilized and an End Of Injection (EOI) angle coinciding with the Bottom Dead Centre (BDC) of start

of compression was fixed for all engine points, ensuring that the injection of water does not continue after Intake Valve Closing (IVC). WI was controlled by an auxiliary ECU (still OEM) that was used to manage the system actuators such as water pump, water rail pressure regulator and water injectors. This secondary ECU communicates with the main engine ECU via CAN and the amount of water to be injected was modified using INCA software. To verify that the *r* ratio is being correctly estimated and applied by the ECU, a separate AVL balance was used to measure water consumption and the ratio between fuel and water consumption finally determines the measured *r*.
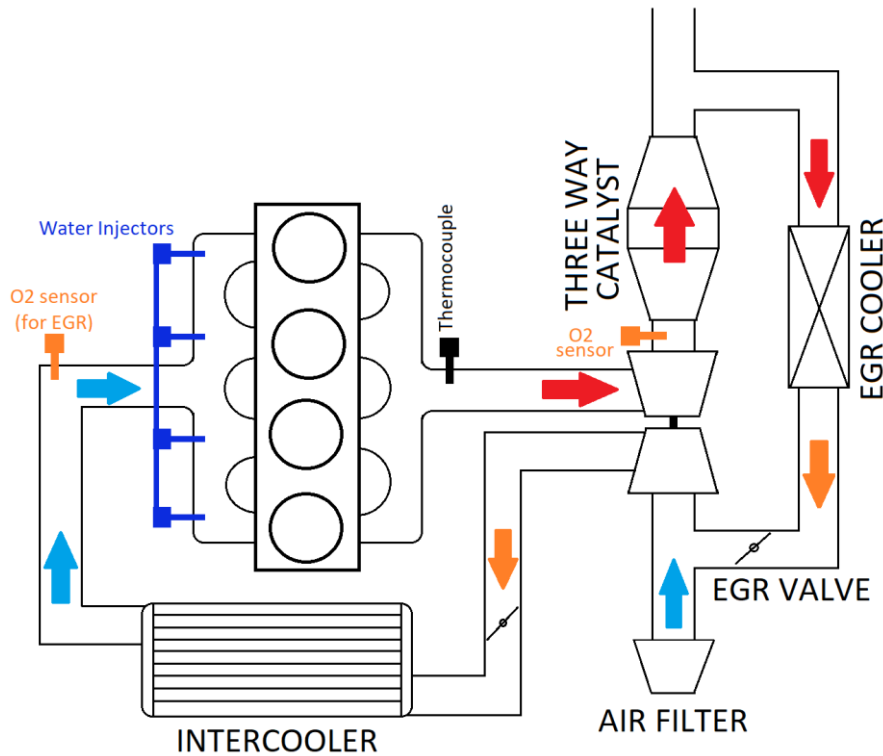
Figure 1.22 - Scheme of the second engine containing both a WI and LP-EGR system.

Three separate experimental campaigns were carried out on this engine: one applying only WI and another one only EGR, selecting a subset of the same engine points to be able to compare their effects. The third test was carried out in one specific engine point in which both EGR and WI were utilized simultaneously to explore a possible synergy between these two technologies. Figure 1.23 shows the grid of engine points explored during each experimental campaign. For each point, an EGR sweep was performed in the case of EGR usage, and an *r* sweep in the case of WI tests. All EGR tests contain a sweep ranging from 0 to 0.12 EGR while WI tests contain a *r* sweep that tends to lower values at low loads and higher values at high loads. For each EGR or *r* value, a further SA sub-sweep was carried out. This allows to model the main combustion parameters as a function of MFB50 for different values of EGR and *r*, as explained on the following section. Finally, for each engine point, a knock limit was defined in terms of maximum MAPO percentile value not to be exceeded and the SA that generates such knock limit percentile value is called knock limited SA.
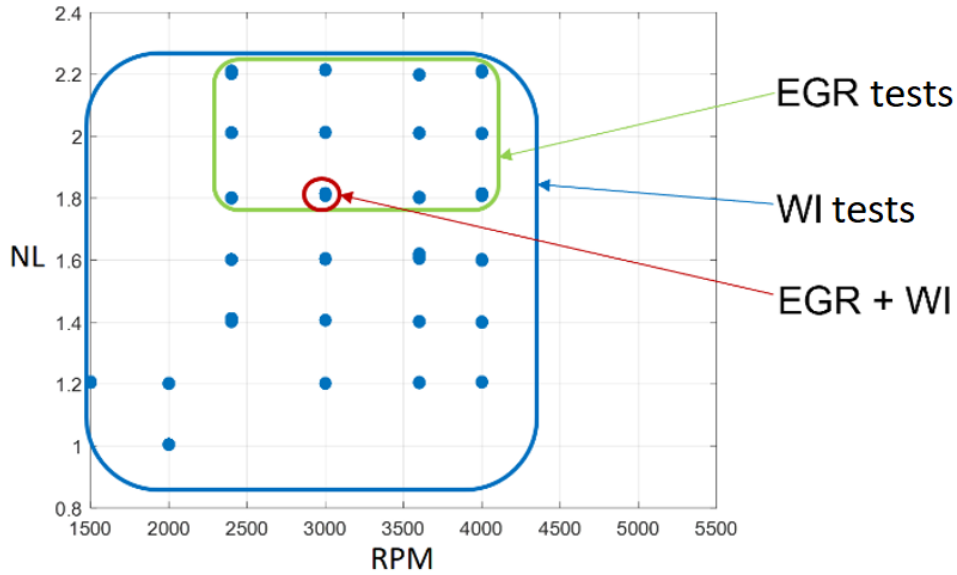
Figure 1.23 - Grid of engine points for each of the experimental campaigns carried out on the second engine.

Focusing on the tests that regard WI (those with EGR are addressed on chapter 3 of this work that explores LP-EGR), a SA sweep was carried out for each engine point at each *r* ratio that was tested. For all the tests, the maximum applied SA corresponds to the knock limited SA, meaning that the most anticipated SA angles in each sweep generate a MAPO percentile value equal to that of the imposed limit, while the most retarded SA corresponds to that in which the obtained EGT reaches the limit of 950°C, imposed for mechanical protection of the turbine. As an example, Figure 1.24 shows SA sweeps performed for *r* ratios up to 0.5 at 3600rpm and 1.6NL. The dots represent measured quantities, and quadratic fitting functions correctly reproduce the trend of SA and EGT as a function of MFB50, for each SA sweep. The already mentioned impact of WI in retarding the combustion phase and cooling the exhaust gases is clearly shown in Figure 1.24 (a) and (b), respectively. From this figure it is also clear that WI expands the combustion phase limits, towards lower values of MFB50 because of increased knock resistance (i.e., when reaching MAPO percentile maximum value), and towards higher values because of cooler exhaust gases (i.e., when reaching 950 °C at the turbine inlet).
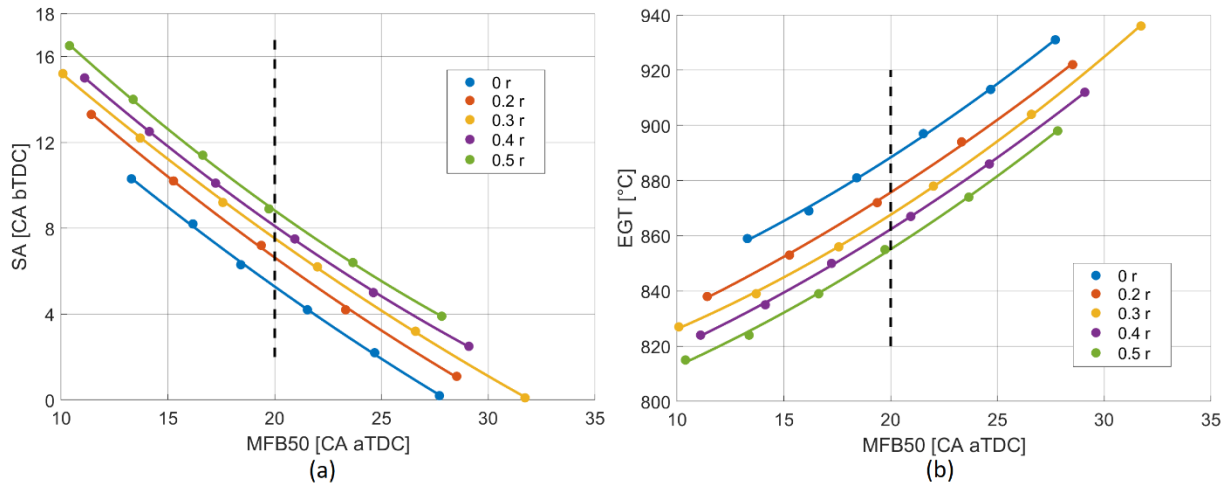
Figure 1.24 - SA vs MFB50 curves (a) and EGT vs MFB50 curves (b), for different values of r. Dashed line indicates the values of SA and EGT for each r case and an arbitrary MFB50 of 20 CA aTDC. Engine point shown: 3600 rpm and 1.6 NL.

1.4.1 Implications of WI on main combustion parameters

From the research activity made on the first engine, it was established that one of the main impacts of WI is that of retarding combustion phase and increasing its angular duration. Now, the scope of the study on this engine was that of being able to quantify and model the combustion delay and cooling effects observed by the usage of WI. These results are later used to compare them with those obtained when using LP-EGR.

1.4.1.1 Torque and BSFC

Using the data that arose from the tests of the WI campaign of this second engine, as shown in Figure 1.23 and Figure 1.24, the impact on parameters such as Torque and BSFC were analysed. Figure 1.25 shows the results for a test at 3600rpm and 1.6NL in which the data has been normalized with respect to the maximum measured values for each variable. BSFC remains almost independent of r and depends almost exclusively on MFB50, but Torque shows a slight separation between the curves at different r ratios. The explanation for this relies on the fact that even if NL was kept constant, the calculation of η_{intake} does not compensate perfectly for the injected water mass and its fresh air displacement effect, meaning that during the tests shown in Figure 1.25, even though NL was constant, the amount of fresh air was not kept perfectly constant in all r cases. The actual intake air flow is lower for increased values of r. This effect is also affected by parameters such as the WI Start Of Injection (SOI) and the injector atomization performance [17]. To keep NL constant, boost pressure had to be adjusted by less than 2%, but as previously stated, this correction did not ensure a perfectly constant intake air flow.
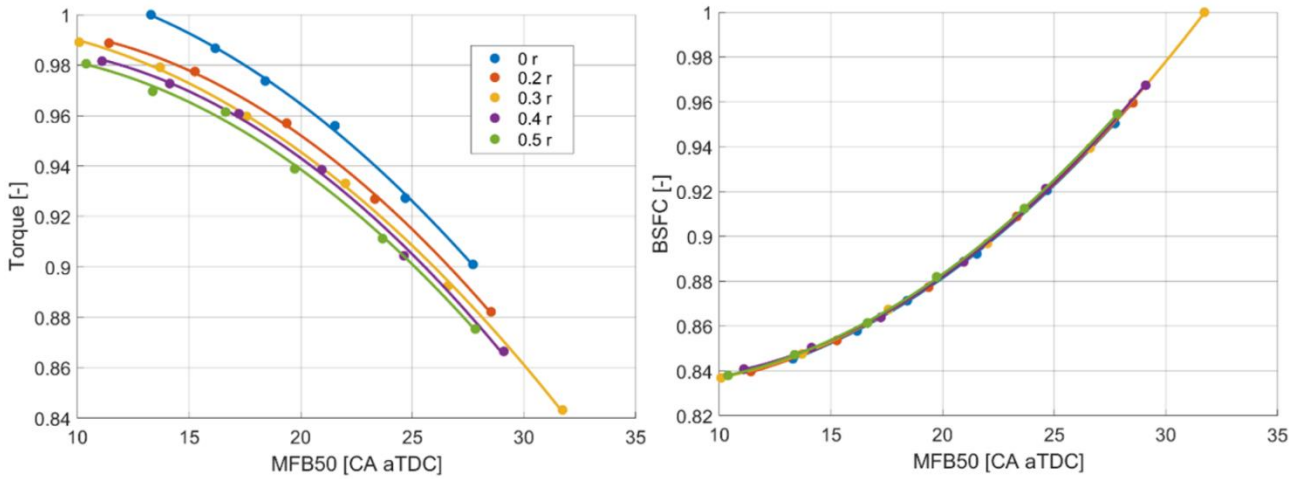
Figure 1.25 - Normalized Torque and BSFC as a function of MFB50, for different values of r. Variables have been normalized with respect to maximum measured values for this engine point. Engine point shown: 3600rpm and 1.6NL.

1.4.1.2 Combustion delay modelling

In this section, the goal was that of quantifying and model the SA increase that must be applied in order to compensate for the delay introduced by WI and obtain a constant MFB50 value. Figure 1.24 shows the results of a test at 3600rpm and 1.6NL that is used as an example to explain the observed effects and modelling procedure. A dashed line is displayed indicating the SA needed to achieve an arbitrary MFB50 target of 20 CA aTDC for each *r* ratio. For the same operating condition, Figure 1.26 (a) directly shows the amount of SA that must be added (called ΔSA), with respect to that of no WI, to achieve the established MFB50 of 20 CA aTDC and compensate for the combustion duration increase introduced by WI. Figure 1.26 (b) shows the same procedure of Figure 1.26 (a) but for other representative cases of RPM and NL (still at an MFB50 of 20 CA aTDC) that have been explored during the experimental campaign and it can be noted that there is a slight change in slope depending on the considered case. It has been found that this trend corresponds to a linear dependence on both NL and *r*, allowing the data shown to be described with a simple two variable linear polynomial function (poly11) as shown in Equation (1.10). This fit produces a surface with an R^2 of 0.96 and a Root Mean Square Error (RMSE) of 0.24 CA, when fitting the data shown in Figure 1.26 (b). Figure 1.27 shows the surface that describes ΔSA as a linear function of *r* and NL, defined by Equation (1.10).
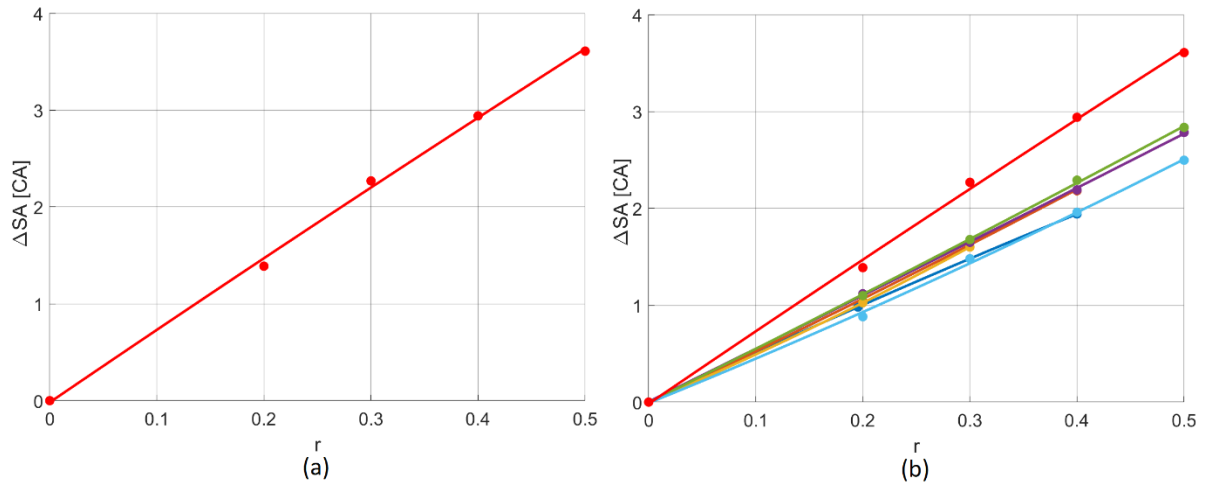
Figure 1.26 - ΔSA as a function of r, denoting the additional SA, with respect to that of the no WI case, to be applied for a given r to compensate combustion retarding and achieve a constant MFB50 of 20 CA aTDC. (a) for the case of 3600 rpm and 1.6 NL, (b) other representative RPM and NL cases during WI tests, each colour represents a different case.
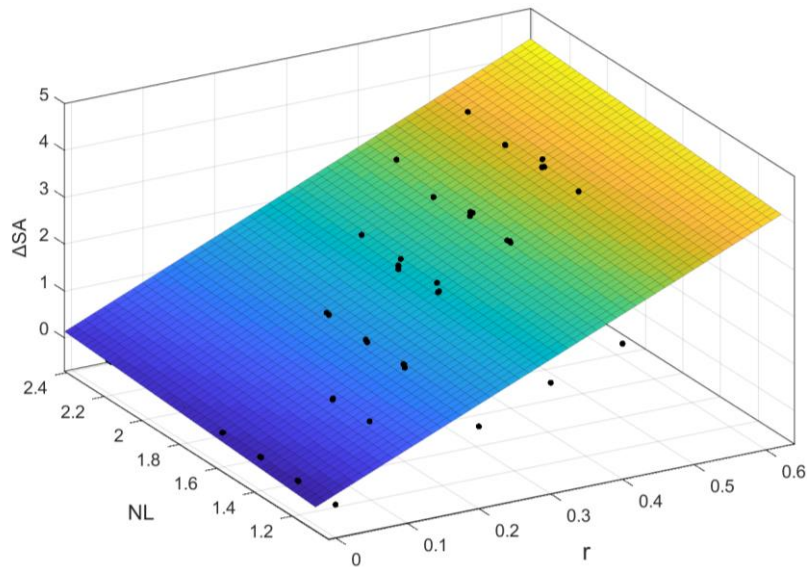
Figure 1.27 - Poly11 surface after fitting ΔSA as a function of r and NL to achieve a constant MFB50 value of 20 CA aTDC. Black dots represent experimental data for such combustion phase.

$$\Delta SA = p_{00\_SA} + p_{10\_SA}r + p_{01\_SA}NL + p_{11\_SA}r \times NL \qquad (1.10)$$

As previously mentioned, the surface in Figure 1.27 is that of the ΔSA to achieve a constant MFB50 of 20 CA aTDC. To further evaluate the validity of this surface, it has been used to calculate the ΔSA for cases of MFB50 different than 20 CA aTDC. The results of this validation are shown in Figure 1.28, in which 95% of the engine points can be validated within an error of ±1 CA, demonstrating that the surface from Figure 1.27 can also be used for values of MFB50 different than 20 CA aTDC.

44
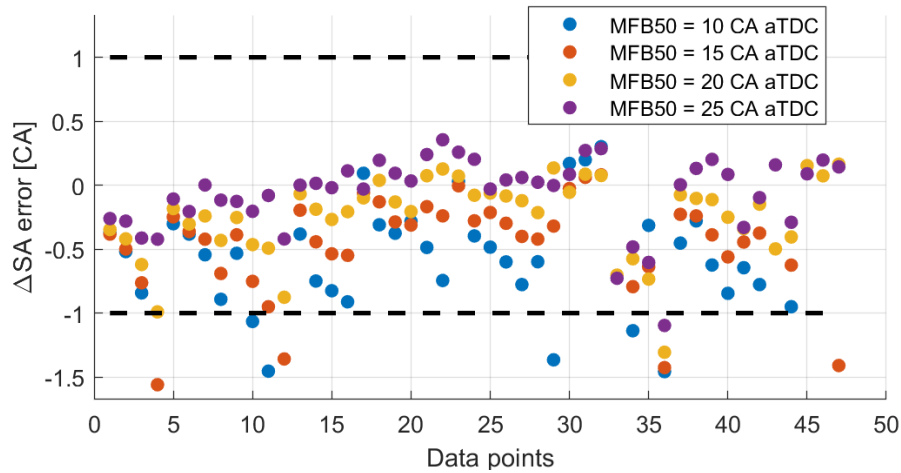
Figure 1.28 - Validation the poly21 surface from Figure 1.27, for combustion phase values different than 20 CA aTDC. ΔSA error refers to the difference between the experimentally measured ΔSA and that calculated from the poly21 surface.

1.4.1.3 EGT reduction modelling

As regards the cooling effect, Figure 1.29 shows directly the EGT decrease (called ΔEGT) when applying a certain r ratio, for the same operating condition of Figure 1.24. The procedure for the calculation of the ΔEGT is analogue to that of the calculation of ΔSA, in which the difference in temperature is observed when applying a certain r ratio, keeping MFB50 equal to 20 CA aTDC. A linear trend is observed like in the case of combustion delay. Cooling of around 37°C was achieved with an r of 0.5. Figure 1.29 (b) shows this linear trend for all RPM and NL cases (and an MFB50 of 20 CA aTDC) and it is noted that these lines tend to separate when changing engine point. The explanation of this relies on the fact that when load is increased, overall temperature in the intake manifold is higher, causing the water that is injected with the same SOI to evaporate mainly within the runners and not when inside the chamber [25], reducing slightly the cooling effect at higher loads. As mentioned before, this effect creates a slight dependency on NL and thus the fit used for ΔEGT in Figure 1.29 (b) is a two variable first grade polynomial (poly11) as a function of r and NL as shown in Equation (1.11). Figure 1.30 shows the surface that arises from the poly11, producing a fit of the data with an R^2 of 0.97 and an RMSE of 2°C.
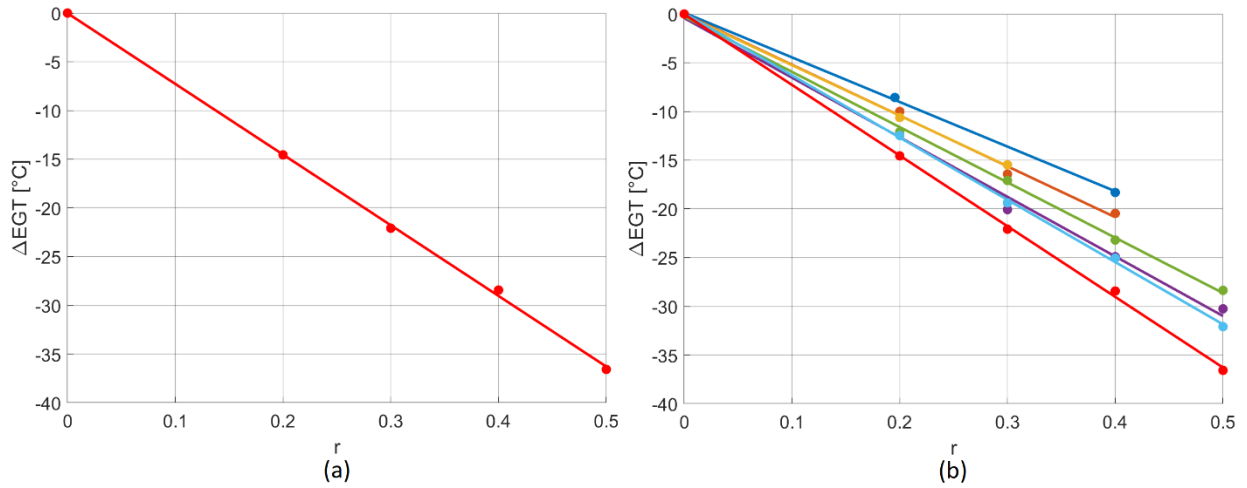
Figure 1.29 - ΔEGT as a function of MFB50, denoting the reduction of EGT when applying different r ratios, at a constant MFB50 of 20 CA aTDC. (a) for the case of 3600rpm and 1.6NL, (b) other representative RPM and NL cases during WI tests, each colour represents a different case.
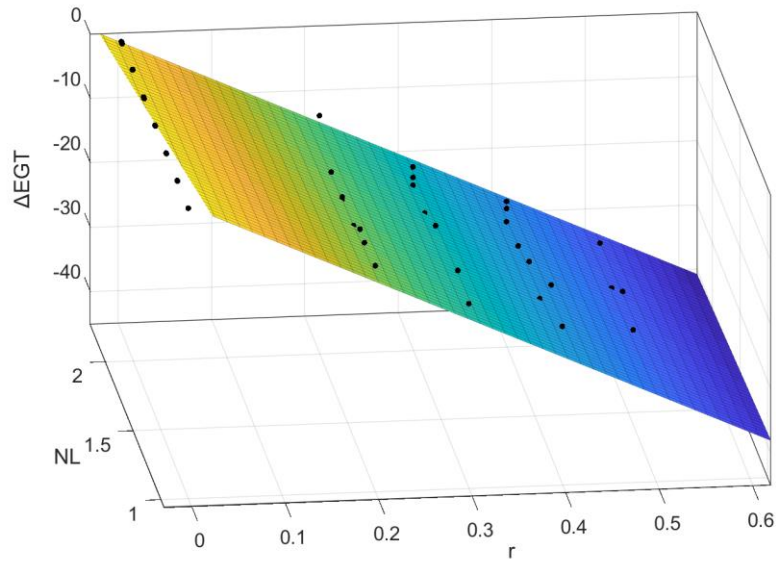
Figure 1.30 - Poly11 surface after fitting ΔEGT as a function of r and NL to achieve a constant MFB50 value of 20 CA aTDC. Black dots represent experimental data for such combustion phase.

$$\Delta EGT = p_{00\_EGT} + p_{10\_EGT}r + p_{01\_EGT}NL + p_{11\_EGT}r \times NL \qquad (1.11)$$

The poly11 surface from Figure 1.30 is that of the ΔEGT when observed at a constant MFB50 of 20 CA aTDC. To further evaluate the validity of this fit, it has been used to calculate the ΔEGT for cases of MFB50 different than 20 CA aTDC. The results of this validation are shown in Figure 1.31, in which 99% of the engine points can be validated within an error of ±10 °C, demonstrating that the fit can also be used for values of MFB50 different than 20 CA aTDC.
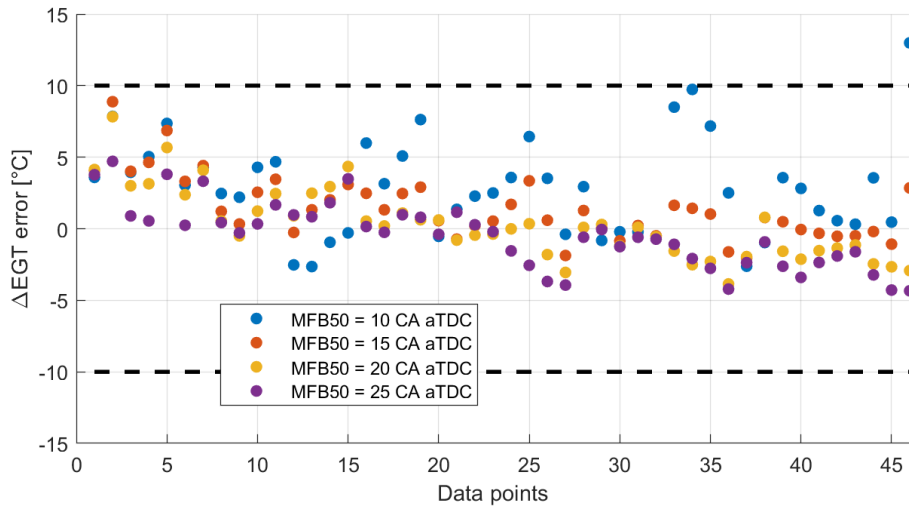
Figure 1.31 - Validation of all tested engine points (not only with an MFB50 value of 20 CA aTDC) using the poly11 surface from Figure 1.30. ΔEGT error refers to the difference between the experimentally measured ΔEGT and that calculated from the poly11 surface.

1.5   Conclusions

The first experimental setup used in this chapter consisted of a commercial 1.4L GDI engine in which a prototypal WI system was installed. Since the main aim of this study was that of using WI in search of increased efficiency, this first setup was used initially to identify the implications of WI on combustion phase, a variable that is strictly related to engine efficiency. For this, a combustion model (WICM) capable of calculating the necessary SA to achieve a desired MFB50, while considering the effects of WI was developed. The main inputs of the model are MFB50, RPM, NL and water-fuel ratio (*r*). As a subsequent step towards achieving higher efficiency, a combustion controller (WICC), that uses the WICM, to manage WI for knock mitigation and optimal combustion phase was developed. A detailed validation and evaluation of the performance of this controller has been carried on by a step-by-step approach. The RT compatibility of the proposed approach allows the controller implementation in a RCP environment, and eventually in a production control system. At first, a completely open-loop configuration has been tested, showing that the WICM is able to manage a MBF50 angle close to MFB50 target with a precision of 1 CA even in presence of WI. Furthermore, the model in combination with the proposed strategy of closed-loop knock control has been used to manage the knock level applying both an actuation of *r* and a correction of SA. Through this configuration, the feasibility of knock mitigation by the usage of WI without sensible variation in MFB50 (if *r* is not saturated) has been demonstrated. In fact, the presence of variations of *r* does not significantly affect the combustion phase due to the WICM compensation and the knock level can be stabilized to the established threshold. The addition of a closed-loop on MFB50 made available using in-cylinder pressure signals allows to better implement the WICC and extract the highest engine efficiency, keeping the combustion phase on the target as long as *r* value is not saturated. The fuel savings associated to the usage of WI have been finally quantified and it was found that a

reduction of up to 16% could be achieved, and the reason for this is not so much the improved combustion phase but the lower mixture enrichment. The fuel that is usually used to cool the combustion chamber and to avoid knock via the standard approach is now no longer necessary, and WI becomes a substitute of this.

A second experimental setup was used, comprised of a commercial 2.0L turbocharged GDI engine to which a more production-oriented WI system was mounted. The aim of the studies carried out on this engine was to further explore the impact of WI in other fundamental variables such as torque and BSFC, as well as to model the combustion phase delay and EGT reduction effects of WI, and compare them to those of a LP-EGR system, which this engine mounts as OEM equipment. BSFC shows to be independent of WI and only dependent on MFB50, while torque had a slight dependence on the *r* ratio used but this was attributed to the displacing effect that water has on the intake air, which is not perfectly accounted for during the calculation of NL. The models that arose from these studies to describe both combustion delay and EGT cooling were simple polynomial functions with NL and *r* as input. Validation results showed that it was possible to estimate combustion delay within ±1 CA and EGT cooling within ±10°C in all the explored engine points.

As final general remarks on WI technology, based on the experience on both engines, it can be said that the usage of WI is especially beneficial at high loads and that its main advantage in terms of fuel consumption is given by the water substitution of the extra fuel on a rich mixture used for combustion chamber cooling. More optimal combustion phase can be achieved with WI, given its knock suppression capabilities, but the fact that WI itself delays combustion leads to a marginal benefit in terms of combustion efficiency improvements. Additionally, the high *r* ratios needed at high loads mean that water consumption could become unpractical when considering a production application, which would require either a large water tank or the driver to often refill a smaller water tank.

2 Low-Pressure Exhaust Gas Recirculation

EGR consists of the recirculation of exhaust gases into the cylinder, and it can be used in two main configurations, High-Pressure EGR (HP-EGR) and Low-Pressure EGR (LP-EGR) and the EGR ratio is determined by Equation (2.1).

$$EGR = \frac{m_{EGR}}{m_{EGR} + m_{air}}$$
(2.1)

Where m_{EGR} and m_{air} represent the masses of recirculated exhaust gases and fresh air entering the cylinder during a cycle, respectively. In the case of HP-EGR, the exhaust gases are mixed downstream the compressor and are recirculated from before the turbine inlet, while in the case of LP-EGR, the exhaust gases are extracted after the catalytic converter and inserted in the air flow before the compressor inlet. LP-EGR is also generally cooled with a water/gas heat exchanger before mixing, leading to even greater benefits [49]. When using EGR, if intake manifold pressure is kept constant, inert exhaust gases will replace part of the fresh air entering the engine and a decrease in torque would be observed. For this reason, EGR acts not only as a gas that absorbs heat and lowers combustion chamber temperature but also requires further opening of the throttle valve or closure of wastegate (to maintain equal torque production with respect to a situation of no EGR) and thus reduces pumping losses [50]. In the case of gasoline turbocharged engines, EGR is therefore used at high loads to reduce the need of a rich mixture for combustion chamber cooling but it can also be used at partial loads to improve efficiency and reduce emissions [51]. In the case of HP-EGR, the increase of EGR rate has the disadvantage of reducing the amount of exhaust gases reaching the turbine and thus harming the performance of the turbocharger [52,53]. In the case of LP-EGR this issue is not present but still, as the exhaust gas is reinserted before the turbocharger compressor, the volumetric flow that the compressor must supply is incremented by the addition of the EGR and given that only the fresh air contributes to power generation, the compressor may now represent a limiting factor for high load performance. The compressor's volumetric flow limit is due to its maximum speed imposed by mechanical constraints, and therefore it would need to be specifically designed to compensate such limitation [19]. Another distinction between these two types of EGR systems is that the LP configuration has slower dynamics than the HP one, mainly since the gas being recirculated in the case of LP must travel a longer path before reaching the combustion chamber.

Authors such as Lu et al [16] have implemented LP-EGR on a boosted GDI engine and assessed its benefits when used during a New European Driving Cycle (NEDC). Figure 2.1 shows some of the results obtained by Lu, where the blue numbers represent the percentage of BSFC benefit and the red numbers the percentage of the NEDC in which the engine has operated during the cycle. Mean BSFC improvements of 2.74% on low load, 4.03% at mid loads and 7.79% at high loads were registered, when compared to base engine calibration without EGR, demonstrating the real-world advantage of the technology.
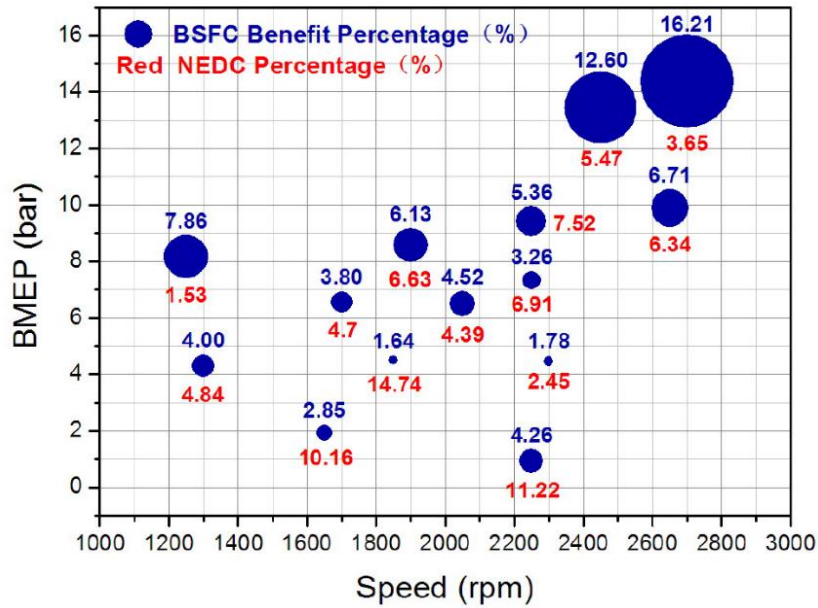
Figure 2.1 - Benefits of using LP-EGR when tested on a NEDC. Source [16].

Alger et al [54] carried out experimental tests on a 1.6L turbocharged GDI engine using LP-EGR, analysing the effects on fuel consumption at both constant combustion phasing (to isolate effects of EGR as diluent) as well as advanced combustion phasing (to include benefits of knock suppression and improved MFB50). Figure 2.2 shows part of the results presented by Alger, in which a BSFC reduction from 253 g/kWh to 240 g/kWh is observed when considering just the benefits of EGR as a diluent. Further improvements are obtained when using EGR to advance combustion phase, reaching a BSFC of 230g/kWh, but with high EGR ratios of 0.2, point from which diluent benefits seem to have reached the maximum and the increased combustion duration starts having a negative impact on fuel consumption.
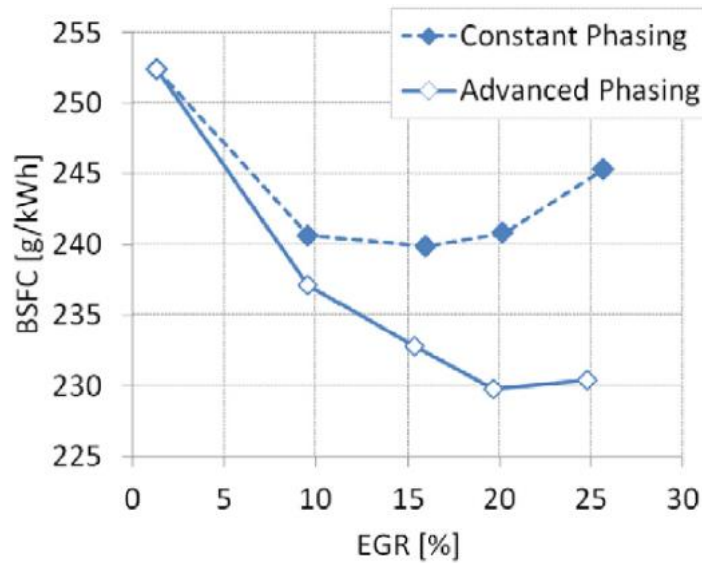
Figure 2.2 - BSFC results for 1500 rpm / 12 bar BMEP with both retarded and advanced combustion phasing. Source [54].

Siokos et al [15] have also studied LP-EGR on a similar setup, achieving a fuel consumption saving of up to 16% while utilizing EGR ratios of 0.2 to both achieve MBT and stoichiometric operation. Dilution benefits alone (constant MFB50) have also been explored by Siokos, arriving to the conclusion that, as also found by Alger, these tend to achieve their maximum benefits at around 0.2 EGR, as shown in Figure 2.3. Siokos also found a correlation between combustion duration and Coefficient of Variation (COV) of IMEP and retains that 0.2 EGR is too high to guarantee a low COV of IMEP for production standards given the increased combustion duration introduced by EGR.
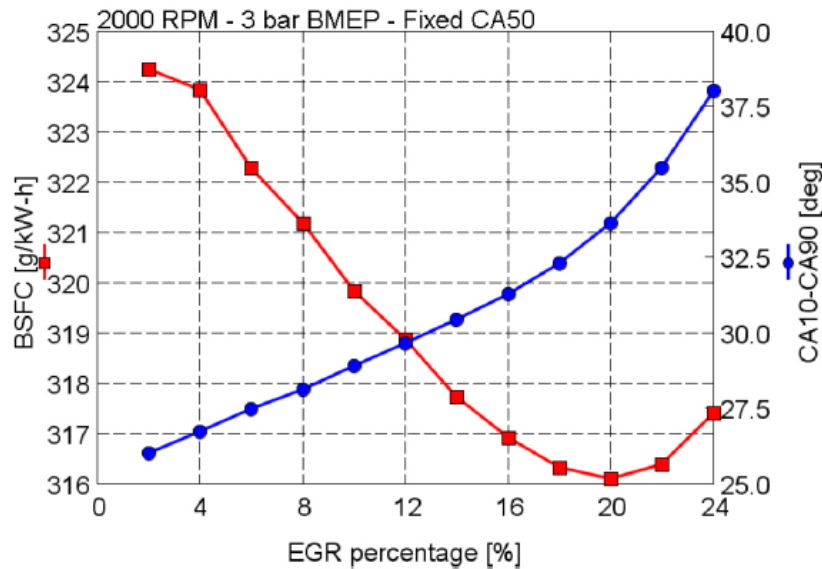
Figure 2.3 - Results for the effect of combustion duration on BSFC as a function of LP-EGR dilution, with fixed MFB50 at MBT (2000RPM, 3bar BMEP). Source [15].

Falfari et al [25] have carried out several CFD studies when diluting mixtures with LP-EGR and WI, observing a decrease in laminar flame speed of 19% when using 0.06 EGR when compared to 32% decrease when using a water-fuel ratio of 0.06. Cordier et al [19] have studied the simultaneous usage of WI and LP-EGR, with the premise that EGR helps reducing cylinder heat wall losses and WI aids mostly to cool the chamber and mitigate knock while allowing to improve combustion phase, premises already introduced by Alger and Siokos. Results of this are shown in Figure 2.4, where the indicated efficiency losses associated to the three cases of using only WI, only EGR and WI + EGR are shown. This evidences that the joint usage of WI and LP-EGR had similar results when compared to only WI, with respect to MFB50 improvement, meaning that most of the combustion phase improvement is given by WI. On the other hand, wall losses are most significantly commanded by EGR. For this reason, the authors suggest using high water-fuel ratios for knock suppression and enhanced combustion phase, while also using no more than 0.05 EGR so as not to introduce an unnecessary combustion lengthening but still reduce wall heat losses.
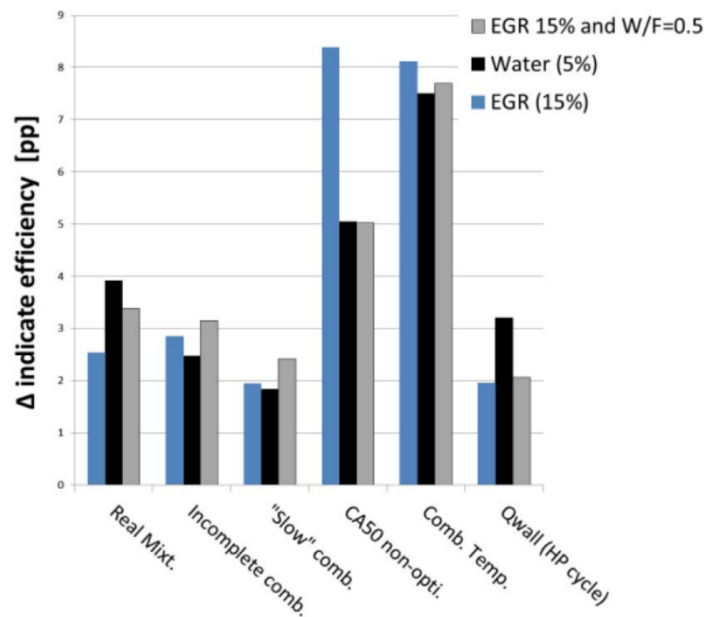
Figure 2.4 – Comparison of indicated efficiency losses between 15% EGR dilution, 5% water dilution (DWI at 100bar) and the combination of both (15% EGR and W/F=0.5 at 125bar of injection pressure), at 2000RPM 17bar IMEP. Source [19].

This chapter introduces the results that arise from experimental tests on a turbocharged GDI engine with LP-EGR and port WI, to then compare these two technologies on the same base engine and to evaluate their possible synergic benefits in maximizing engine performance and efficiency. The main contribution with respect to the actual state of the art is the development of mathematically simple and robust LP-EGR models for compensating the corresponding combustion duration increment and the prediction of associated EGT cooling effect, which can be easily inverted to be used in a control strategy, especially to control EGT. This is achieved by a wide experimental analysis to directly compare LP-EGR and WI on the same engine, allowing to quantify the performance of such solutions, separately and jointly, and to clarify if and how they may allow reaching stoichiometric operation at very high specific loads. Additionally, a direct comparison of the engine performance obtained with the traditional approach of mixture enrichment, the usage of WI and finally LP-EGR is made, making even clearer the comparison between these two technologies with respect to the traditional approach in a close-to-production setup.

At first, a brief description of the experimental setup used for the LP-EGR is presented. Then, the effects of LP-EGR on the main combustion parameters such as MFB50, EGT, Torque and BSFC are modelled and subsequently compared to those observed with WI from Chapter 1. Fast, control-oriented experimental models are then presented, being able to calculate the combustion retarding effect and the cooling capabilities of LP-EGR, like in the case of WI. The main limitations of each approach are also highlighted. After this, the effects of EGR and WI are confronted and a synergy between EGR and WI when used simultaneously is investigated. Finally, three different engine calibrations were generated on the same engine, to directly assess the benefits of implementing a LP-EGR system and compare it with that of using WI or the traditional approach of mixture enrichment.

The main findings shown in this chapter have been the subject of a publication by the author of this thesis [37].

2.1   Experimental setup

The engine that was used for this study is the same that was described in Section 2.4 and the engine layout is that of Figure 1.22. The EGR setup is a cooled LP-EGR system in which the exhaust gases to be recirculated are extracted after the Three-Way Catalyst (TWC). From this point onwards, each time EGR is mentioned in this work, it refers to cooled LP-EGR. An additional oxygen sensor, apart from those used for mixture control, has been installed in the intake manifold used to measure oxygen concentration. By comparing such value to that of fresh air, the EGR ratio was estimated through a series of models that are not displayed in this work for confidential reasons. During the experimental tests, the setting of variables such as SA, EGR and WI ratio, wastegate position, among others, has been done via INCA software that communicates to the engine's main ECU via an ETAS module. A development ECU has been used, allowing to overwrite all calibration parameters while experimental tests were being carried out.

Figure 1.23 shows the grid of engine points that has been used for the two experimental campaigns that regard LP-EGR. The first was just using EGR and the second used both EGR and WI together in the search of a synergy. The procedure followed to carry out the SA and EGR sweeps were identical to those for the exploration of WI. EGR ratios that of up to 0.12 (meaning 12%) were used, an such limit value was chosen in accordance with production applications that limit the amount of EGR to ensure combustion stability and low cycle-to-cycle variations.

As an example, Figure 2.5 shows SA sweeps performed for EGR ratio up to 0.12 at 3000 rpm and 2 NL. The dots represent measured quantities, and quadratic fitting functions correctly reproduce the trend of SA and EGT as a function of MFB50, for each SA sweep. The already mentioned impact of EGR in retarding the combustion phase and cooling the exhaust gases is clearly shown in Figure 2.5 (a) and (b), respectively. From this figure it is also clear that EGR expands the combustion phase limits: towards lower values of MFB50 because of increased knock resistance (i.e., when reaching MAPO percentile maximum value), and towards higher values because of cooler exhaust gases (i.e., when reaching 950 °C at the turbine inlet).
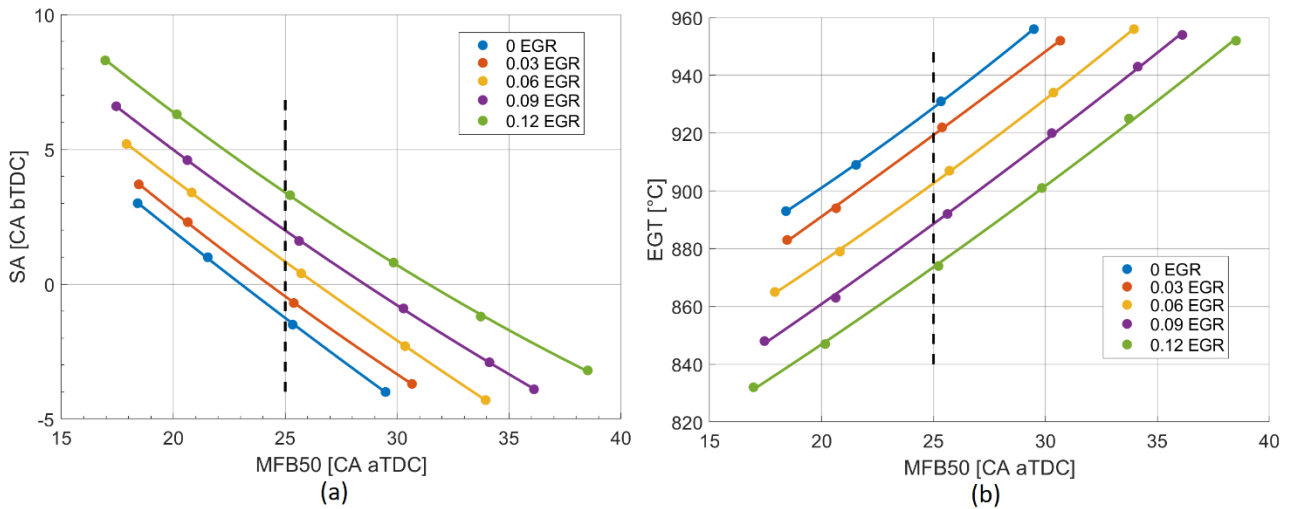
Figure 2.5 - MFB50 vs SA curves (a) and MFB50 vs EGT curves (b), for different values of EGR. Dashed line indicates the values of SA and EGT for each EGR case at an arbitrary MFB50 of 25 CA aTDC. Engine point shown: 3000rpm and 2NL.

As described previously, a SA sweep was carried out for each EGR ratio that was tested. For all the tests, the maximum applied SA corresponds to the knock limited SA (meaning that all most anticipated points in each sweep possess a MAPO percentile value equal to that of the imposed limit), while the most retarded SA corresponds to that in which the obtained EGT reaches the limit of 950°C (imposed for mechanical protection of the turbine). As already mentioned, increasing EGR ratio could decrease torque production since inert gas replaces a portion of fresh air. To avoid such effect and to maintain constant torque output for each tested engine point, every time EGR was increased, the amount of fresh air entering the engine was re-established to its previous value. This was done by adjusting turbocharger wastegate position to increase boost, thus increasing total gas mass flow through the compressor. During this work EGR therefore represents an addition of a certain percentage of inert gas to the intake air mass. In order to achieve this, the compressor must handle higher volumetric flows and higher pressure ratios, for which it needs to rotate at higher speed. This introduces a first limitation of the LP-EGR system for high loads when high EGR rates are necessary, since the turbocharger achieves its speed limit, not being able to generate higher flow of both fresh air and recirculated gas. This means the achievable performance could be lower if compared with the traditional approach of enriching fuel mixture for its cooling effect instead of using EGR. Another aspect that may produce a limitation on LP-EGR application is the fact that the flow of recirculated gases is produced solely by the pressure difference between the exhaust gases after the TWC and the compressor inlet. At mid/high loads where exhaust pressure is sufficiently high this is generally not an issue, but at part/low loads, high EGR rates may not be achieved.

Table 2.1 contains the intake pressure values needed to achieve the mentioned constant fresh air mass flow for each EGR ratio, showing a linear increase of absolute intake pressure with respect to the amount of EGR used. Such values demonstrate that for reaching higher EGR ratios the turbocharger would probably need to be redesigned for the specific application.

EGR ratio	Absolute intake pressure
0	2.35 bar
0.03	2.43 bar
0.06	2.49 bar
0.09	2.58 bar
0.12	2.64 bar

2.2   Implications of LP-EGR on main combustion parameters

As done on this same engine with the WI system but now with LP-EGR, the carried out experimental tests were used to analyse its impact on the main combustion parameters and model the combustion delay and EGT cooling effect. At the end of this section, a comparison between WI and LP-EGR is done and a search for a possible synergy is explored.

2.2.1.1   Torque and BSFC

Figure 2.6 shows the impact of EGR on Torque and BSFC (normalized values are shown for confidentiality reasons). As it can immediately be observed, the curves of both Torque and BSFC corresponding to different EGR ratios overlap almost completely, denoting an essentially unique behaviour, depending only on MFB50 and thus SA. This is mainly because, as explained previously, the mass flow of fresh air into the engine is kept constant for all EGR ratios. These superposed curves also denote that when EGR ratio is increased the additional exhaust gases do not have further effects other than retarding combustion to a greater extent and absorb extra heat, when maintaining a given combustion phase.
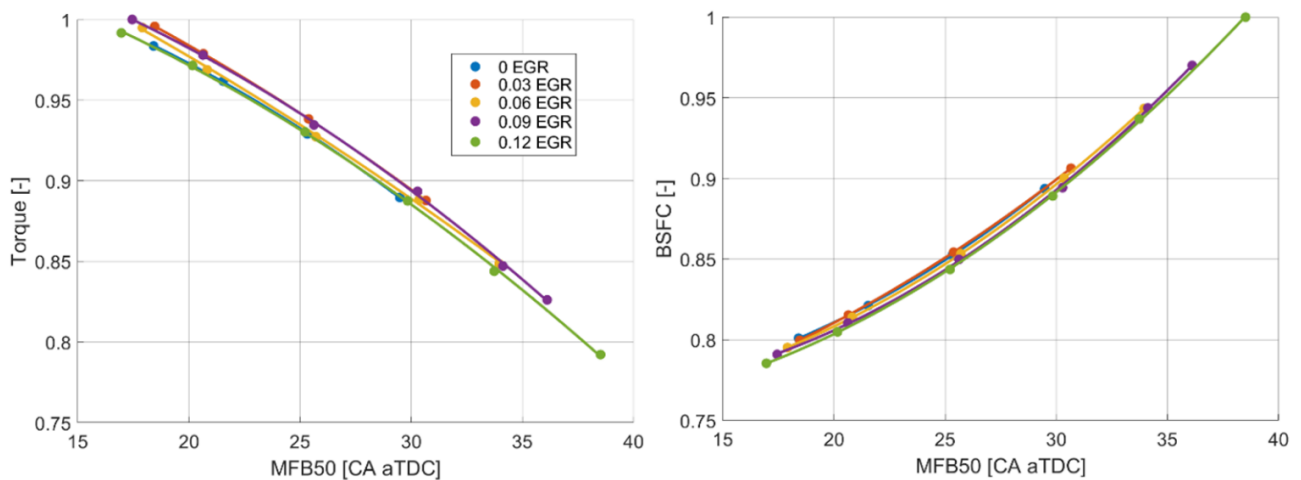
Figure 2.6 - Normalized Torque and BSFC as a function of MFB50, for different values of EGR. Values have been normalized with respect to the maximum ones for this engine point. Engine point shown: 3000 rpm and 2 NL.

Having established that the two parameters in which EGR has the most impact are combustion phase and EGT, the following sections concentrate on these two.

2.2.1.2   Combustion phase delay modelling

When analysing the ΔSA and ΔEGT curves for EGR, the same procedure is applied than in the case of WI, observing the difference in SA and EGT, with respect to that of no EGR, for different values of r and a fixed MFB50 of 25 CA aTDC. Figure 2.5 (a) shows a dashed line indicating the SA needed to achieve an arbitrary MFB50 target of 25 CA aTDC for each EGR case. For the same operating condition, Figure 2.7 (a) directly shows the ΔSA, with respect to that of no EGR, to achieve the established MFB50 of 25 CA aTDC and compensate for the combustion duration increase introduced by EGR. Figure 2.7 (b) shows the same procedure of Figure 2.7 (a) but for other representative cases of RPM and NL (still at a MFB50 of 25 CA aTDC) and it can be noted that there is a slight change in slope depending on the considered case. It has been found that, like on the case of WI, this coincided with a load dependence that can be fitted with a simple two-variables polynomial function, with a quadratic dependence on EGR and a linear dependence on NL like that of Equation (2.2). This fit produces a surface with an R2 of 0.99 and a RMSE of 0.15 CA, when fitting the data shown in Figure 2.7 (b). Figure 2.8 shows the resulting surface that describes ΔSA as a function of EGR and NL.
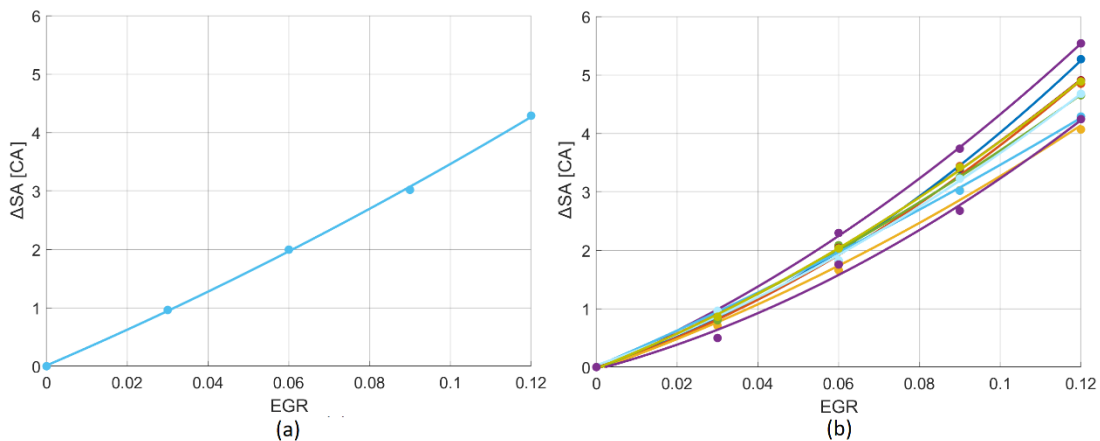
Figure 2.7 - ΔSA as a function of EGR, denoting the SA increase, with respect to no EGR case, to be applied for a given EGR ratio to compensate for combustion duration increment and to achieve a constant MFB50 of 25 CA aTDC. (a) for the case of 3000 rpm and 2 NL, (b) other representative RPM and NL cases during EGR tests, each colour represents a different case.
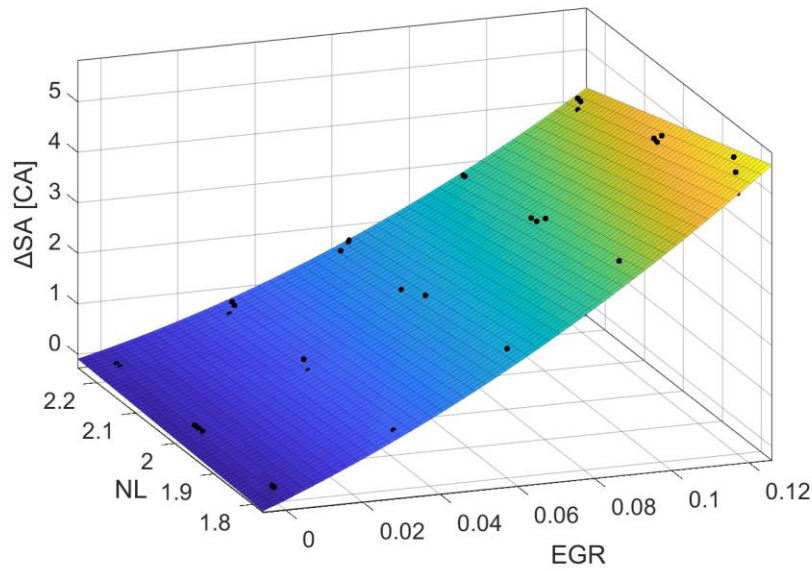
Figure 2.8 - Poly21 surface (second order in EGR, first order in NL) after fitting ΔSA as a function of EGR and NL to achieve a constant MFB50 value of 25 CA aTDC. Black dots represent experimental data for such combustion phase.

$$\Delta SA = p_{00} + p_{10}EGR + p_{01}NL + p_{20}EGR^2 + p_{11}EGR \cdot NL \qquad (2.2)$$

As previously mentioned, the surface in Figure 2.8 is that of the ΔSA to achieve a constant MFB50 of 25 CA aTDC. To further evaluate the validity of this surface, it has been used to calculate the ΔSA for cases of MFB50 different than 25 CA aTDC. The results of this validation are shown in Figure 2.9, in which 95% of the engine points can be validated within an error of ±1 CA (self-imposed accuracy target), demonstrating that the surface from Figure 2.8 can also be used for values of MFB50 different than 25 CA aTDC.
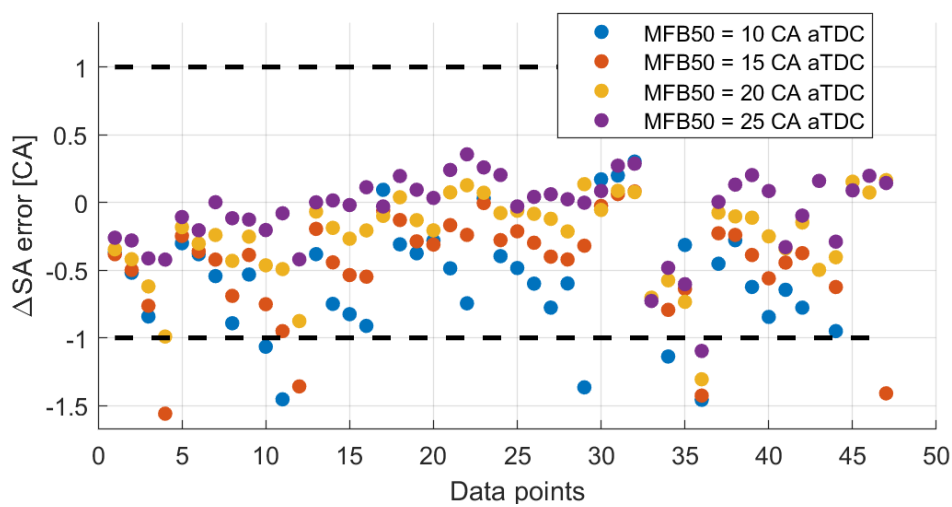
Figure 2.9 - Validation the poly21 surface from Figure 2.8, for combustion phase values different than 25 CA aTDC. ΔSA error refers to the difference between the experimentally measured ΔSA and that calculated from the poly21 surface.

As regards the cooling effect observed when using LP-EGR, Figure 2.10 shows directly the ΔEGT achieved when applying a certain ratio of EGR, for the same operating condition of Figure 2.5. The procedure for the calculation of the ΔEGT is analogue to that of the calculation of ΔSA, in which the difference in temperature is observed when applying a certain ratio of EGR, keeping MFB50 equal to 25 CA aTDC. EGT reduction of around 60°C has been achieved with an EGR ratio of 0.12. In this case, the fitting of data from all RPM and NL cases (shown as a dashed line in Figure 2.10 (b)) can be performed simply with a linear function depending only on EGR, yielding a fit with an R2 of 0.98 and an RMSE of 2.4 °C. This model can be used to predict the reduction in terms of EGT when applying a certain EGR ratio. Given the simplicity of the linear function, the inverted model may be used in an engine control strategy to calculate the necessary EGR ratio to achieve a certain cooling effect for components protection.
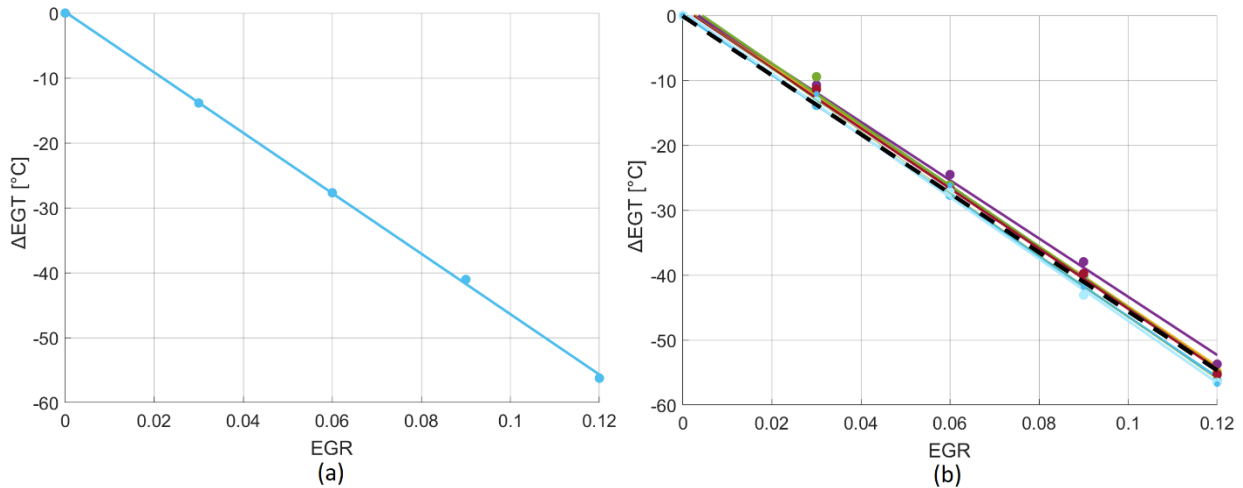
Figure 2.10 - ΔEGT as a function of EGR, denoting the reduction of EGT when applying different ratios of EGR, at a constant MFB50 of 25 CA aTDC. (a) for the case of 3000 rpm and 2 NL, (b) other representative RPM and NL cases during EGR tests, each colour represents a different case. The dashed line in (b) represents the linear fit of all data present in the figure.

As previously mentioned, the linear fit shown in the dashed line of Figure 2.10 (b) is that of the ΔEGT when observed at a constant MFB50 of 25 CA aTDC. To further evaluate the validity of this linear fit, it has been used to calculate the ΔEGT for cases of MFB50 different than 25 CA aTDC. The results of this validation are shown in Figure 2.11, in which 93% of the engine points can be validated within an error of ±10 °C (self-imposed accuracy target), demonstrating that the fit that arises from Figure 2.10 can also be used for values of MFB50 different than 25 CA aTDC.
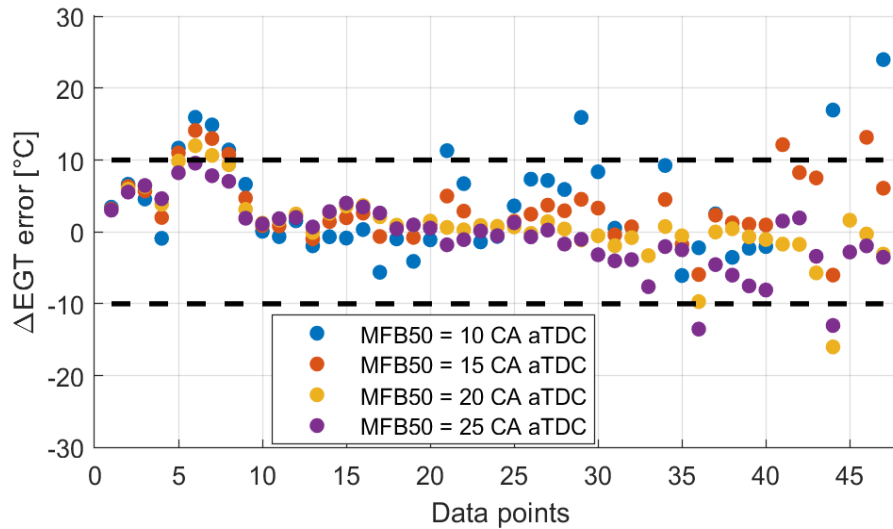
Figure 2.11 - Validation of all tested engine points (not only with an MFB50 value of 25 CA aTDC) using the linear fit arising from Figure 2.10 (b). ΔEGT error refers to the difference between the experimentally measured ΔEGT and that calculated from the linear fit.

The observed cooling effect is mainly attributed to two factors. First, the combustion phase delay and its increased duration that EGR dilution introduces. Secondly, the heat that the added recirculated gas absorbs when introduced in the combustion chamber. Additionally, the exhaust gas that is recirculated contains a higher specific heat than the fresh air [55], contributing even more to the lowering of EGT. This topic is discussed further in the following section, where EGR is compared to WI.

2.3   Comparison between LP-EGR and WI

Having discussed the results obtained for EGR and WI, in this section a direct comparison of the results of each strategy is done, using as an example one of the engine points tested for both EGR and WI experimental campaigns. This allows to identify a quantitative relationship between these two possible solutions, establishing the ratios to be used in each case to achieve similar EGT reduction effects.

Figure 2.12 shows ΔSA for both EGR and WI for the engine point that is used as an example, 2400 rpm and 2.2 NL. This figure shows only one engine point, but the conclusions do not vary significantly when making the comparison on the rest of the engine points. At first sight it seems that EGR has a much stronger effect on combustion phase than WI, but some remarks need to be made to correctly compare the two solutions. The use of EGR is limited by factors such as combustion stability (quantified using as index the IMEP Coefficient of Variation (CoV of IMEP)) as discussed in the following section, as well as the previously mentioned limit of increased compressor volumetric flow demand. WI on the other hand is not associated with such compressor related issues but is limited in terms of maximum r due to combustion stability and the refilling frequency of the water tank in the final on-board application. This container is sized so that the driver must not refill it for long time intervals, in the order of several thousands of kilometres, imposing practical

limits for the maximum *r* of around 0.6. Additionally, at high *r* rates the water that is injected starts to create oil dilution problems that affect engine lubrication [19].
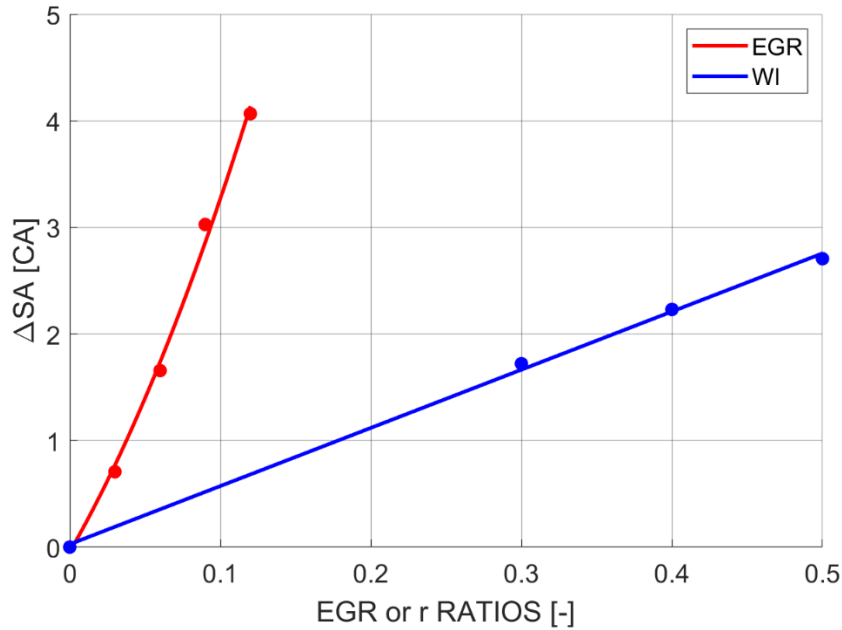
Figure 2.12 - ΔSA as a function of EGR and r for the cases of LP-EGR and WI (when used separately). The engine point corresponds to 2400 rpm and 2.2 NL. EGR and WI ratios are expressed as fractions.

When looking at Figure 2.13, where the cooling capabilities of both EGR and WI are compared, it is immediately noted that the effects of EGR regarding cooling is comparable to that of WI or even greater within the explored range. When analysing all engine points, an approximate equivalence of almost five to one is observed, meaning for example that a 0.03 of EGR ratio corresponds to 0.15 of *r*. This quantitative relationship is not constant for all EGR or *r* ratios, at higher ratios the gap is further increased, meaning that even more water would be needed. The explanation of why EGR seems to have a greater effect than WI for a similar ratio relies on the fact that the mass of intake air is around 14.7 times greater than that of fuel. It must be remembered that the ratio of EGR and *r* are referenced to two different parameters, being EGR a ratio with the mass of intake air as a reference, and *r* a ratio with the mass of injected fuel as a reference.
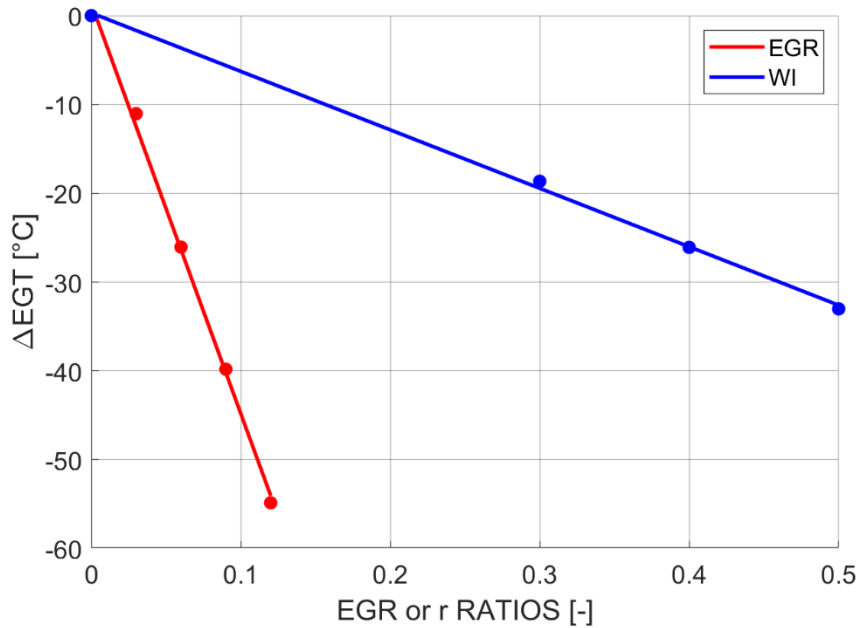
Figure 2.13 - ΔEGT as a function of EGR and r for the cases of LP-EGR and WI (when used separately). The engine point corresponds to 2400 rpm and 2.2 NL. EGR and WI ratios are expressed as fractions.

The EGR cooling effect is caused mainly by two factors. One is the absorption of heat by the additional exhaust gases that have been recirculated, and the other factor is the increased combustion duration caused by the dilution of the fresh mixture and the higher specific heat capacity of EGR gas. Combustion duration is defined as the difference between MFB10 and MFB90 [56], meaning the CA interval between the angular positions in which 10% of the mixture has been burned and that when 90% has been burned. Figure 2.14 shows how combustion duration increases with increasing EGR or r. Sweeps in Figure 2.14 (b) seem to present a linear trend when compared to those of Figure 2.14 (a) that clearly exhibit a parabolic trend. In fact, they are both parabolic but the explored MFB50 range in Figure 2.14 (b) is much narrower than that of Figure 2.14 (a), making them look like linear fits rather than parabolic. The slight difference in combustion duration (inferior than 0.5 CA) between the cases of no EGR and no WI in Figure 2.14 is generated because ambient conditions were not exactly identical during both tests. It is also to be noted that the increase in combustion duration becomes more evident when considering high values of MFB50. This was verified not only on the engine point shown in Figure 2.14 but also on the rest of the explored operating conditions.
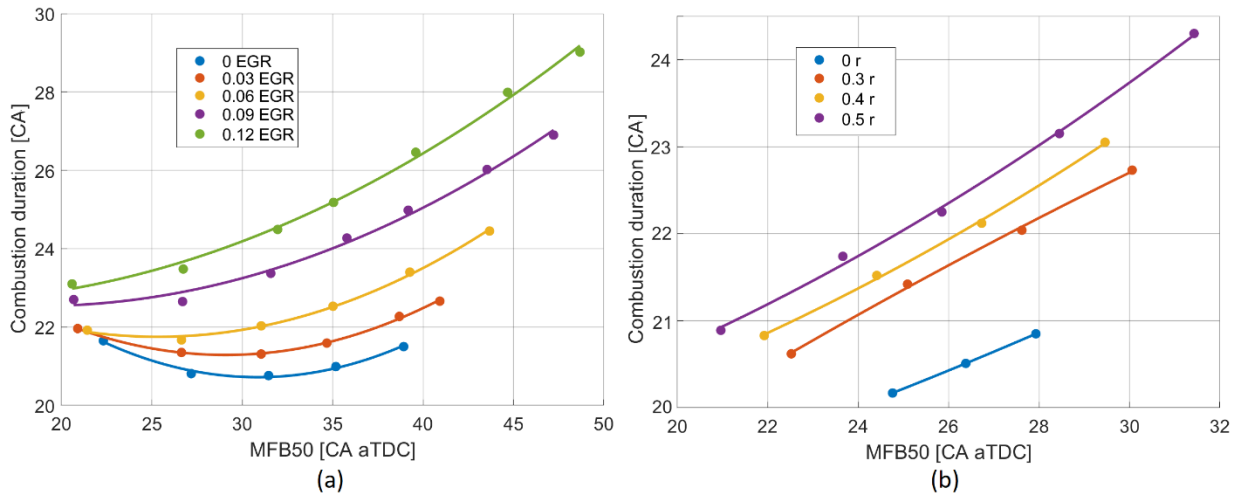
Figure 2.14 - Combustion duration as a function of MFB50 for the different cases of EGR (a) and WI (b). Engine point shown corresponds to 2400 rpm and 2.2 NL.

To identify how much EGR and WI increase combustion duration, a comparison is made between the duration when applying a certain EGR or *r* and that of when none of these is used, that will be named ΔCombustion Duration. Equation (2.3) shows how ΔCombustion Duration is calculated.

$$\Delta Combustion\ Duration = (MFB90 - MFB10)_{EGR,r} - (MFB90 - MFB10)_{EGR=0,r=0} \quad (2.3)$$

Using data from Figure 2.14, ΔCombustion Duration curves are calculated using the very same procedure implemented for the ΔSA and ΔEGR curves shown previously, meaning that the ΔCombustion duration is calculated considering a fixed value of MFB50 at each engine point and for each value of EGR and *r*. Figure 2.15 shows a comparison between EGR and WI for the engine point of 2400 rpm and 2.2 NL. There is a great similarity in the values of Figure 2.12 and Figure 2.15, meaning that the ΔSA is almost equal to the ΔCombustion Duration. Since the ΔSA is the one needed to maintain a fixed MFB50, the similarity between these two figures indicates that most of the increase in combustion duration occurs between the start of combustion and MFB50, and not between MFB50 and MFB90. This could be explained by the fact that being the initial stage of combustion the slowest (also that with the lowest temperature [57]), mixture dilution has a greater impact on such stage.
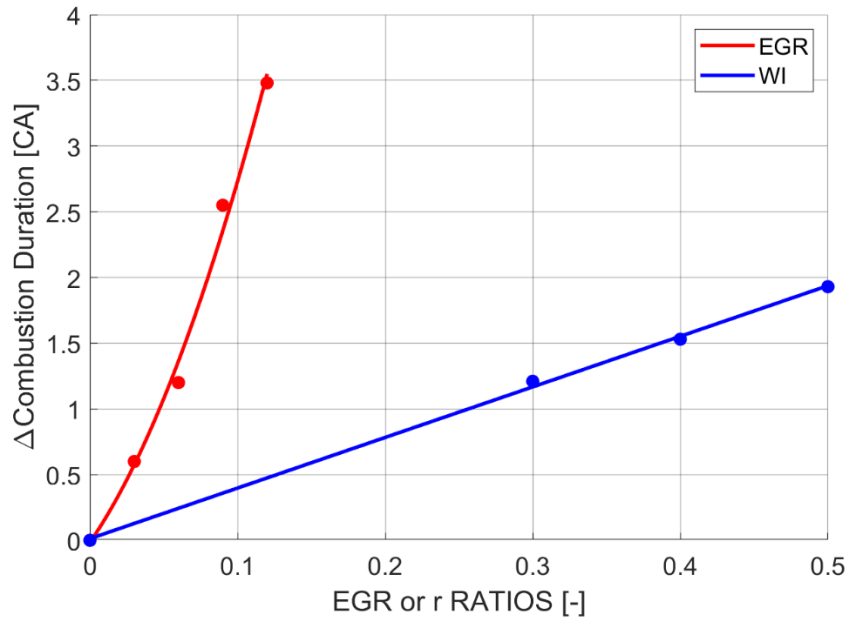
Figure 2.15 - ΔCombustion Duration as a function of EGR and r for the cases of LP-EGR and WI (when used separately). This represents the CA interval increase of MFB10-90 (with respect to no EGR nor WI), for a constant MFB50. Engine point shown corresponds to 2400 rpm and 2.2 NL. EGR and WI are expressed as fractions.

Figure 2.16 (a) shows the correlation between ΔCombustion Duration and ΔEGT, for both EGR and WI and for the same operating condition of Figure 2.15. A linear trend clearly emerges in which the slope for both solutions is very similar. This characteristic could be attributed to the fact that being a high load engine point, temperature in the intake runner is high enough to cause most of the water to evaporate in the intake runners and not inside the cylinder. When looking at lower load points for the same engine speed, such as the one reported in Figure 2.16 (b), a slightly steeper slope was observed, possibly indicating that in such cases more water was evaporating inside the cylinders (further contributing to EGT cooling) rather than in the intake runners [17].
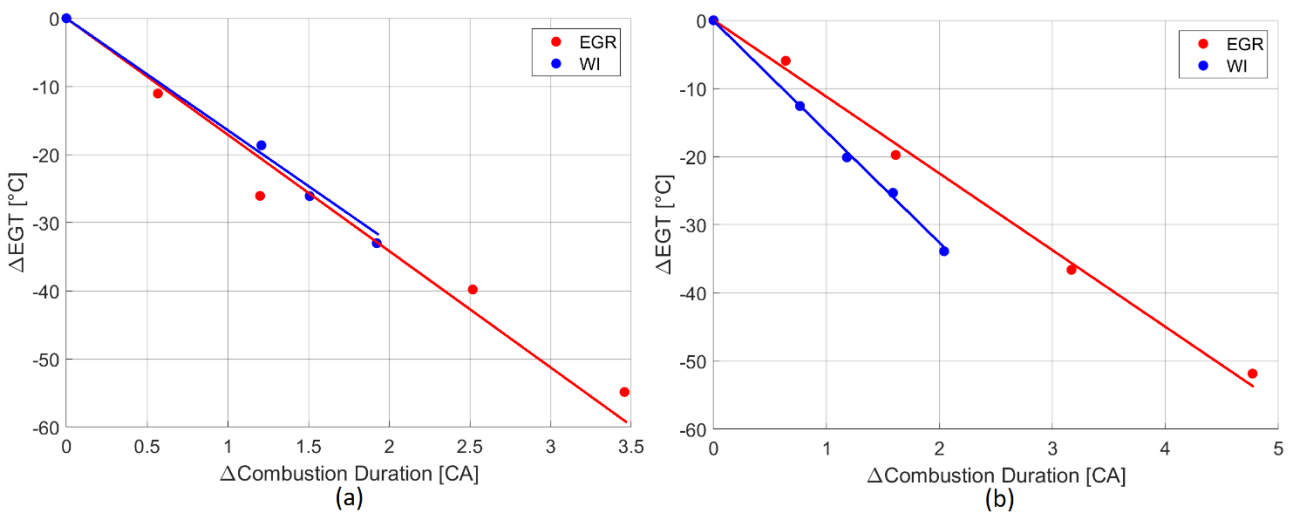
Figure 2.16 - Correlation between ΔCombustion Duration and ΔEGT for engine point (a) 2400 rpm and 2.2 NL (b) 2400 rpm and 2 NL.

2.4   Limitations of cooled LP-EGR

In the previous paragraphs of this chapter, some of the limitations of the LP-EGR system have been mentioned. At high loads, a first limitation was identified by acknowledging that the volumetric flow and boost pressure that the compressor must manage is increased proportionally with the increase in EGR ratio (as shown in Table 2.1), leading to turbocharger speed issues and a performance cap given by turbocharger capabilities. A second limitation, at low loads, is the fact that there might be not enough pressure difference, between the gases after the TWC and the intake duct before the compressor, to produce the recirculated mass flow needed to achieve a desired EGR ratio.

Another factor that could impose a limit on the maximum EGR ratio is the increase of CoV of IMEP. This is dependent on both engine point and MFB50, but general trends have been confirmed for all engine points. Figure 2.17 shows a comparison between the CoV of IMEP evaluated while separately applying EGR and WI, at 3000 rpm and 1.8 NL. For a constant MFB50 value of 20 CA aTDC, similar effects on CoV are caused by EGR and WI, and the same happens when comparing values at an MFB50 of 25 CA aTDC. The CoV increase when using EGR or WI becomes more pronounced, with respect to the case of no EGR or no WI, when considering higher values of MFB50. Given that the MFB50 is typically retarded with increasing load (due to knock restrictions), this could impose a limitation on the maximum possible amount of EGR that can be utilized. Every manufacturer imposes its own CoV limit but nevertheless these plots show that LP-EGR is not more detrimental on combustion stability than WI, when the comparison considers ratios that produce similar cooling effects. As commented in the case of the needed intake manifold pressure increase shown in Table 2.1, this increase in CoV IMEP could impose a consideration for the redesign of engine components and calibration.
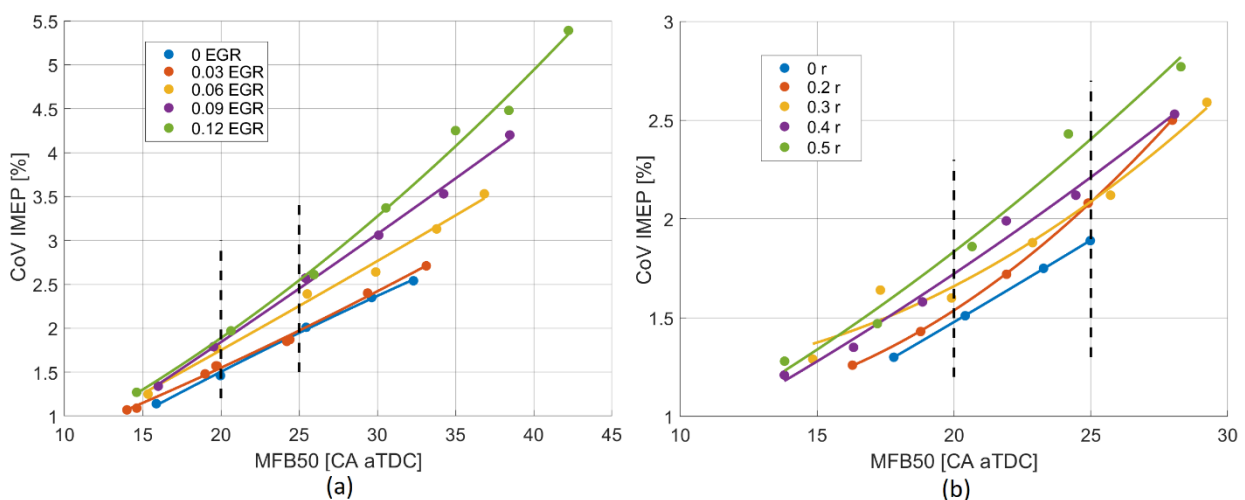
Figure 2.17 - CoV of IMEP as a function of MFB50, for the values of EGR (a) and WI (b) ratios. The engine point corresponds to 3000 rpm and 1.8 NL.

2.5 Synergy analysis of combined LP-EGR and WI

So far, EGR and WI have been compared by analysing the effects they produce when used separately. At the engine point of 3000 rpm and 1.8 NL, both technologies have been used simultaneously in search of a possible synergy. To do so, four SA sweeps were conducted by applying different combinations of EGR and WI ratios, and finally verifying whether the results obtained for each SA sweep were indeed equal or not to the sum of the observed effects of EGR and WI when tested separately. The four SA sweeps were designed with the following ratios of EGR and WI:

1. 0.03 EGR and 0.3 r.
2. 0.03 EGR and 0.4 r.
3. 0.09 EGR and 0.3 r.
4. 0.09 EGR and 0.4 r.

Three comparisons have been carried out, always considering the first case as baseline or reference test. The first comparison is between cases 2 and 1, in which only WI changes with an increment of 0.1 *r*. The second comparison is between cases 3 and 1, in which there is only a 0.06 increment in EGR. And finally, a third comparison was evaluated between cases 4 and 1, with a 0.06 increase in EGR and 0.1 in *r*. During all these comparisons it is verified if the observed combustion speed and EGT decrease are equivalent to the sum of those measured when testing EGR and WI separately, as shown in the previous sections of this work.

Figure 2.18 and Figure 2.20 show the experimental results for the four combinations of EGR and WI ratios, highlighting each comparison. Figure 2.19 and Figure 2.21 show the effects of applying EGR and WI separately. From these four figures, it can be verified whether the sum of the separate effects taken from Figure 2.19 and Figure 2.21 are equal to those observed in Figure 2.18 and Figure 2.20. The results of these comparisons are the following:

Comparison 1: $\Delta SA_1 = $ **0.5** CA $\quad \leftarrow \rightarrow \quad$ ΔSA WI = **0.6** CA
Comparison 2: $\Delta SA_2 = $ **2.9** CA $\quad \leftarrow \rightarrow \quad$ ΔSA EGR = **2.9** CA
Comparison 3: $\Delta SA_3 = $ **3.4** CA $\quad \leftarrow \rightarrow \quad$ ΔSA WI + EGR = **3.5** CA

Comparison 1: $\Delta EGT_1 = $ **5** °C $\quad \leftarrow \rightarrow \quad$ ΔEGT WI = **6** °C
Comparison 2: $\Delta EGT_2 = $ **27** °C $\quad \leftarrow \rightarrow \quad$ ΔEGT EGR = **28** °C
Comparison 3: $\Delta EGT_3 = $ **33** °C $\quad \leftarrow \rightarrow \quad$ ΔEGT WI + EGR = **34** °C
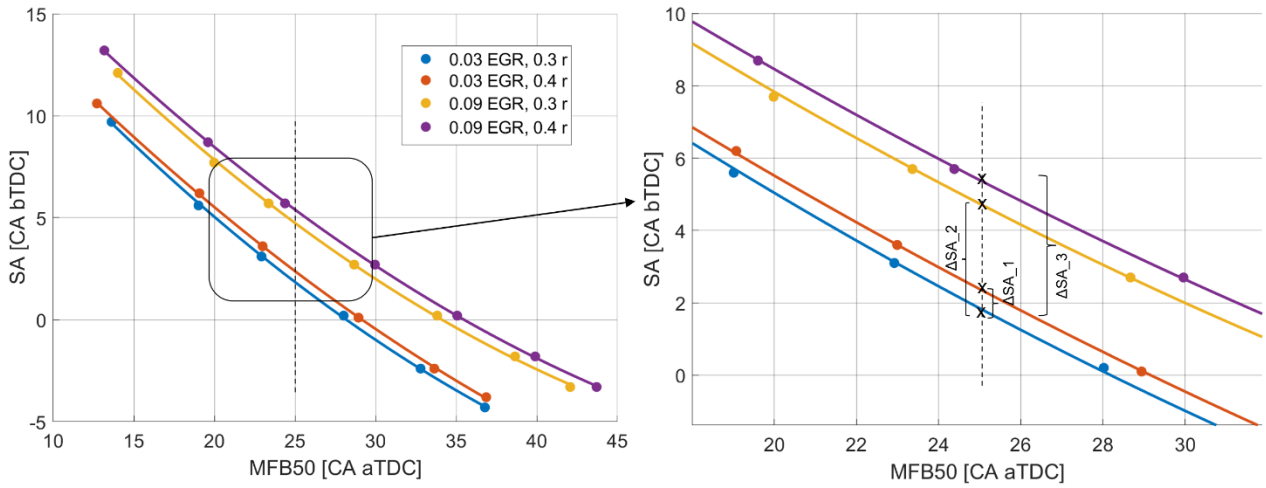
Figure 2.18 - SA sweeps for the various cases when using EGR and WI simultaneously. The engine point corresponds to 3000 rpm and 1.8 NL.
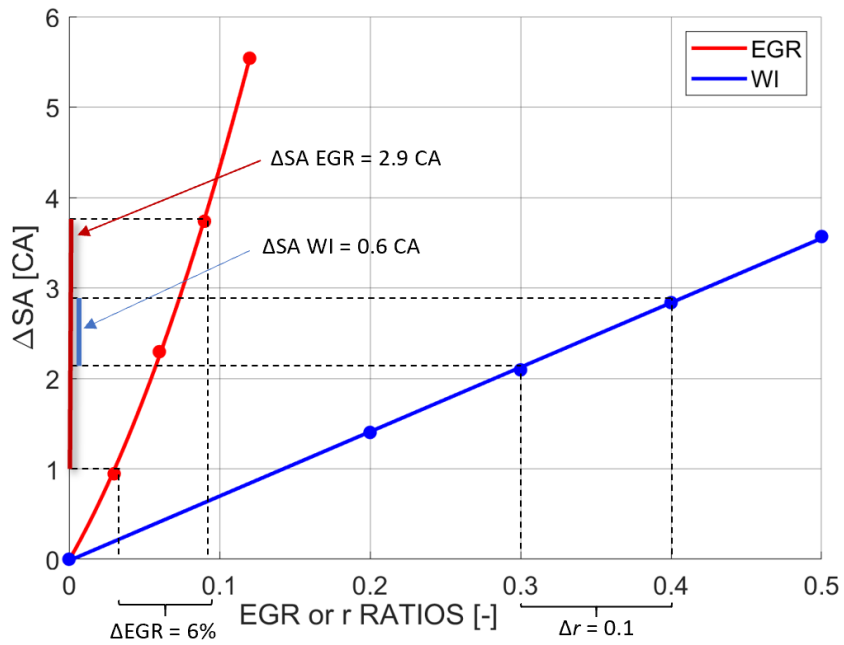
Figure 2.19 - SA increase needed to achieve a constant MFB50, when using EGR and WI separately (from previous tests). The engine point corresponds to 3000 rpm and 1.8 NL.
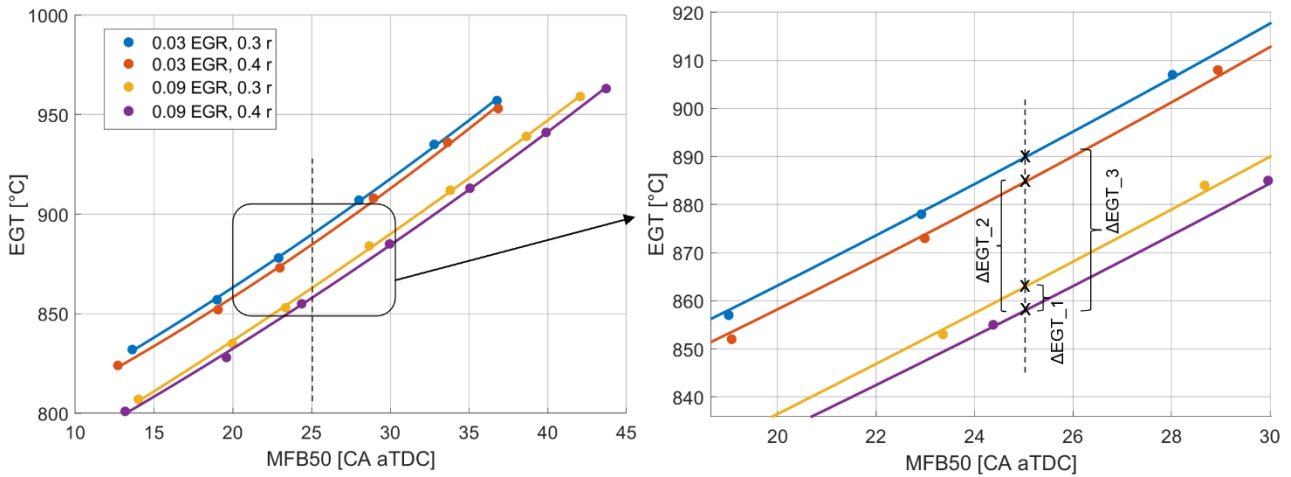
Figure 2.20 - EGT during the SA sweep for the four cases when using EGR and WI simultaneously. The engine point corresponds to 3000 rpm and 1.8 NL.
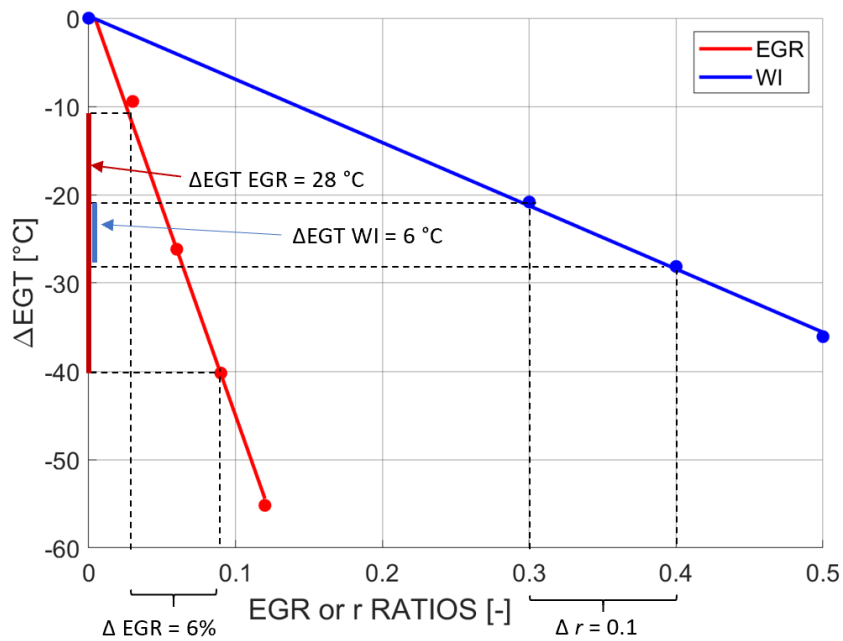
Figure 2.21 - EGT reduction at constant MFB50, when using EGR and WI separately (from previous analysis). Engine point shown corresponds to 3000 rpm and 1.8 NL.

These results show that the sum of the individual effects of EGR and WI are equivalent to those obtained when combining them and thus not presenting any kind of synergy. Both in terms of combustion phase delay and EGT reduction, the third comparison (combined increment of both WI and EGR) results to be the sum of the first and second comparisons (separate increment of WI or EGR, respectively), aside from a small difference that can be attributed to experimental errors and fitting of the curves shown in each plot.

2.6   Production engine performance comparison, LP-EGR vs WI

As a result of the extensive experimental work carried out on both LP-EGR and WI, the final objective of this study was to take advantage of the engine from Figure 1.22 and the fact that it had both technologies, and generate an engine calibration for each of these so as to extract the most performance out of the engine and compare the results of LP-EGR and WI in a close to production application. The criteria to generate the engine calibrations for each case were based on the results of the previous experimental campaigns, being mostly a knock-limited situation to determine the most anticipated SA value and the EGT limit of 950°C to determine the maximum admissible NL. To comply with the oncoming emissions regulations, EGR and r ratios were set accordingly within feasible on-board application limits to comply with the previously described knock and EGT limitations as well as allow for $\lambda = 1$ operation when using EGR and WI.

The results of this activity were three different calibration sets: A first one, called traditional, which corresponds to an engine calibration that does not use EGR or WI and uses the traditional approach of mixture enrichment for combustion gas cooling, and two other calibrations, one for EGR and another one for WI, that operate at $\lambda = 1$ while meeting the previously described criteria. The selection of the r and EGR values used by these calibrations is based on mainly two criteria. The first criteria aims to lower MFB50 as much as possible while keeping knock level below an established threshold, the second criteria is based on a series of industrial application constraints as for example not having excessive water consumption or guaranteeing a CoV of IMEP that does not exceed a certain threshold. The actual values of r and EGR that were used cannot be disclosed because of confidential reasons. The following figures shown the performance obtained from experimental tests at WOT using these three calibrations. For confidential reasons, values of torque and BSFC have been normalized with respect to the maximum value of the traditional approach.

Figure 2.22 shows how the traditional approach can achieve the highest performance in terms of torque, followed by WI and then EGR. The reason for this is that the usage of rich mixtures allows for adequate combustion gas cooling, but this is penalized by the greatly increased fuel consumption when compared to the other two calibrations, as shown in Figure 2.23. As explained in the previous paragraph, both the industrial constraints that limit the maximum r and EGR values as well as the impossibility to increase boost as much as it would be necessary to fully compensate the fresh air displacing effect, prevent these two calibrations from reaching the performance of the traditional approach. At low engine speeds, boost cannot be increased as much as necessary because turbine speed is not high enough to generate such boost. At high engine speeds, boost cannot be increased beyond a certain value because to create such boost the turbine would have to operate beyond its maximum allowed speed. WI gets closer than LP-EGR to the performance of the traditional approach, mostly because, as seen in Figure 2.25, higher values of NL and thus higher amount of fresh air into the cylinder are achieved with WI. The calibration with LP-EGR falls behind because of the forementioned limitations of compressor volumetric flow and thus not being able to introduce as much fresh air into the cylinder as in the case of WI or the traditional approach. As shown in Figure 1.25, achievable combustion

phase for the cases of WI and LP-EGR was similar, still better than the traditional approach, confirming what was stated on the conclusions of the previous chapter in which the advantage of these two technologies in terms of fuel consumption reduction, and especially WI, relies on the fact that mixture enrichment is avoided and not so greatly because of enhanced combustion phase.
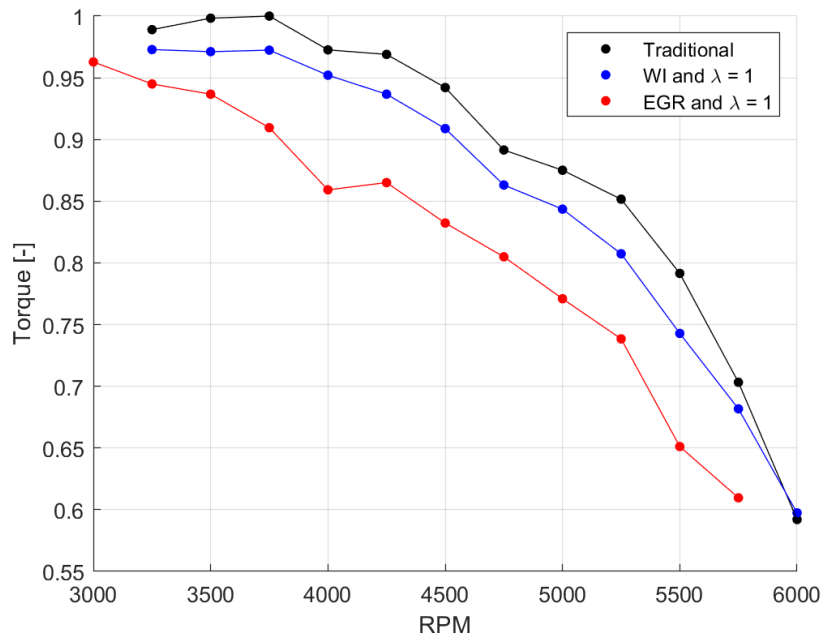
Figure 2.22 - Normalized torque for the three different calibrations.
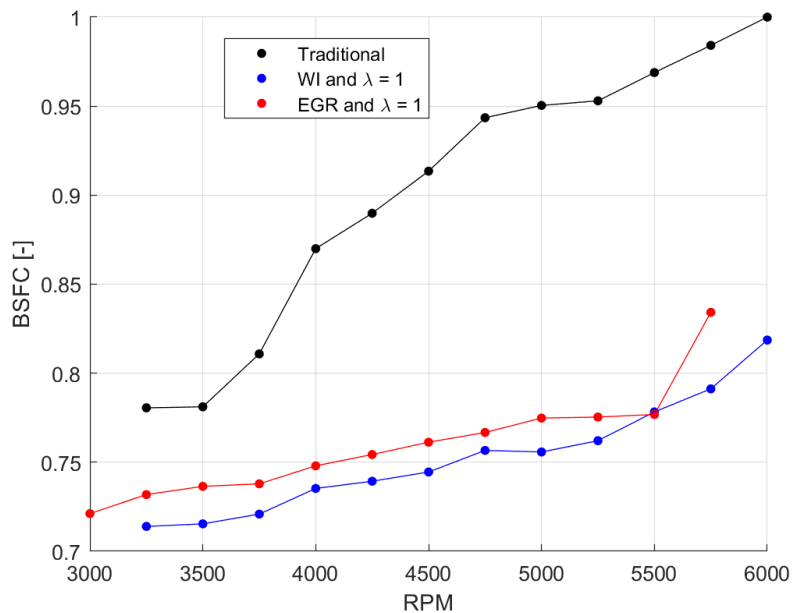
Figure 2.23 – Normalized BSFC for the three different calibrations.
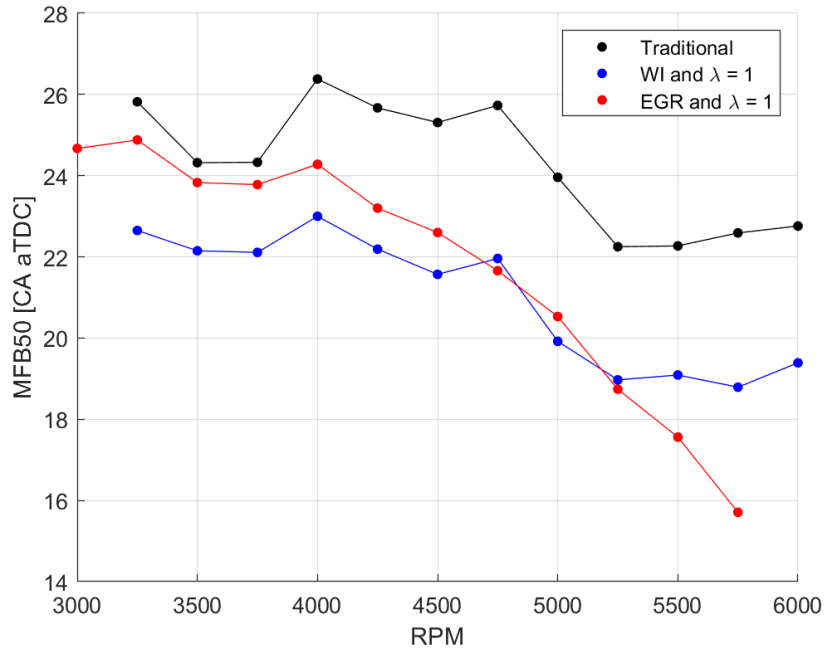
Figure 2.24 - MFB50 for the three different calibrations.
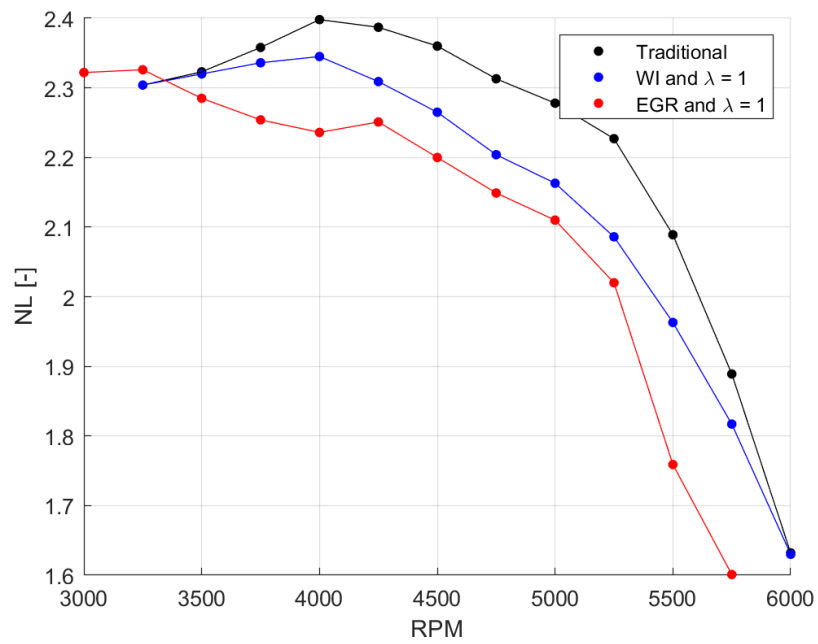
Figure 2.25 - NL for the three different calibrations.

2.7   Conclusions

In this chapter, the effects of LP-EGR on the main combustion indexes have been explored. SA sweeps have been carried out using different LP-EGR ratios, for mid/high load engine operation, where there is a high probability to reach and overcome the maximum gas temperature at the turbine inlet. This technology was tested first by itself and then simultaneously with WI in order to investigate a possible synergy between them. Differences have been identified also from a quantitative point of view, and limitations remarked.

The usage of LP-EGR has demonstrated to be an effective solution to lower EGT, achieving similar or even higher cooling capabilities when compared to WI. In terms of EGT reduction, an approximate five to one relationship was observed between water-to-fuel and LP-EGR ratios, meaning that for example a 0.03 EGR ratio produced the same effects of a 0.15 r ratio.

The main limitation of LP-EGR has been that the recirculated gas introduced into the combustion chamber consumes volumetric flow of the turbocharger that could be otherwise used to compress fresh air and thus increase even further specific-power production. This condition becomes a restriction for performance when the turbocharger speed arrives to its maximum and thus not allowing to further close the wastegate to manage the increased compressor volumetric flow due to EGR.

The increase in combustion duration has been identified as the main cause of EGT reduction for both EGR and WI, having the latter an additional contribution due to water evaporation in the cylinder which absorbs extra heat. The combustion phase delay and EGT reduction effects associated to EGR have been successfully modelled with low-order polynomial functions depending on EGR ratio and engine load. With this approach it is possible to calculate the amount of SA that must be added to compensate for combustion increased duration for a given ratio of EGR or r, and to predict the EGT decrease associated to it. As in the case of WI, the models can be inverted and used in a control strategy, by imposing a desired EGT and calculating the needed EGR ratio to be applied in order to achieve such desired EGT. During the experimental tests in which EGR and WI were used simultaneously in search of a possible synergy, it has been observed that their effects are essentially additive, and no significant interactions emerged. This applies to combustion phase delay and EGT reduction.

Finally, the comparison of engine performance with the three calibrations, one using the traditional approach of mixture enrichment, one replacing this latter with the usage of WI and a third one using LP-EGR, has confirmed that the main advantages of these technologies in terms of fuel consumption relies on the possibility to avoid mixture enrichment and not so greatly on enhanced combustion phase.

3 Combustion phase measurement via accelerometer

During Chapter 1, the advantages of replacing the traditional SA control strategy with a MFB50-oriented control strategy have been evidenced, from which the most important are the direct control of engine efficiency and torque delivery. The desire to investigate technologies towards a real-world production application is a trend that is present during all the work carried out for this thesis. Having said this, to finalize the possibility to apply the WICC on an on-board application, it is necessary to estimate MFB50 using on-board available equipment and with the lowest computational resources as possible so as not to overload a standard ECU.

Several authors have studied the estimation of MFB50 using different methods, some of which by using Analytical Neural Networks (ANN) as is the case of Zhu and Johnson [58,59]. Zhu et al [58] have investigated the possibility of estimating MFB50 using a neural network that uses RPM, intake Manifold Absolute Pressure (MAP), intake camshaft centreline, exhaust camshaft centreline and SA as inputs, and validated their model obtaining an estimation within 15% of the real value (Figure 3.1), as measured by an in-cylinder pressure sensor.
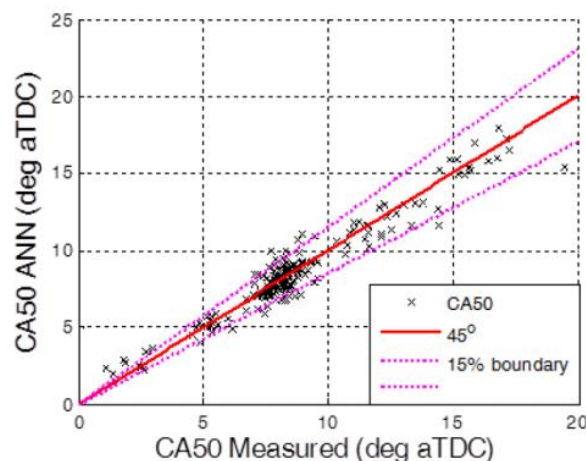
Figure 3.1 - Steady state performance of the CA50 ANN model. The ANN has a single layer and 10 neurons. Significant error can be observed in this plot which is intentional to illustrate the benefits of the correction approach. Source [58].

Other authors such as Aengeby et al [60] remark the still inexistence of an available widespread industrially available technique to estimate combustion phase. For this reason, they have studied the possibility of measuring MFB50 using the signal from an ion-current sensor and correlating it to the peak cylinder pressure. Results obtained by Aengeby show that he has been able to estimate peak pressure and thus combustion phase with an accuracy between 1.3 CA and 2 CA. Although the results obtained are valid, it is important to say that a very small amount of production engines possess an ion-current sensor, due to economical restraints, and thus making this application of limited scope.

Wang et al [61,62] have developed a virtual sensor, based on the thermodynamics of combustion, to estimate first the pressure in the cylinder (using MAP, fuel mass, residual gas mass, among others as input)

and then reconstruct the HRR to finally estimate MFB50. Figure 3.2 shows the RT validation of the method used by Wang, obtaining a mean RMSE of 3.6 CA. Though the good results of this study, the method remains as a proof-of-concept for the model-based combustion phasing control, but the MFB50 estimation results still too computationally intense for an on-board application.
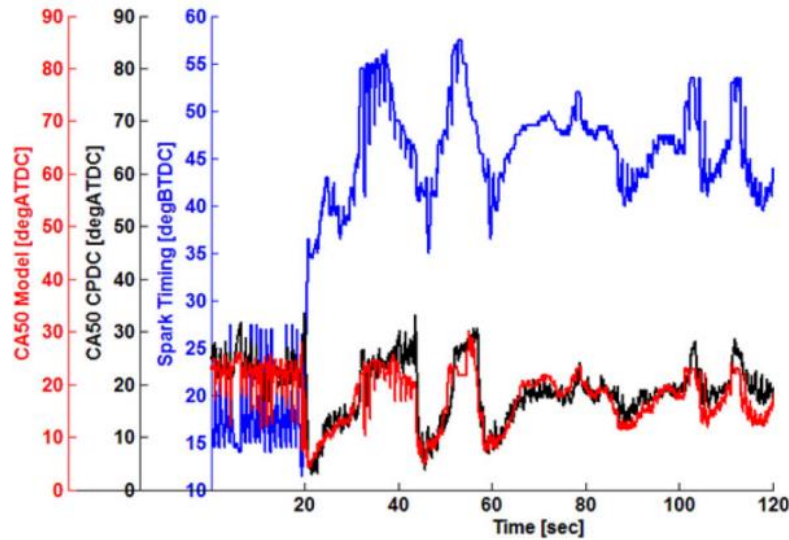
Figure 3.2 Real-time combustion phasing prediction system validation results (first 120 seconds of FTP driving cycle). Source [61].

Businaro et al [63] have studied how to use the accelerometric signal already available on-board to determine relevant parameters like maximum in-cylinder pressure, but did not try to estimate MFB50. Amezcua et al [64] have installed several accelerometers on a CIDI engine to detect MFB50 through the accelerometric signal and found that there was a correlation between the peak of the filtered accelerometric signal and the squared derivative of the in-cylinder pressure signal. However, the algorithm that they have developed was only able to produce marginal results with an $R^2 = 0.55$, reason why the authors retain that they needed to work on the optimization of the filtering of the signal. Ponti et al [65] have also studied the use of accelerometers on a CI engine, observing a correspondence of the angular position of the peak of the filtered accelerometric signal and the peak of Hear Release Rate (HRR). Nevertheless, Ponti remarks that it was difficult to carry out this detection when at low loads below 8bar of BMEP, because of high noise to signal ratio and low signal energy and retained that modifying the position of the accelerometer could have potentially improved results.

This chapter is dedicated to a new experimental campaign oriented to evaluate the possibility of estimating MFB50 angle by accelerometric signal, in which the novel contribution is its almost completely on-board available calculation methodology, meaning that both the signal acquisition and filtering chain as well as the computational tools for MFB50 estimation are already available in most production ECUs because of their application for on-board knock measurement. The main inputs for the closed-loop section of the WICC are MAPO98 and MFB50, being both measurements taken from the processing of the in-cylinder pressure signal, during the previously shown WICC validation campaign. With an on-board application as a goal, the

replacement of the in-cylinder pressure sensor with an on-board available alternative is necessary. Accelerometers are widely used to detect knock via a high pass filtering of the signal. This opens the opportunity to evaluate the possibility of using this very same signal, processed differently, for detecting combustion phasing as well. Previous studies demonstrated that there is a significant correlation between the angular position of in-cylinder pressure peak derivative and MFB50 [63], reason why the first step of the analysis is to determine if the accelerometer can generate a signal that is able to identify this pressure derivative peak. This investigation demonstrates the feasibility in obtaining feedback on MFB50 by using the accelerometric sensors available on-board, already used for knock detection, and using a similar signal processing than that used for knock to take advantage of the already available ECU signal processing algorithms.

The work presented in this chapter has been published as part of this PhD research activity results in [36].

3.1   Experimental setup

The development of MFB50 estimation algorithm based on accelerometric signal has been developed on the engine displayed in Figure 1.22 whose characteristics are displayed in Table 1.4. The engine was equipped with two accelerometers as standard production equipment, one located between cylinders 1 and 2 (Acc12) and the other located between cylinders 3 and 4 (Acc34). The accelerometric signal was acquired with the same instrumentation that was used to acquire the in/cylinder pressure sensors, using a sampling frequency of 200 kHz.

3.2   Preliminary signal analysis

As already mentioned, it is known that there is a correlation between the angular position of the peak of the derivative of the in-cylinder pressure signal and MFB50. For this reason, the first step was to observe if the signal from the accelerometers contained information related to such peak position.

A vast number of experimental tests at different engine points have been carried out, ranging from 1500rpm to 5500rpm and values of NL that range between 0.4 and 1.4. During these tests, both in-cylinder pressure sensors and accelerometers signals have been recorded.

A first processing of the accelerometric signal was made to understand the range of the main frequencies related to combustion phasing. Contrary to knock, characterized by frequencies above 5 kHz, components of the accelerometric signal that can be used to identify combustion phasing are found in a frequency domain that can be as much as five times lower. A first analysis was made, using a 4th order

Butterworth low pass filter with a cut-off frequency of 1 kHz. Figure 3.3 shows the results of this processing, from which it is immediately observed that near the peak of the derivative of the in-cylinder pressure signal related to a combustion event, there is a corresponding accelerometric signal peak as well. This implies that there is the possibility to directly correlate the position of the accelerometer peak and MFB50. As shown in Figure 3.3, the peak is more relevant for the cylinders located near to the sensor analysed. To ensure a more precise peak detection, its identification is carried out inside an angular window within which the combustion occurs, excluding all the rest of the cycle phases.
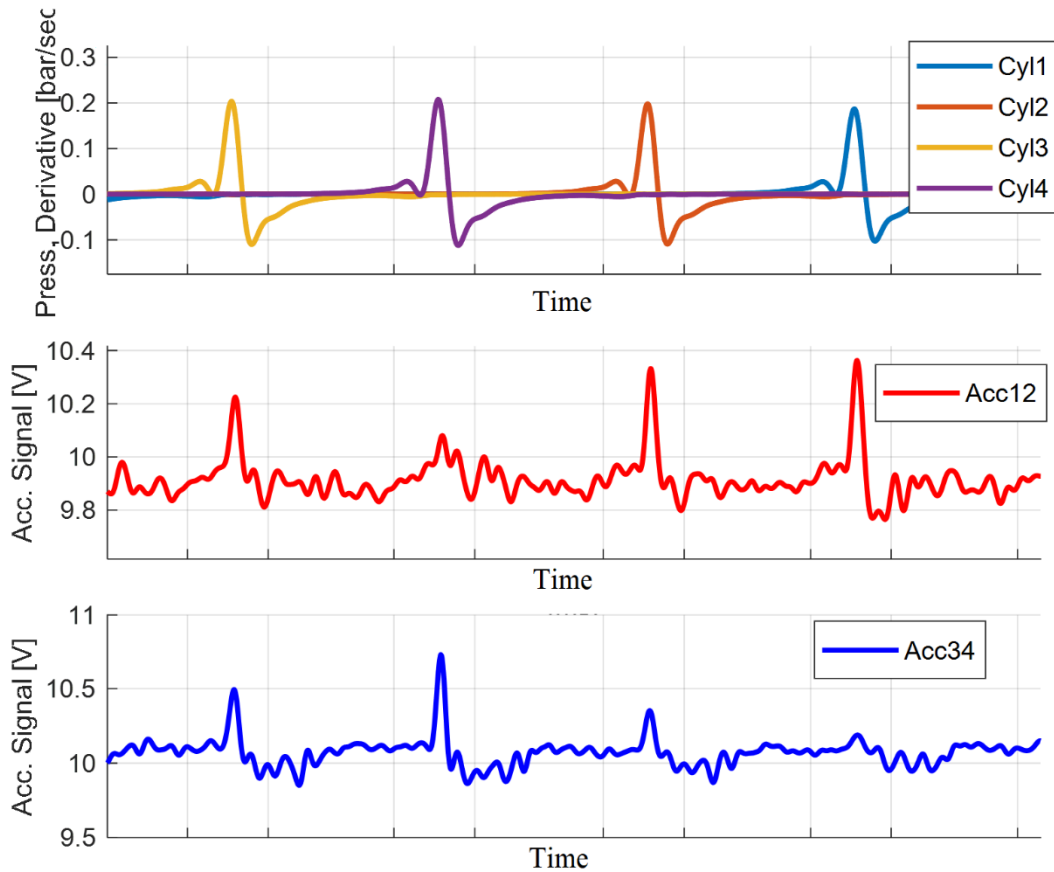
Figure 3.3 - On top, derivative of in-cylinder pressure signal. In the middle and in the bottom, filtered accelerometric signal from the accelerometers (low pass 1 kHz), 1500rpm and 1.2NL.

From this preliminary analysis, which was repeated for different engine operating conditions and using different low-pass cut-off frequencies, two observations can be made. The first is that there is a time (and thus angular) delay between the peak of the pressure signal and the one from the accelerometric signal. The physical explanation relies on the fact that the vibrations from the instant of maximum in-cylinder pressure must mechanically travel through the engine block before arriving to the accelerometer sensor. This process takes time and generates a delay between the physical event in the combustion chamber and its detection by the accelerometer. This delay is constant in the time domain because it corresponds to the propagation of the vibrations across the engine block but given that the algorithm must be able to work in the angular domain and an ample RPM range, it is no longer constant when converted into an angular value and depends on RPM. For this reason, the called Angular delay must be adequately identified for each RPM case. The second observation

75

is that the cut-off frequency used on the low pass filtering process of the accelerometric signal impacts on the correlation between its peak and the location of MFB50. This implies that there is the need to generate a map with the cut-off frequency that maximizes correlation at each engine point.

As an example, Figure 3.4 displays the results from the filtered accelerometric signal where the angular delay corresponds to the angular difference between the red or blue points (Acc. Peak) and the dashed line, for a fixed combustion phase. Equation (3.1) shows how Angular delay can be calculated as the mean value of such parameter for all the considered engine cycles.

$$Angular\ delay = \sum_{i=1}^{N} \frac{(Acc.Peak - MFB50meas)_i}{N} \tag{3.1}$$

Where *Acc.Peak* is the position of the maximum value of the filtered accelerometric signal inside the angular window and *MFB50meas* is the MFB50 measured with in-cylinder pressure sensor, both registered in same cycle. Therefore, once the *Acc.*Peak has been identified, the estimation of MFB50 by accelerometric signal (for each cycle) can be obtained by using Equation (3.2).

$$MFB50est = Acc.Peak - Angular\ delay \tag{3.2}$$

Figure 3.4 displays the data points acquired with the filtered signal of the accelerometers, obtaining a correlation of over 90% between accelerometric signal peak and measured MFB50 from indicating system. All the forthcoming results are obtained using the accelerometer positioned between cylinders 1 and 2 for observing the same two cylinders, and in the same way the other sensor has been used for cylinders 3 and 4. General trends show that at mid and high loads, correlation remains above 90% while at low loads (NL < 0.6), the accelerometric signal is not able to generate a distinctive peak due to a lack of combustion intensity, resulting in a correlation below 50%. Given that this study has been conducted to develop a methodology that would allow to measure MFB50 on-board, mainly with the objective of its implementation on the MFB50 closed-loop branch of the WICC, the focus is put in achieving a high correlation in the mid-high load region with $NL \geq 1$.
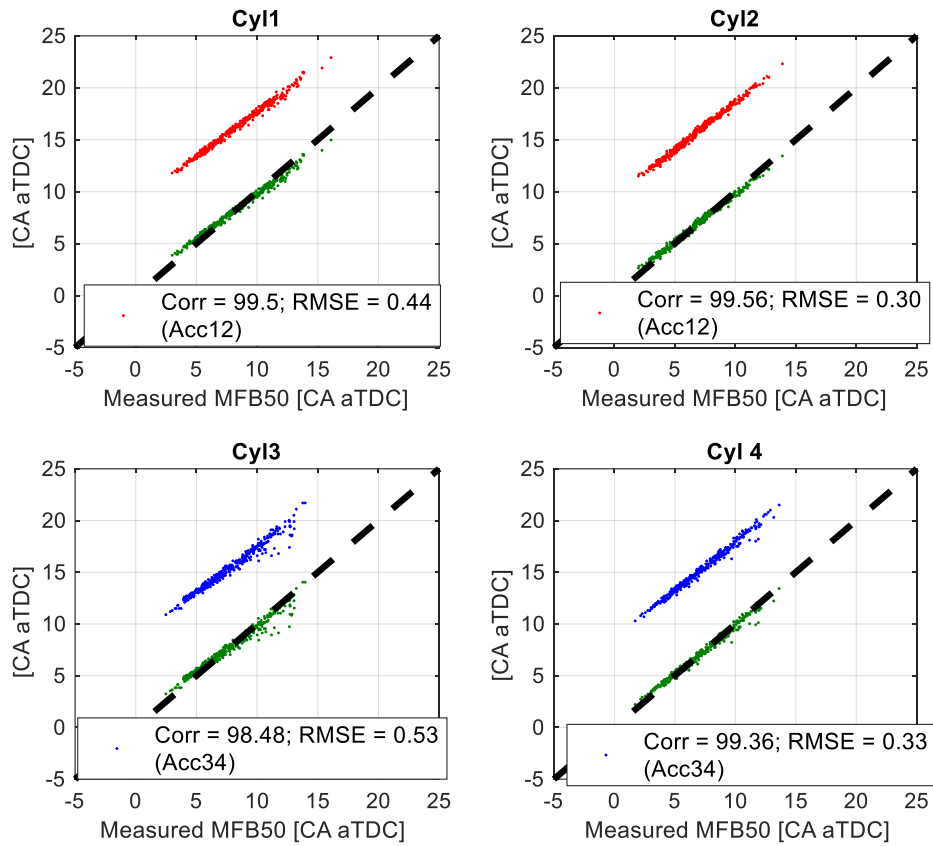
Figure 3.4 - Correlation between accelerometric signal peak position and MFB50 measured with in-cylinder pressure sensor. RPM2500 NL 1.1. Red and blue dots represent the correlation obtained without angular compensation (red=Acc12; blue Acc34). Green dots represent the correlation after the application of the angular delay compensation (MFB50 estimated).

3.3   Signal processing algorithm and calibration

Once established that it is possible to estimate combustion phasing with accelerometric signal, an algorithm is designed in order to obtain the best results at each engine point. The strategy consists in signal windowing to focus on the combustion phase, a low-pass filtering stage, peak recognition and angular delay compensation (Figure 3.5). Consequently, the algorithm has been calibrated by following three steps:

- windowing of the accelerometric signal to be processed
- selection of the cut-off frequency for signal filtering
- angular delay identification.

Signal windowing has been imposed from 5 CA until 70 CA after spark event, interval in which accelerometric signal peak is generally located. Regarding the other two factors, optimum cut-off frequency and angular delay are identified and mapped for each of the tested engine points, process that is explained in the following paragraphs.
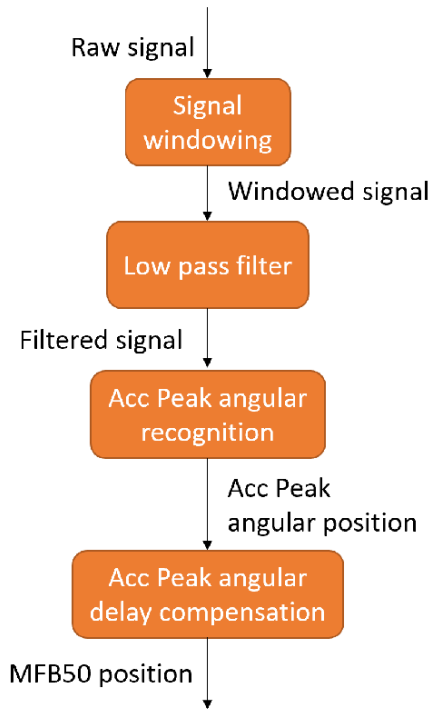
Figure 3.5 - Block diagram of accelerometric signal processing algorithm.

To evaluate the performance of the algorithm, the RMSE is calculated for each engine point to determine the angular error between the estimation of MFB50 by accelerometric signal and that calculated by the indicating system. Equation (3.3) shows how this calculation is done.

$$RMSE \ = \ \sqrt{\frac{\sum_{i=1}^{N}(MFB50est - \overline{MFB50meas})_i^2}{N_{Cycles}}} \tag{3.3}$$

As a first procedure, a sweep of cut-off frequencies is made at each engine point to find the frequency that minimizes the calibration RMSE. Figure 3.6 displays the results for several cases of load at 2500rpm as an example. This optimal cut-off frequency is not equal for all four cylinders and, as predicted, it depends on both engine speed and load, and ranges from 500 Hz to 900 Hz. After this analysis, optimal cut-off frequency values were identified as a function of RPM, as shown in Table 3.1, to simplify the algorithm implementation, once it was determined that engine speed was the main influencing parameter.
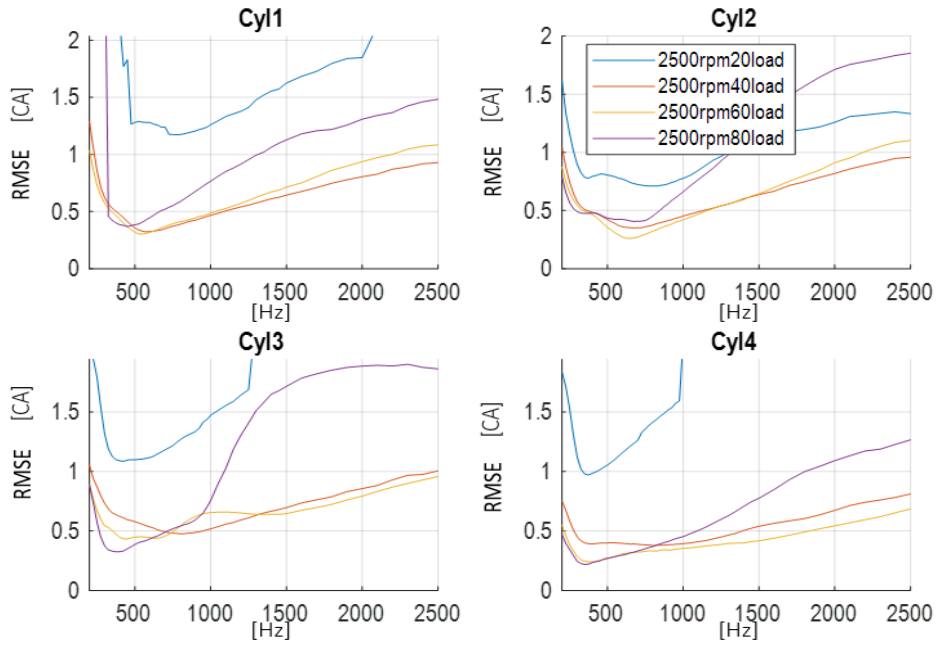
Figure 3.6 - RMSE vs Cut-off frequency for 2500RPM and different cases of load.

Table 3.1 - Cut-off frequency [Hz] map.

NL\RPM	1500	2500	3500	4500	5500
80		600	700	800	
60	500	600	700	800	900
40	500	600	700	800	900
20	500	600	700	800	900

The cut-off frequency for each engine point in the grid is identified and mapped, and the angular delay associated to each cut-off frequency is mapped as well. The final result is represented, for a specific engine operating condition, by the green points of Figure 3.4 that are shifted towards the black dashed line after the application of the mapped angular delay (and after the signal had previously been filtered with a 600 Hz cut-off frequency, the optimal one for such engine speed).

The tables below contain the results of the algorithm applied to each tested engine point, in just one cylinder as an example. As it can be seen, correlation coefficients seen in Table 3.2 are above 95% in most of the cases. Table 3.3 displays the RMSE for all tested engine points, which remains mostly under the pre-established limit of 1 CA, but some operating conditions at high speed exceed this limit. A general trend has been observed in which over a certain limit of RPM, the accelerometric signal starts to be affected by vibrations from other sources that impact the accuracy of the MFB50 estimation. These vibration disturbances in the signal could not be eliminated with filtering because they lie in the same frequency spectrum of the filtered accelerometric signal.

NL\RPM	2000	2400	3000	3600	4000	4400	5200
0.6	98.1	98.3	98.7	98.3	97.6	95.0	93.7
0.8	99.1	99.5	99.3	99.0	98.8	96.7	94.8
1.0	99.5	99.1	99.5	99.2	99.0	98.6	95.9
1.2	99.3	99.3	99.4	99.2	98.5	98.5	96.5
1.6	\	98.9	98.8	98.3	97.6	\	\

Table 3.3 - RMSE in CA degrees for the estimation of MFB by accelerometric signal.

NL\RPM	2000	2400	3000	3600	4000	4400	5200
0.6	0.80	0.90	0.60	1.00	0.90	1.30	2.60
0.8	0.60	0.80	0.70	0.50	0.70	1.20	1.90
1.0	0.40	0.50	0.50	0.40	0.60	0.70	1.80
1.2	0.30	0.30	0.50	0.40	0.90	0.40	1.60
1.6	\	0.40	0.50	0.50	0.60	\	\

3.4   Conclusions

In this section, MFB50 estimation by accelerometer signal processing was evaluated over a wide operating range of a 2L turbocharged GDI engine. At first, a correlation was found between the peak of the low-pass filtered accelerometric signal and MFB50, highlighting that there is a time and angular delay between the peak of the accelerometric signal and MFB50 and that using different cut-off frequencies when filtering the signal, depending on the engine operating conditions, could significantly improve the results of the estimation. For this, an analysis was carried out on all tested engine points, to identify the cut-off frequency that maximized the correlation for each of them, and a map of cut-off frequency was then generated (ranging from 500Hz to 900Hz), depending on engine speed. After this, the angular delay was identified for each engine point, generating again a map for the explored operating range. Using the identified maps, it was determined that MFB50 could be estimated with a correlation always higher than 95%, and a RMSE below 1 CA except at relatively high engine speeds.

To summarize the procedure, the algorithm first extracts a portion of the accelerometric signal (windowing stage) between 7 CA and 70 CA after the spark event of the given cylinder, then it uses a pre-defined cut-off frequency to apply a low pass filter to the windowed signal, and finally it determines the peak of the filtered signal and it applies an angular offset corresponding to the angular delay identified in the pre-calibrated map.

The main advantage of this approach with respect to a model-based one is that the acquisition of the accelerometric signal is already present in most ECUs for knock detection and even the window in which the signal must be acquired is also similar (window used for knock is usually 0 CA to 90 CA from firing TDC).

Also, the filtering functions already used for knock can be used also for the MFB50 estimation, with different cut-off frequencies. Apart from the signal acquisition and windowing, functions already present in the ECU, the remaining parts of the algorithm that need to be added are the cut-off frequency map and the angular delay map. This allows for the complete algorithm to require low additional computational resources to the ECU, which is a key factor when considering production applications.

4   Virtual sensor to estimate maximum in-cylinder pressure

As mentioned during the introduction of this thesis, one of the biggest challenges to overcome to further improve the reliability and efficiency of modern SI engines is knock mitigation, which is highly correlated to the Maximum In-cylinder Pressure (Pmax) [66–68]. The main aspects that have motivated the development of this virtual sensor were that the availability of an estimation of the Pmax can be used not only to assess the mechanical stresses to which the engine is subjected [13] but also as an input in a predictive knock model to accurately calculate MAPO index [69]. This predictive model is of great relevance for the estimation of engine damage associated to a given combustion phase and engine knock level, allowing to generate a knock controller that controls both combustion phase for increased efficiency and engine damage associated to the different knock levels [70,71]. With such applications in mind, it becomes clear that the main intention of the development of the virtual sensor for estimating the Pmax was that of its integration in a control strategy that controls combustion phase to extract the most efficiency from the engine and at the same time considers engine damage, for which an accurate estimation of Pmax is key.

Authors such as Cavina, Ceschini and Nates [13,20,66] reported typical knock damages and the relations between knock intensity and the engine rings damage. To define a reliability threshold avoiding knock, Panzani et al. [68] developed an index able to set the unsafe limit conditions for the engine based on the in-cylinder pressure measurement. The high cost and low durability of in-cylinder pressure sensors have always prevented their application on production engines. For this reason, it is key to be able to estimate Pmax without the need of an in-cylinder pressure sensor, to elaborate a knock control strategy.

Authors such as Kulah [72] have developed a virtual pressure sensor for a CI engine with the aim of reconstructing first the entire pressure trace, then the HRR curve and finally estimate other engine parameters such as IMEP. Some results of this study are shown in Figure 4.1 in which Kulah was able to reproduce the pressure trace, but the algorithm for doing so is based on the physics of combustion and thus computationally very demanding. Apart from such limit, the mentioned RMSE of 4.4 bar appears to be acceptable for a CI engine with pressure peaks of over 150bar.
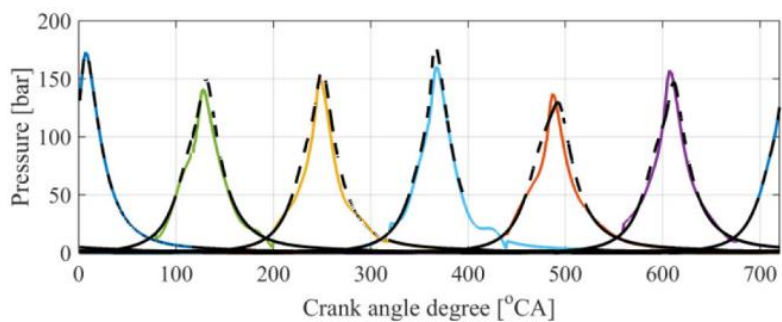
Figure 4.1 – Pressure trace reconstruction on all four cylinders of a CI engine. Source [72].

Rugland et al [73] developed a similar virtual sensor, based on physics of the gases inside the cylinder, to reconstruct the pressure trace, and validated it using data from a CI engine. Even though they seem to have been able to correctly reproduce the waveform of the pressure trace, as seen in Figure 4.2, they do not specify the accuracy at which they are able to estimate Pmax or even the RMSE.
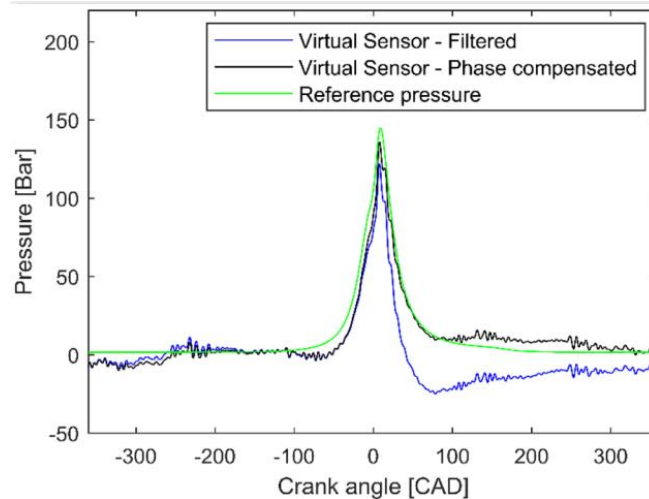
Figure 4.2 - Reference cylinder pressure (green), VS signal with (black) and without (blue) phase lag compensation. Source [73].

Other authors [74,75] have discussed the development of virtual sensors for the same purpose, not only for the estimation of Pmax, and have mostly chosen ANNs as the main solution for the estimations of interest.

This chapter focuses on the development of a data-driven model capable of predicting the maximum in-cylinder pressure during the operation of an internal combustion engine. The novel content of this study lies in the mathematical simplicity of the model (i.e., RT capability), the extremely low requirements for its calibration, and on the wide variety of data coming from different engines and conditions that were used for the model validation. The model is in fact based, for the majority of the engines that were tested, on only two operating parameters, engine load and combustion phase. Experimental data from four different gasoline engines, two turbocharged GDI SI, a NA SI and a Gasoline Compression Ignition (GCI) engine, were used to calibrate and validate the model, demonstrating its general validity. Some of these engines were equipped with technologies such as LP-EGR and WI or a compression ignition type of combustion in the case of the GCI engine. A vast amount of engine points were explored in order to cover as much as possible of the operating range, to confirm the broad applicability of the model. The validation process was carried out using both mean data from each explored engine point as well as cycle-by-cycle data, focusing on on-board application and the model implementation in a RT combustion control strategy. The validation also includes lean operating conditions for one of the SI engines. In all cases, the model demonstrated to be accurate within 5% when considering both mean values and cycle-by-cycle data, while retaining its simplicity and low computational weight. Additionally, a study on the minimum amount of engine points necessary for the model calibration has

been conducted and it was concluded that only about 20 engine points are needed, if chosen strategically as regards engine load and combustion phase.

Each of these engines has been instrumented with in-cylinder pressure sensors to be able to first calibrate the model and then validate it. To evaluate the model's performance, a comparison between the estimated Pmax from the model and the measured one obtained from the sensor has been performed. Given that one of these engines possesses a WI system and a LP-EGR system, it has been evaluated whether it is necessary to include them as inputs to the model to improve accuracy. Additionally, lean operation has also been explored to determine if the model remains valid in such case or if it is needed to include λ as an input as well. A similar situation occurred in the case of the GCI engine, where given the prototypal nature of the engine, other variables such as intake manifold pressure and fuel rail pressure (Prail) varied substantially during the tests, highlighting the need of their addition as inputs to the model.

Most of the results of this section have been published in [76].

4.1   Experimental setup

The experimental data used for the identification of the model and its subsequent calibration and validation is based on four gasoline engines (their main characteristics are displayed in Table 4.1):

- Engine 1: Four-cylinder 2.0L Turbocharged GDI equipped with LP-EGR and WI.
- Engine 2: Two-cylinder 0.9L Turbocharged GDI.
- Engine 3: Three-cylinder 1.0L Naturally Aspirated GDI.
- Engine 4: Four-cylinder 1.3L Turbocharged GCI.

Table 4.1 - General characteristics of the tested engines.

	Engine 1	Engine 2	Engine 3	Engine 4
Engine displacement [cc]	1995	875	999	1248
Number of cylinders	4	2	3	4
Bore [mm]	84	80.5	70	69.6
Stroke [mm]	90	86	86.5	82
Compression ratio	10:1	10:1	10.5:1	16.8:1
Valves per cylinder	4	4	2	4

In-cylinder piezoelectric pressure sensors were installed in each of the four engines and the pressure signals have been acquired using AVL's IndiCom indicating system, at a frequency of 200kHz. The pressure signal was used for the calculation of the main combustion indexes such as the MFB50, IMEP, Pmax, among others. An ETAS module along with INCA software was used to communicate with the ECU and to log the main engine parameters of interest such as SA, throttle position, EGR and WI ratios, lambda, intake manifold pressure, among others. Engine load is represented by the variable NL as in the previous sections.

Engine 1 was that of Figure 1.22 and the data used for it was that produced during the WI and EGR studies of the previous chapters. Engine 2 is a standard turbocharged two cylinder engine and engine 3 is a standard NA engine. The equipment and methods for the measurement of combustion indexes and control of engine variables remains the same as the one described for engine 1. Engines 2 and 3 are conventional gasoline engines, reason why no specific description is made. As regards engine 4, a GCI combustion system was developed starting from a standard light-duty 1.3L diesel and adding a PFI injection system. As well known, to keep GCI combustion stable a proper control of intake conditions is needed. In this way, engine 4 was modified also adding an external supercharger and air cooler, generating the necessary thermodynamic conditions of air pressure and temperature which allow the gasoline to auto-ignite. A simplified scheme of this engine layout is shown in Figure 4.3.
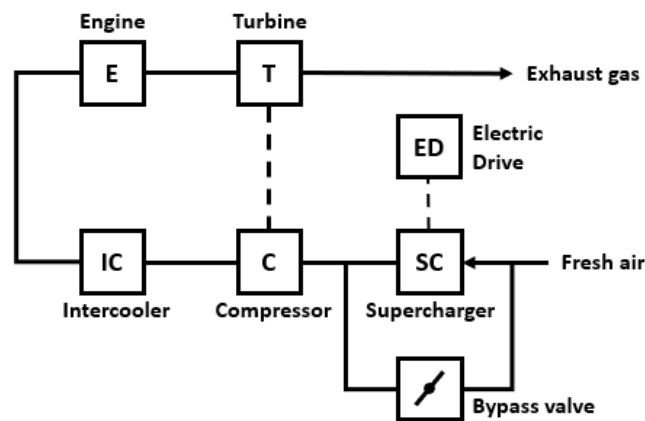
Figure 4.3 - Simplified scheme of the experimental setup of engine 4.

Unlike previous control layouts, which overwrite actuations to the main ECU, to properly control GCI combustion a full bypass approach for engine control is needed. Based on a fully programmable ECU, provided by Alma Automotive, it has been possible to test GCI combustion by varying main control parameters such as Start of Injection (SOI) angles, number of injections, fuel rail pressure and boost pressure. As for the standard gasoline engines previously described, to obtain the main combustion indexes also engine 4 was equipped with 4 piezoelectric in-cylinder pressure sensors. Moreover, custom pressure transducers and thermocouples were added on the intake and exhaust runners, collecting further information on the engine behaviour such as exhaust temperature and pressure, and temperature before and after the intercooler.

4.2   Model development and validation

Initially, the model was identified and tested on engine 1, following further validation on the other three engines. Experimental tests consisted mainly of SA sweeps at different values of engine speed, load and other variables such as EGR and WI ratios, as explained in the previous chapters. The experimental data consists of both mean values and cycle-by-cycle values. In the case of mean values, data was logged after reaching the desired engine point and then averaging two hundred consecutive cycles. In case of variables that present an individual cylinder behaviour such as MFB50, IMEP, PMAX, among others, the mean between the measurement of all four cylinders, called mean cylinder, was considered.

4.2.1   Engine 1: Model determination and validation

The identification of the mathematical function that is used to describe the Pmax has come as a result of a broad analysis (for which engine 1 was initially used) of the influence of the main combustion indexes on Pmax. The conclusion that arose from this analysis was that the two parameters that were the most influent were engine load (represented by NL) and combustion phase (represented by MFB50).

Four experimental campaigns were carried out on this engine. The first one, called below as Dataset PQ, consists of an exploration of an ample area of the operating range of the engine, using a base calibration that already uses WI at some mid and high load points. Each RPM and NL case on this dataset is a single case of SA and r, no sweeps were carried out. The second campaign, called Dataset WI, consists of SA sweeps within a r sweep, for different cases of RPM and NL, exploring only the region of mid and high loads. The third campaign, called Dataset EGR, consists of SA sweeps within an EGR sweep, for different cases of RPM and NL, exploring only the region of mid and high loads. The fourth campaign consisted of SA sweeps for different values of λ, towards lean conditions, at mid loads. Figure 4.4 shows the RPM and NL distribution of the first three campaigns. It is to be noted that, as explained previously, some of the points in Figure 4.4 contains a single SA, EGR and r combination (case of Dataset PQ) or a sweep of SA and EGR or r (case of Dataset WI and Dataset EGR). Figure 4.5 shows an example of SA sweeps performed during EGR and r sweeps.
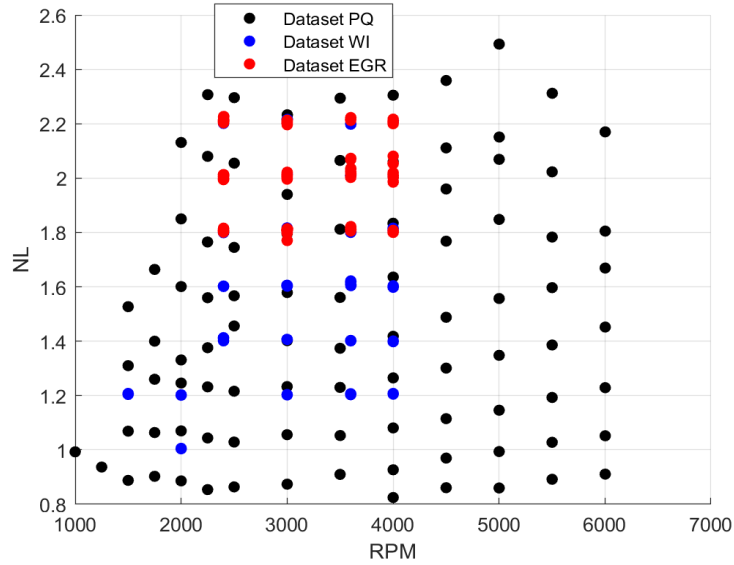
Figure 4.4 - Explored engine points on the experimental campaigns of engine 1.
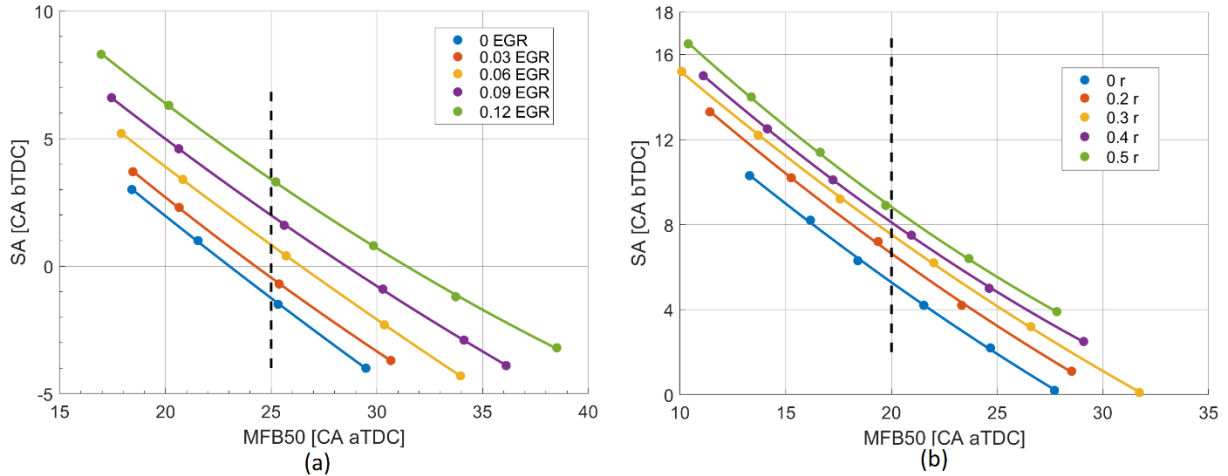
Figure 4.5 - Example of SA sweeps within an (a) EGR sweep in the case of Dataset EGR at 3000 rpm and 2 NL and (b) r sweep in the case of Dataset WI at 3600 rpm and 1.6 NL.

Figure 4.6 shows the logged data from the first three datasets when Pmax is plotted as a function of MFB50 and NL. Pmax has been normalized with respect to the highest recorded value of all data for each engine. It is immediately noted how these points adopt the form of a polynomial function with respect to these two independent variables. Engine speed has no impact on the values of Pmax, nevertheless it is important to mention that η_{intake} used for the calculation of NL already indirectly takes into consideration the effects of engine speed. In fact, volumetric efficiency depends on the intake air dynamic effects which are highly dependent on engine speed. Pmax values have been normalized for confidentiality reasons. Figure 4.6 also shows how Dataset PQ does not contain SA sweeps while Dataset WI and Dataset EGR do. This is the reason why these two last datasets cover a wider range in the MFB50 axis. After analysing the data from Figure 4.6, a quadratic dependence with MFB50 and a linear dependence with NL was observed and a polynomial equation (poly21) was used to describe Pmax. It is called in the following as Simple model, and it is defined by Equation (4.1).

$$Pmax = p_{00} + p_{10}MFB50 + p_{01}NL + p_{20}MFB50^2 + p_{11}MFB50 \cdot NL \qquad (4.1)$$
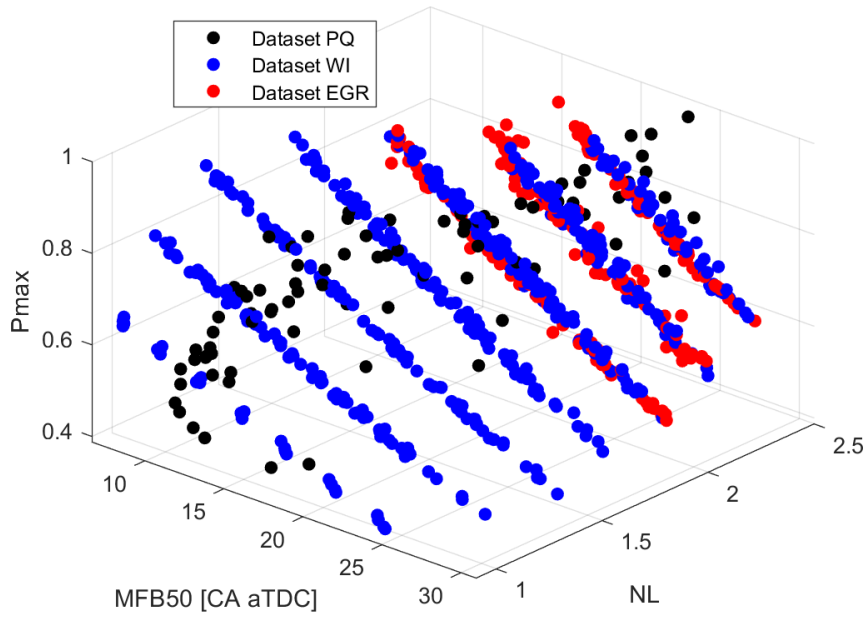
Figure 4.6 - Pmax from all experimental mean data as a function of MFB50 and NL for engine 1. Pmax values have been normalized with respect to the maximum Pmax value for this engine.

4.2.1.1   Mean data calibration and validation of engine points without EGR or WI

Given that data presented in Figure 4.6 contain points with and without EGR and WI, a first approach was to first calibrate and validate the model using only data that did not include them, given that Equation (4.1) does not take them explicitly into account. Dataset WI and Dataset EGR contain points without EGR or WI because on every EGR and *r* sweep from these campaigns there is an initial SA sweep with EGR or r equal to zero. Figure 4.7 shows the remaining points after removing those with EGR or WI and the surface that arises from the calibration using all remaining points. To calibrate the surface, the coefficients of Equation (4.1) were calculated using the least squares method.
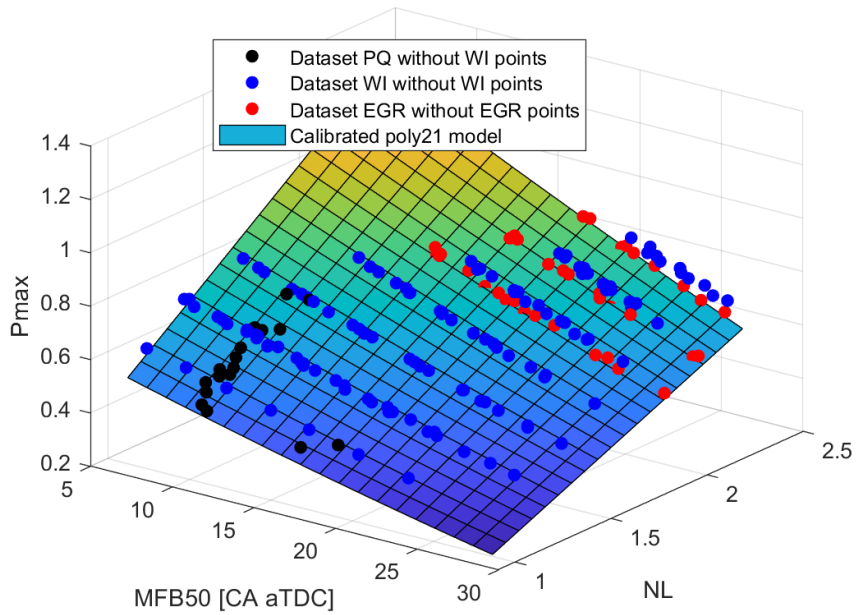
Figure 4.7 - Pmax from experimental data, without EGR or WI, as a function of MFB50 and NL. Calibrated polynomial with all the displayed points.

Figure 4.8 shows the results of the validation of all explored engine points without EGR or WI. Pmax error is expressed as a percentage of the experimental value and is calculated as shown in (4.2):

$$Pmax\ Error\ = 100 \times \frac{Pmax_{experimental} - Pmax_{model}}{Pmax_{experimental}} \tag{4.2}$$

A precision target of ± 5% when estimating Pmax has been imposed. As seen in Figure 4.8, most validation points were able to achieve this target. A few points from Dataset EGR with an MFB50 between 20 and 30 CA aTDC show an error slightly superior to the desired value. The reason for this is that a retarded combustion has higher cycle-by-cycle variations which lead to a mean measurement that is not as robust as those corresponding to a more anticipated combustion phase. This validation has a total RMSE of 2.1%. The points used for the validation are those shown in Figure 4.7.
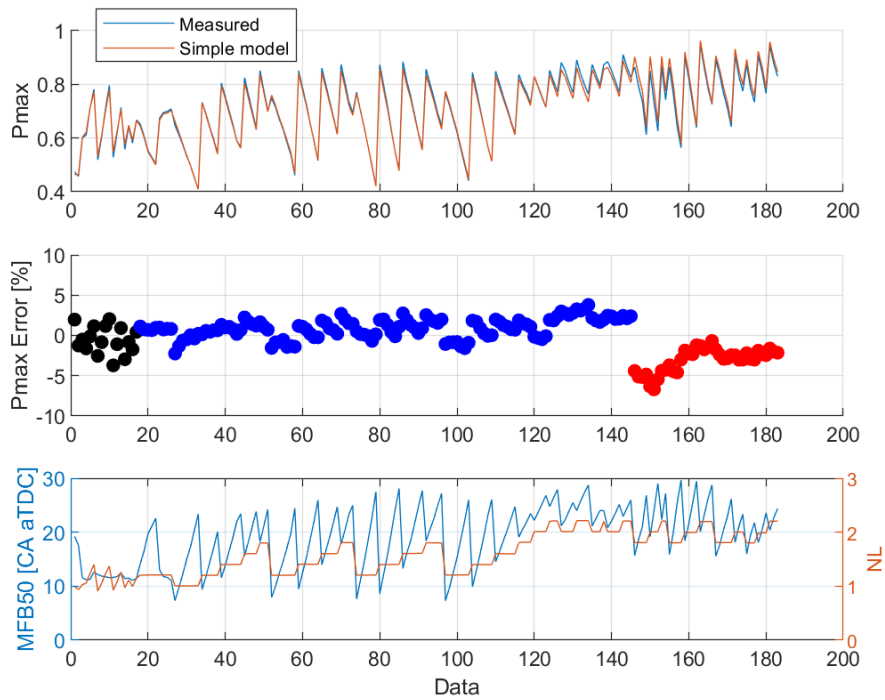
Figure 4.8 - Validation results of engine points without EGR or WI, using the calibrated model of Figure 4.7. Mean RMSE = 2.1%. Black, blue and red dots in the second plot represent Dataset PQ, WI and EGR, respectively.

4.2.1.2   *Mean data validation of engine points with EGR and WI*

The experimental points from Figure 4.6 suggest a unique Pmax surface when plotted with respect to MFB50 and NL, meaning that the polynomial model might not require additional compensations to accurately estimate Pmax on engine points that use EGR or WI. For this reason, to further test the validity of the model, the calibrated surface from Figure 4.7 is now used to validate the engine points with EGR and WI that have been excluded from the calibration and validation of the previous section.

Figure 4.9 shows the location of the experimental engine points in which EGR and WI were used and the calibrated model from Figure 4.7 as a reference. Figure 4.10 contains the validation results when estimating Pmax with the previously calibrated polynomial and it can be seen how most of the validated engine points comply with the self-imposed precision target of ± 5%. This result demonstrates that the model can predict Pmax in points where EGR and WI were used, without the need of adding these as additional inputs, retaining only MFB50 and NL as inputs. This validation has a RMSE of 2.3%. In this case, none of the validated points were used for calibration.
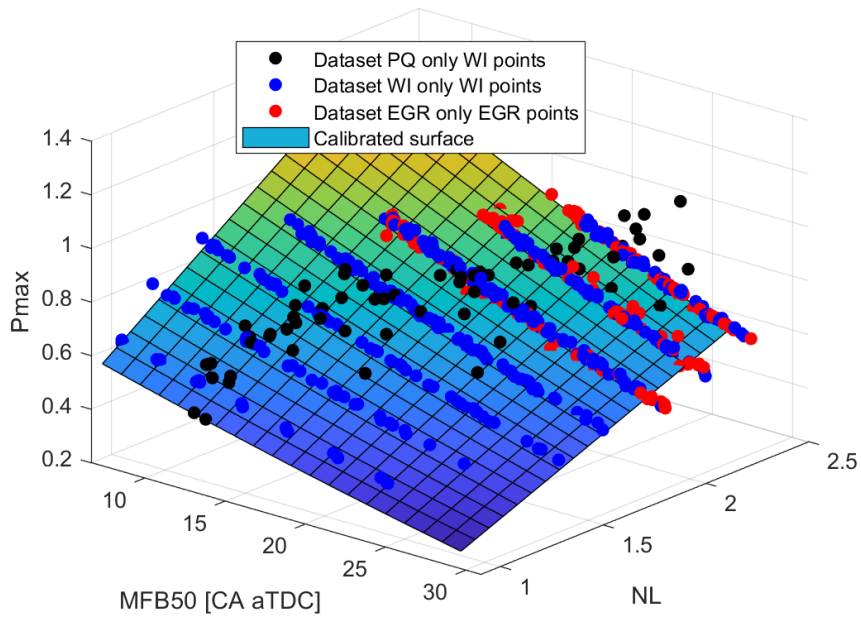
Figure 4.9 - Pmax from experimental data with EGR or WI only, and model showed in Figure 4.7.
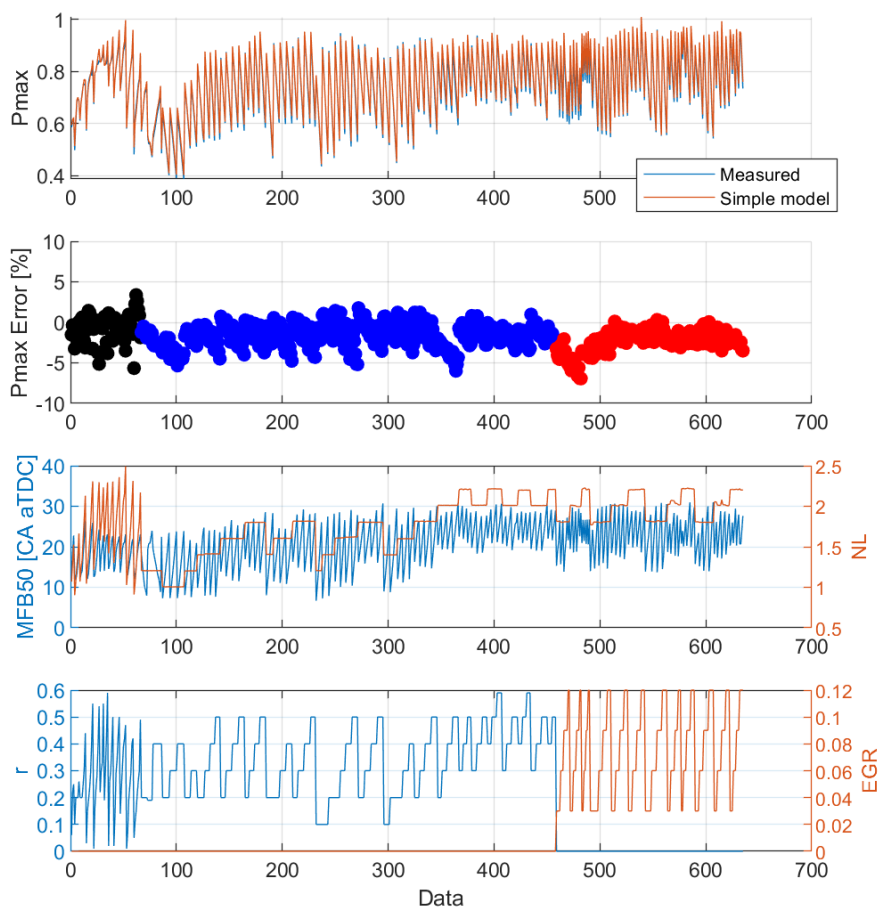
Figure 4.10 - Validation results of engine points with EGR or WI, using the calibrated model of Figure 4.7.Mean RMSE = 2.3%.

The main reason why it is not necessary to add WI or EGR variables as inputs to the model is because, as already stated by the author in a previous publication [37], the main effect of EGR and WI is to slow down combustion speed and this effect is already contained in the MFB50.

4.2.1.3   Cycle-by-cycle data validation

To further expand the validation of the previously described model, a series of mid to high load engine points at 3000 rpm have been explored and the cycle-by-cycle data has been validated using the same surface from the previous sections (calibrated with mean data). As shown in Figure 4.11, the cycle-by-cycle data consists of SA sweeps for three different cases of NL.
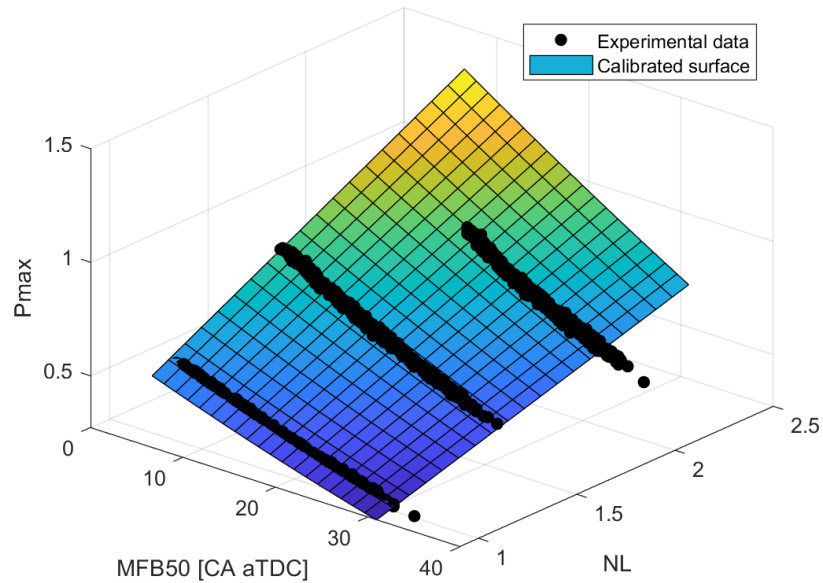
Figure 4.11 - Cycle-by-cycle experimental data to be validated using calibrated surface from Figure 4.7.

Figure 4.12 shows the results of the validation of the cycle-by-cycle data. In this case, the mean RMSE of the entire validation was of 3.6%, evidencing a slight decrease of the performance of the model with respect to that obtained during the validation of the mean data, but still within the 5% limit. The validation of these data points is crucial to implement the model in a control strategy that would most likely need Pmax values to be estimated cycle-by-cycle.
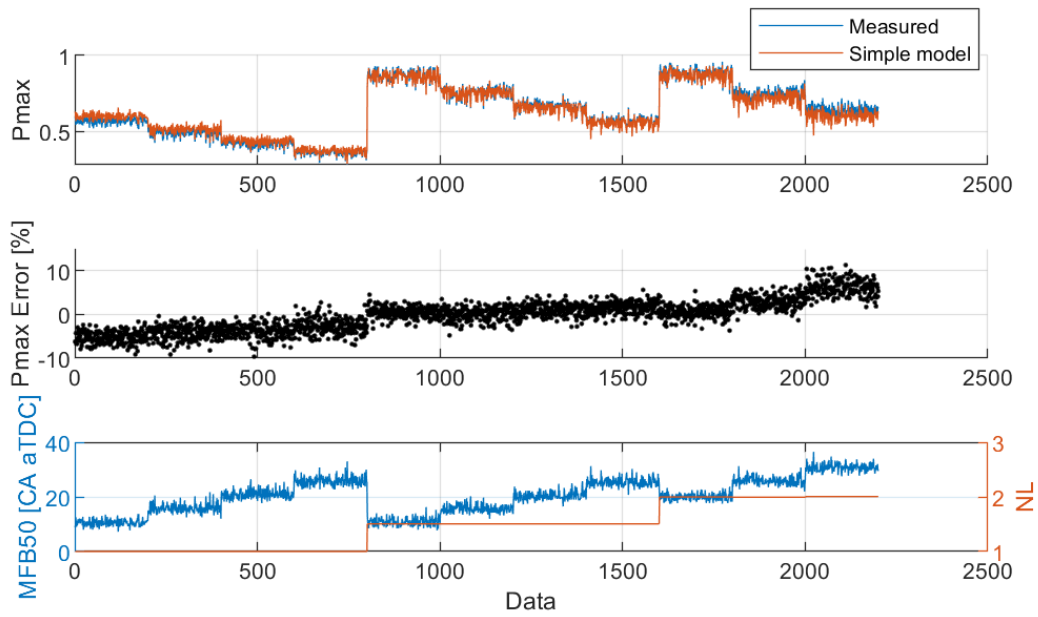
Figure 4.12 - Validation results of cycle-by-cycle data, using the calibrated surface of Figure 4.7. Mean RMSE = 3.6%.

4.2.1.4 Lean operating conditions model validation

As mentioned before, the fourth experimental campaign carried out on engine 1 contains lambda sweeps ranging from 1 to 1.3 for six different cases of MFB50 and NL. The aim of this campaign was to determine whether the model in its Simple form could be applied in lean conditions or if λ needed to be included as an additional input. Figure 4.13 shows the Pmax as a function of lambda for the engine points explored in the last experimental campaign of this engine, and a quasi-linear trend with respect to Air-to-Fuel ratio is observed for each engine point.
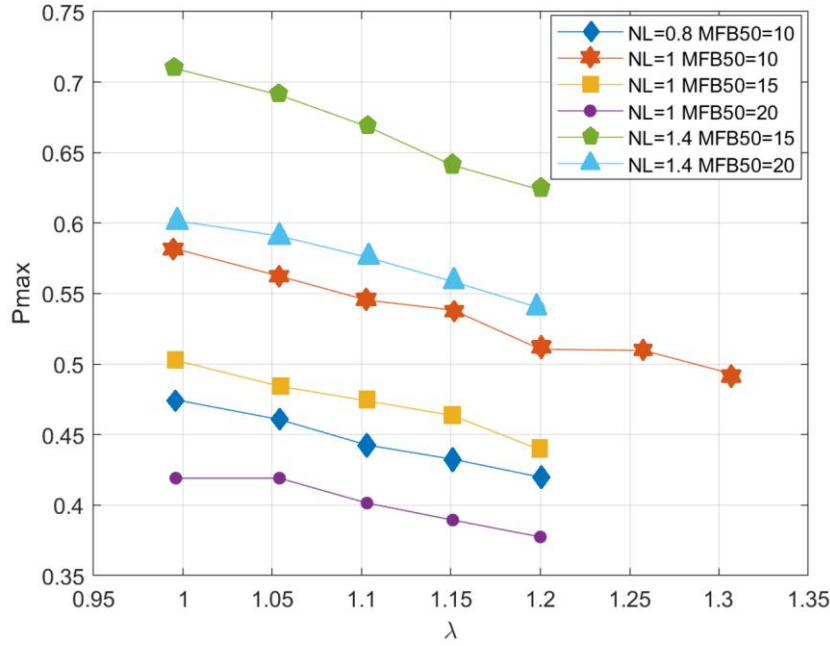
Figure 4.13 – Normalized Pmax as a function of lambda for the six different cases, at 3000rpm, of NL and MFB50 explored in the fourth experimental campaign.

Figure 4.14 shows the results of the validation with such mean data points of the fourth experimental campaign. The model defined by Equation (4.1) has been recalibrated by using the points from Figure 4.7 and adding those of the fourth experimental campaign. As Figure 4.14 shows, the Simple Model is unable to reach acceptable performance during these lambda variations (RMSE = 11.6%). This leads to the need to add an additional corrective function that includes lambda as an input, as shown in Equation (4.3). From now on, any Pmax model that includes corrective functions for additional parameters will be named Complex Model. A linear function was used for the correction of Pmax since the observed trend of decreasing maximum in-cylinder pressure with increasing lambda was linear.

$$Pmax = [p_{00} + p_{10}MFB50 + p_{01}NL + p_{20}MFB50^2 + p_{11}MFB50 \cdot NL] \times [a_1 + a_2\lambda] \quad (4.3)$$

In which a_1 and a_2 are the calibration coefficients. The blue line and dots in Figure 4.14 represent the performance of the Complex Model defined by Equation (4.3). For this, the model has been recalibrated using the same points shown in Figure 4.7 and also adding those of the fourth experimental campaign. Results have greatly improved (RMSE = 2.5%) and are now comparable to that obtained in the previous sections.
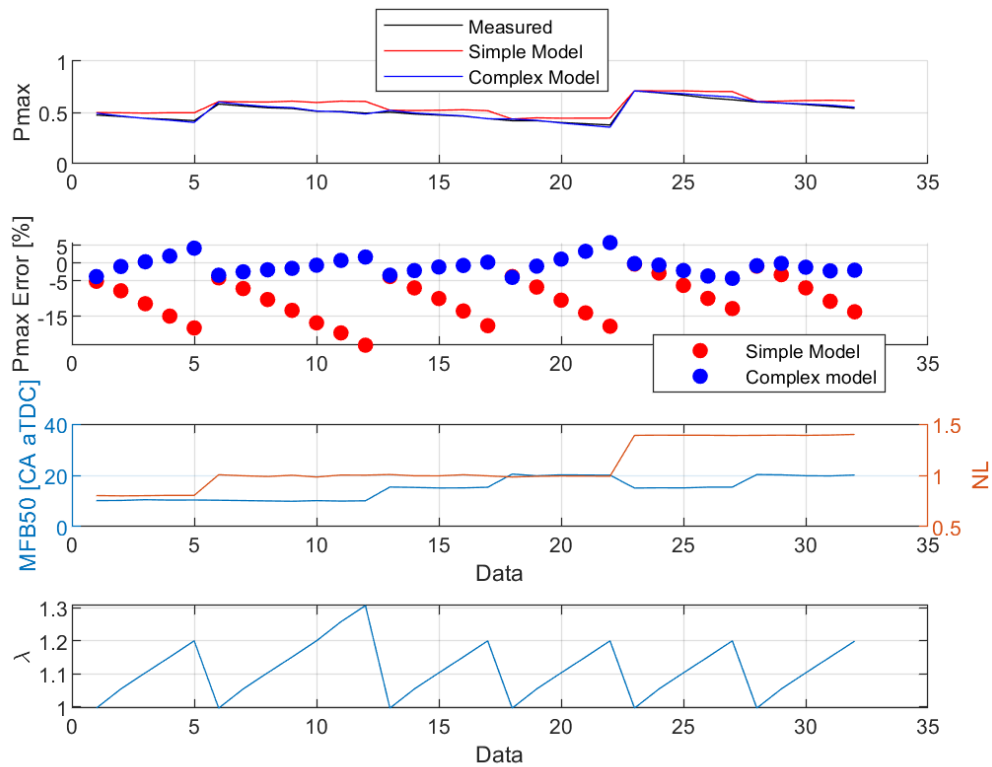
Figure 4.14 - Validation results of mean data from the fourth experimental campaign, using the Simple Model (RMSE = 11.6%) and the Complex Model (RMSE = 2.5%).

The cycle-by-cycle data from this campaign has also been used for model validation. Figure 4.15 shows the improvement of the Complex model (RMSE = 3.3%) when compared to the Simple Model (RMSE = 13.8%). The data points between 4000-4500 have a high error due to the retarded combustion and high lambda value, leading to higher combustion variability than the rest of the engine points and thus making it more difficult for the model to predict these variations.
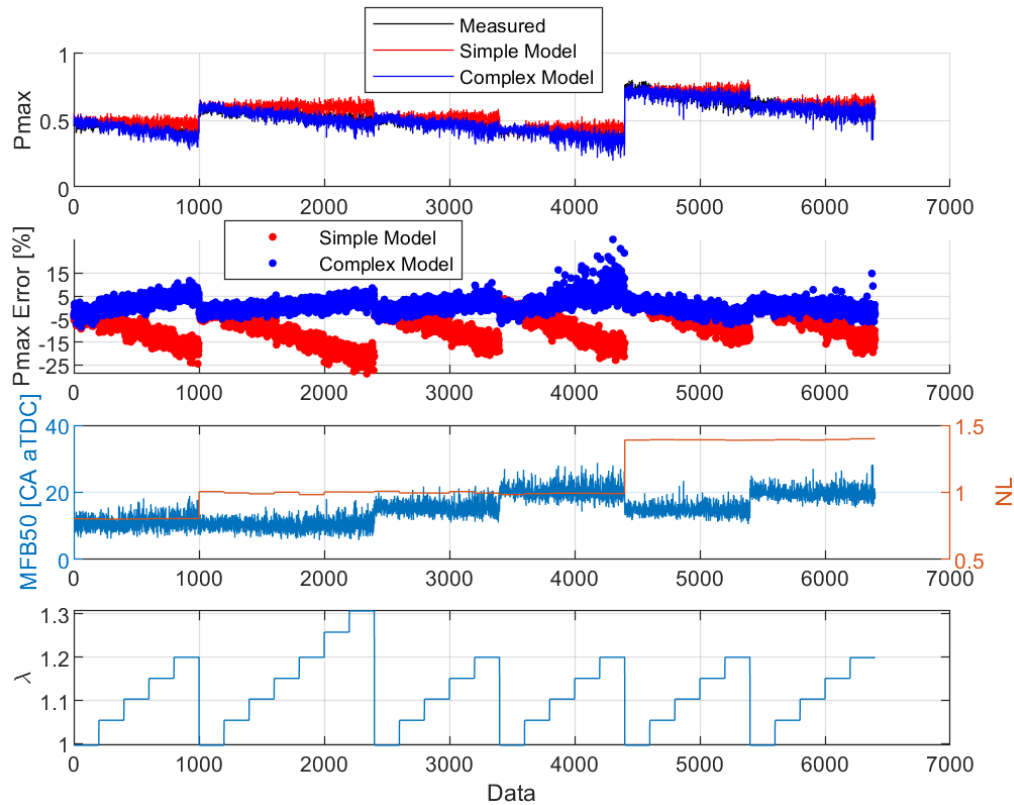
Figure 4.15 - Validation results of the cycle-by-cycle data from the fourth experimental campaign, using the Simple Model (RMSE = 13.8%) and the Complex Model (RMSE = 3.3%).

4.2.1.5   *Identification of the minimum number of engine points needed for model calibration*

Until now, a vast number of engine points, around 180, were used for the calibration of the model, but this does not mean that such amount is necessary to obtain desired validation results. In the previous sections, at first all experimental points without EGR or WI were used to calibrate the model and validated in those same points, and later that same calibration was used to validate the experimental data with EGR and WI. In this section, an assessment is done to identify the minimum amount of experimental data needed to obtain best model performance during validation. For this, an identification methodology was developed to properly select and increasing number of experimental points from all those available, including those in which EGR and WI were used. The methodology chooses points to cover first the region close to the border of the MFB50-NL domain shown in Figure 4.6, and then it also selects some central points. The number of points used for calibration starts at a minimum of six, being this the minimum amount of data needed to obtain the six coefficients of the Simple Model. At each iteration step the method uses the chosen points to calibrate the model and then utilizes such calibration to validate all the available experimental data while calculating the R2 and RMSE of each calibration and validation. The data from the fourth experimental campaign has been left out from this analysis.

Figure 4.16 shows the trend in R2 and RMSE for this process, when considering up to 50 calibration engine points (as already mentioned, the validation is always carried out using all the remaining points, and R2 and RMSE indexes are used to quantify the accuracy of the model during the validation process). When considering the R2, the minimum number of points needed to obtain the best performance is 14, and the maximum R2 obtained is of 0.99. Adding more calibration points does not improve the R2 value. As regards RMSE, the minimum number of points needed for best performance is 20, and the minimum RMSE obtained is of 2%. Having said this, to achieve best results in terms of both R2 and RMSE, a total of 20 engine calibration points would allow achieving the highest accuracy.
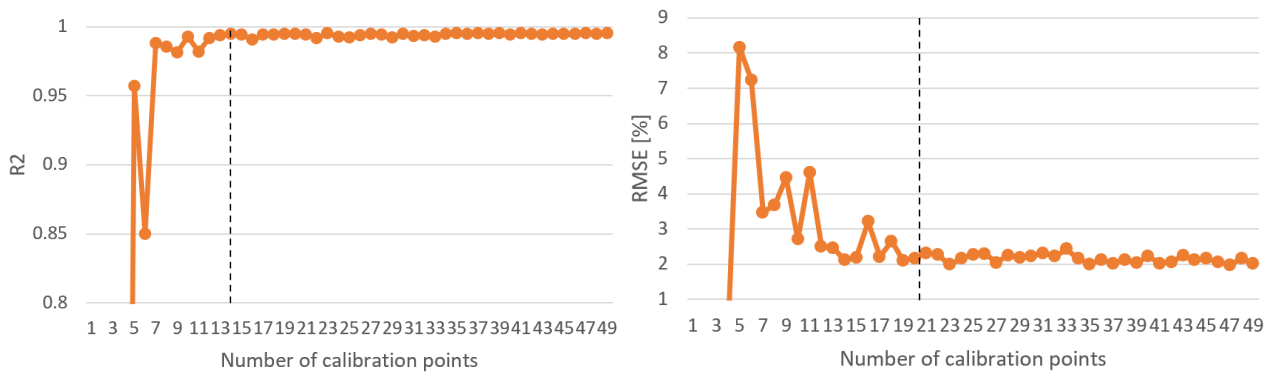
Figure 4.16 - Validation R2 and RMSE as a function of number of points used for calibration. Minimum number of points for best performance is 20.

As mentioned before, the method used for the analysis of the experimental data needed for calibration selects a small number of points that first cover the perimeter of the region delimited by all available experimental data, and then adds proper intermediate points inside this perimeter. Figure 4.17 shows an example of this selection for the case of 20 calibration points. Choosing points close to the perimeter allows to better shape the surface, not having the need to extrapolate the shape of the surface during validation. Furthermore, internal points give the correct slope to the surface in both directions (MFB50 and NL).
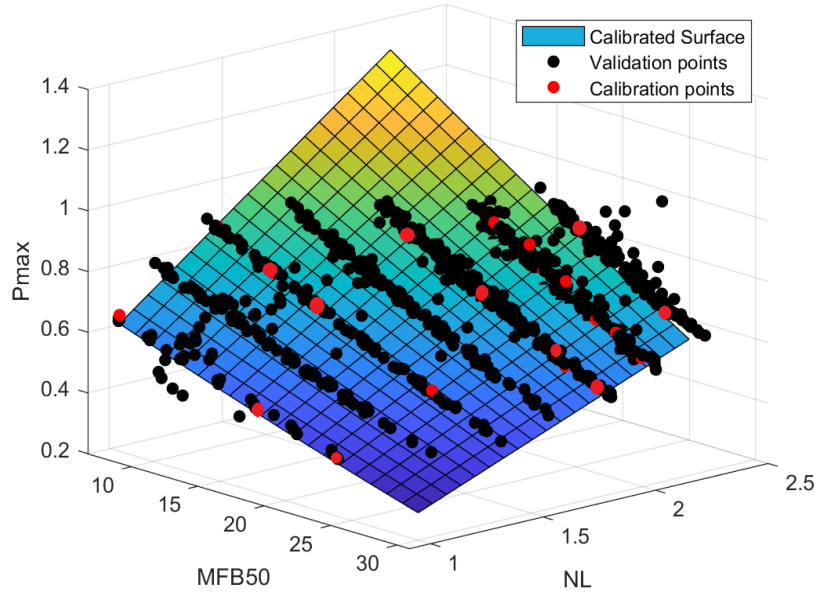
Figure 4.17 - Example of a selection of 20 engine points that are enough for an accurate calibration of model coefficients.

4.2.1.6 Addition of corrective functions for EGR and WI

In previous sections, it has been demonstrated that the desired model performance of $\pm$ 5% error on Pmax estimation could be achieved without any compensation for EGR and WI. Nevertheless, it has been observed that validation results are slightly dependent on EGR and *r* ratios. Figure 4.18 shows a portion of the data with EGR and WI that has been validated in the previous sections without using any corrective functions (Simple Model). This figure shows how the Pmax error exhibits a slight slope for each case of EGR or *r*. This mentioned effect can be compensated by adding two linear corrective functions considering EGR and WI effects. Equation (4.4) gives a mathematical formulation of Complex Model with these corrective contributions.

$$Pmax = (p_{00} + p_{10}MFB50 + p_{01}NL + p_{20}MFB50^2 + p_{11}MFB50 \cdot NL) \times (a_1 \qquad (4.4)$$
$$+ a_2 r) \times (b_1 + b_2 EGR)$$

Figure 4.18 compares results obtained from both the Complex Model and Simple Model. The corrective functions have contributed to lower the previously mentioned slope. Nevertheless, improvements have occurred mostly on points with WI and not on those with EGR, and RMSE has only decreased from 2% without the complex model to 1.8% with the complex model. Given this marginal improvement, it can be concluded that in the case of engine 1 the use of corrective functions is not necessary.
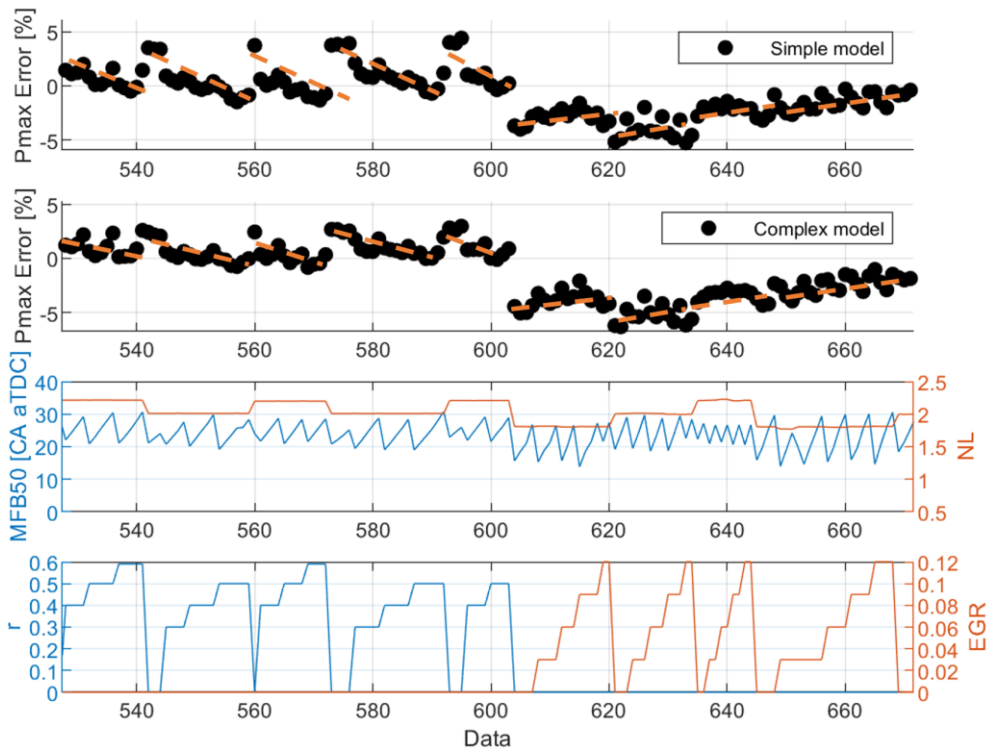
Figure 4.18 - Validation of points with EGR and WI, using a calibration with (Equation 3) and without (Equation 6) corrective functions. Mean RMSE improved from 2% with the Simple Model to 1.8% with the Complex Model.

4.2.2 Engine 2 and Engine 3: Simple Model calibration and validation

As shown in previous sections, the Simple Model is capable of predicting Pmax with the ± 5% desired precision. To test the model on engines 2 and 3, the same approach has been used to analyse data from engine 2 (0.9l Turbo GDI) and engine 3 (1.0L NA). The values of Pmax have been normalized with respect to the maximum registered value on each engine for confidentiality reasons, as it has been done for Engine 1.

Figure 4.19 shows the data available for these engines in terms of RPM and NL. Mid and high loads have been explored on engine 2 while the entire operating range of engine 3 has been tested. In both cases, no sweeps were conducted and each point corresponds to standard calibration. Figure 4.20 shows the Pmax trend with respect to MFB50 and NL for each engine, and it is noted how it may be fitted with a relatively smooth surface, just as in the case of Engine 1. Individual surfaces were calibrated for each of these two engines, as shown in Figure 4.21 (for engine 2) and Figure 4.23 (for engine 3), and then used during the validation of each of these, as shown in Figure 4.22 (for engine 2) and Figure 4.24 (for engine 3).
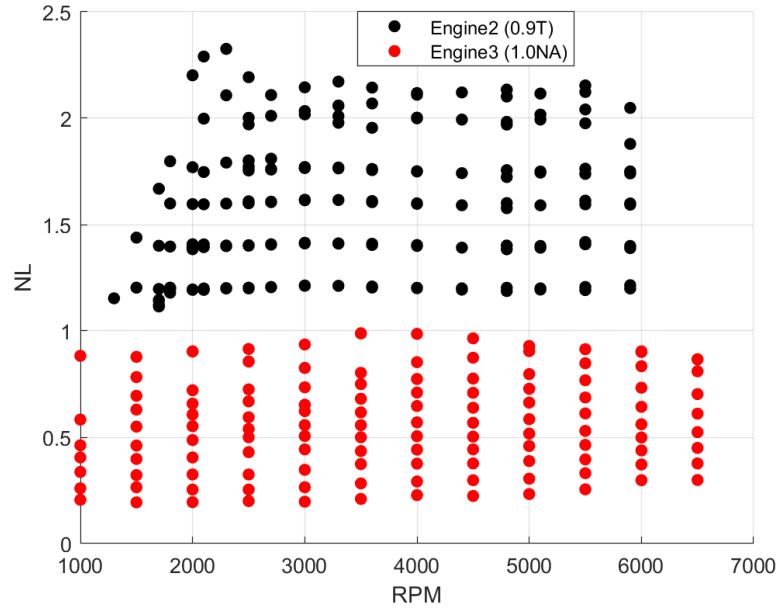
Figure 4.19 - Explored engine points on the experimental campaigns of engines 2 and 3.
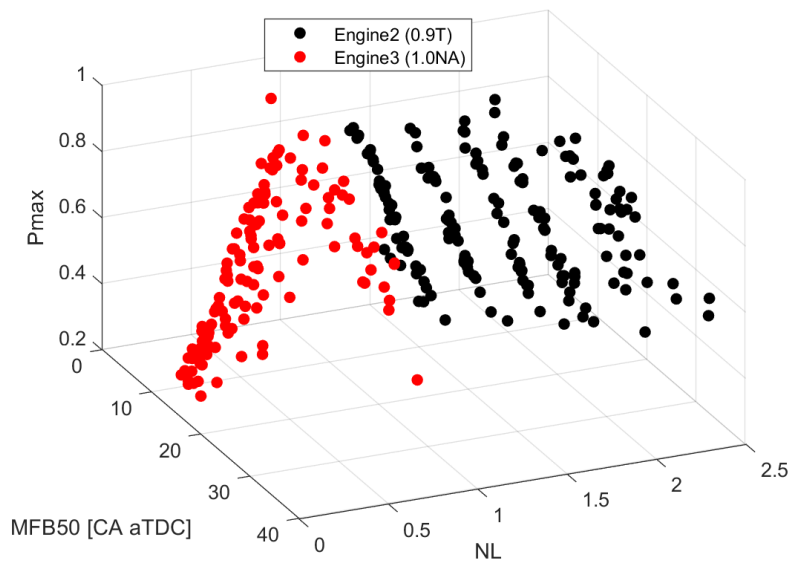
Figure 4.20 - Pmax from all experimental mean data as a function of MFB50 and NL for engines 2 and 3. Pmax values have been normalized with respect to the maximum Pmax value for each engine.

As mentioned before, first the Simple Model is used to calibrate the surface for engine 2 using all available engine points, as presented in Figure 4.21, and the subsequent validation of also all available points is displayed in Figure 4.22. A mean RMSE equal to 1.9% is achieved when validating the data from engine 2, complying with the established precision limit of 5%.
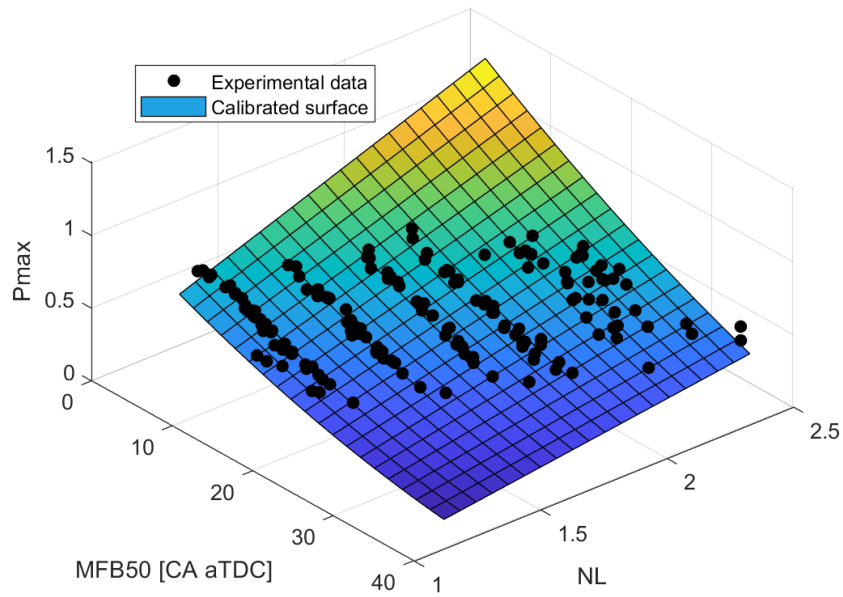
Figure 4.21 - All available experimental data for engine 2 and the surface that arises from the calibration of the Simple Model with this data.
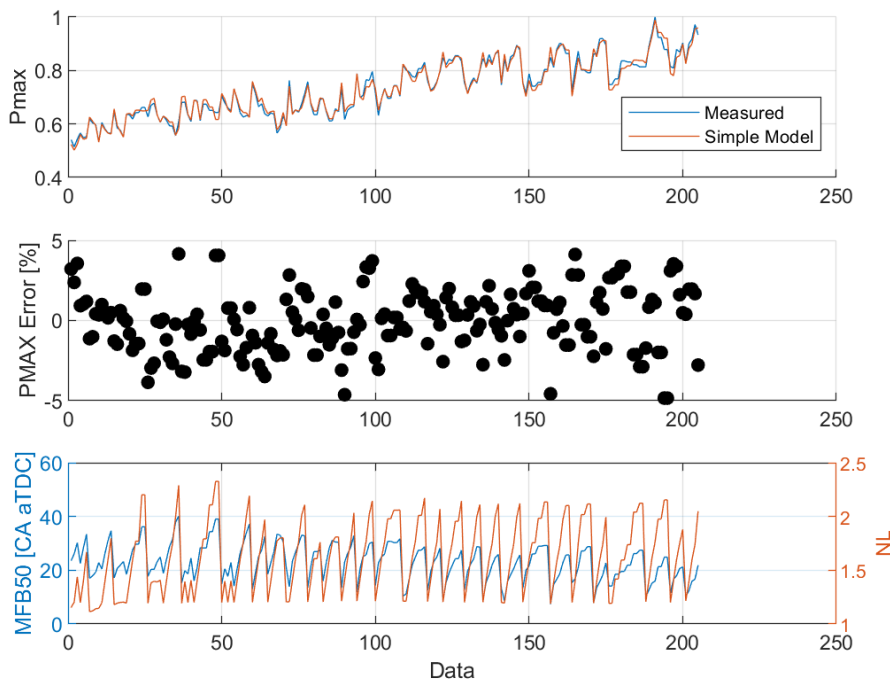
Figure 4.22 - Validation of data from engine 2, using a calibration with the Simple Model with data from only this engine. Mean RMSE = 1.9%.

The same procedure is repeated for engine 3, using the Simple Model to calibrate the surface with all available data from this engine and then validating on these same points. Figure 4.23 and Figure 4.24 show the surface that arises from the data of engine 3 and the validation results of these points using the calibrated surface, respectively. It is noted that Pmax error is higher than in the case of engine 2. This is given by the fact that engine 3 is naturally aspirated and the Pmax values are almost half when compared to engine 2 which is turbocharged, making the Pmax error almost double as a percentage. The mean RMSE results equal to 4.8%, meaning that the model is still able to achieve the desired precision.
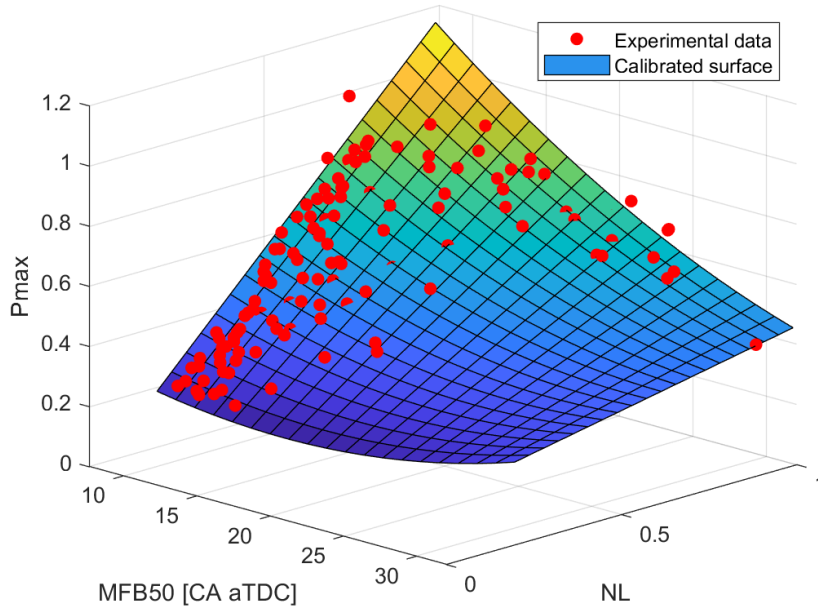
Figure 4.23 - All available experimental data for engine 3 and the surface that arises from the calibration of the Simple Model with this data.
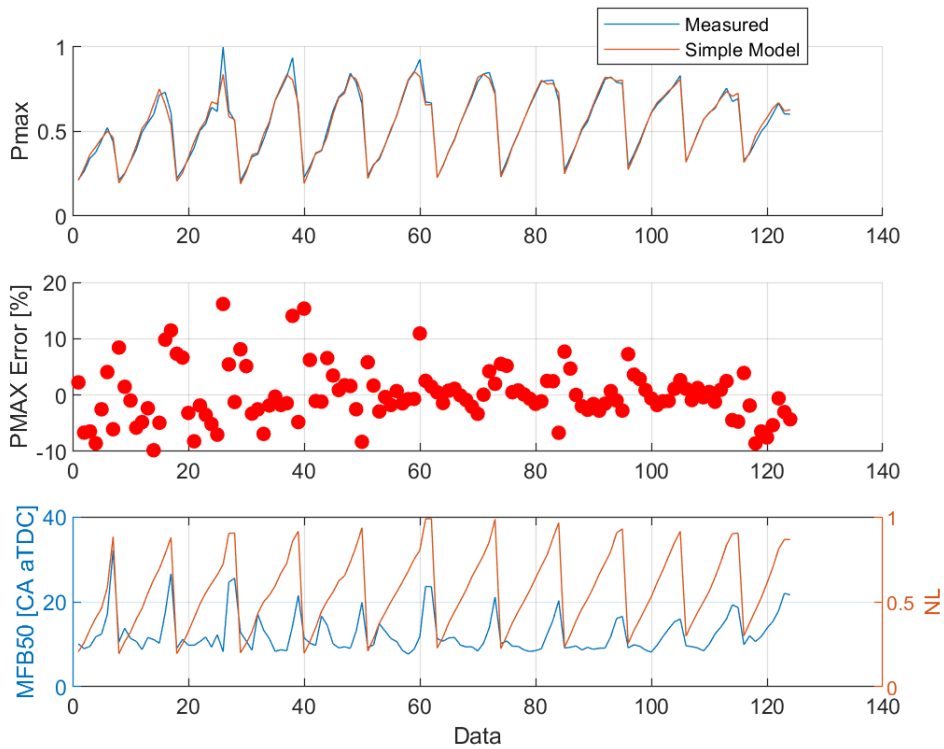
Figure 4.24 - Validation of data from engine 3, using a calibration with the Simple Model with data from only this engine. Mean RMSE = 4.8%.

As done for engine 1, an analysis on the minimum amount of engine points needed for a successful calibration and validation is carried out and as exposed in Figure 4.25, and also in this case the minimum number of points needed for best performance is around 20. The methodology used for choosing these points is the same as the one described for engine 1.
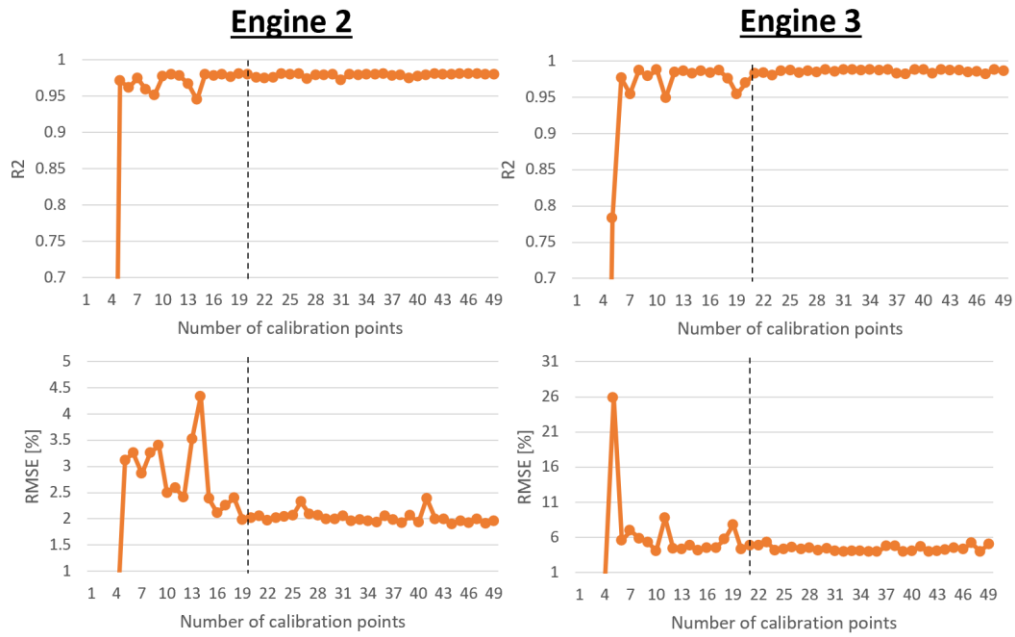
Figure 4.25 - Validation R2 and mean RMSE as a function of number of points used for calibration for engines 2 and 3. Minimum number of points for best performance is 20.

4.2.3 Sensitivity analysis of input variables and coefficients of the model

As established, the main inputs of the model are NL and MFB50, which should be somehow measured in the case of a real-time control strategy application. NL can be easily determined from the measurement of intake pressure and a properly calibrated volumetric efficiency coefficient, as shown in Equation (4.1), and from experience it can be measured with an accuracy of ±4%. In the case of MFB50, the author has developed and demonstrated a way of measuring MFB50 from the signal of the accelerometers already used on OEM applications for knock detection [36]. In this case the accuracy observed was of ±0.7 CA aTDC for most engine points. Having said this, a sensitivity analysis is made on these two variables, to assess the Pmax error due to errors and uncertainties on NL and MFB50 measurements.

$$\frac{\partial Pmax}{\partial MFB50} = p_{10} + 2 \times p_{20}MFB50 + p_{11}NL \tag{4.5}$$

$$\frac{\partial Pmax}{\partial NL} = p_{01} + p_{11}MFB50 \tag{4.6}$$

Being a surface, the sensitivity of Pmax is not a unique value but changes depending on the MFB50 and NL being considered. Equation (4.5) shows the calculation of sensitivity to MFB50 while Equation (4.6) is relative to the sensitivity to NL. Table 4.2 shows the sensitivity of Pmax (expressed as a percentage of the maximum registered Pmax value in the engine, the same used for the normalization) for both input variables on engine 1 as an example (the other two engines exhibited a very similar behaviour). The table on the left shows the sensitivity of the model to MFB50, calculated on the engine points reported on the table and then

103

considering a MFB50 measuring accuracy of ±0.7 CA aTDC. Same is done on the table on the right, being this the sensitivity to NL, in which the considered measuring accuracy of NL is of ±4%. It can be seen how with the mentioned measuring accuracy of both MFB50 and NL, the sensitivity of Pmax to both input variables remains in most cases below 5%.

Table 4.2 - Sensitivity of Pmax (expressed as a percentage of the maximum registered Pmax value in the engine, same used for the normalization) to MFB50 and NL for engine 1.

Sensitivity to MFB50 [% Pmax]								Sensitivity to NL [% Pmax]						
		Load [NL]								Load [NL]				
		0.3	0.6	1	1.5	2	2.5			0.3	0.6	1	1.5	2	2.5
MFB50 [CA aTDC]	10			1.7%	2.2%	2.8%	3.3%	MFB50 [CA aTDC]	10			5.4%	5.4%	5.4%	5.4%
	20			1.5%	2.0%	2.6%	3.1%		20			4.3%	4.3%	4.3%	4.3%
	30			1.3%	1.8%	2.4%	2.9%		30			3.2%	3.2%	3.2%	3.2%

To understand how much each term of the model contributes to the final result, Table 4.3 shows the values that they assume when considering an MFB50=15CA aTDC and NL=1 as an example, for all three engines. This engine point corresponds to a mid-load situation for engines 1 and 2 and high load for engine 3. It is noted how, at this engine point, the most relevant terms are those containing NL, but this is not necessarily true when considering other engine points. As observed from the slope of the surfaces shown in the previous sections, the terms with NL become more relevant at low values of MFB50, and terms with MFB50 become more relevant at high values of NL.

Table 4.3 - Values adopted by each term of the model for a situation of MFB50=15CA aTDC and NL=1.

	p_{00}	$p_{10}MFB50$	$p_{01}NL$	$p_{20}MFB50^2$	$p_{11}MFB50 \cdot NL$	Pmax
Engine 1	0.15	-0.12	0.64	0.02	-0.16	0.53
Engine 2	0.05	-0.15	0.87	0.08	-0.26	0.59
Engine 3	0.02	-0.14	1.52	0.10	-0.60	0.90

Figure 4.26 shows the Pmax surface of all three engines on a single plot, showing that these tend to overlap between each other. Nevertheless, a unique surface cannot predict Pmax on all engines with the desired accuracy because of the constructive characteristics of each engine, especially in terms of the MFB50 and NL borders. For this reason, it is imperative to carry out at least a small experimental campaign, as shown in Figure 4.17, to calibrate the surface when considering an unknown engine.
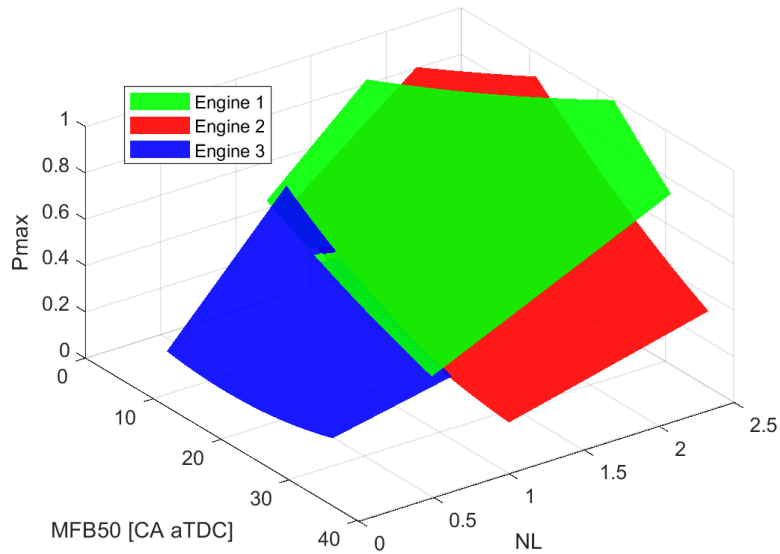
Figure 4.26 - Superposed Pmax surfaces of all three engines.

4.2.4 Engine 4: variation of the Complex Model and validation of GCI engine

The validation results from the previous three engines confirmed the validity and robustness of the application of the Simple Model (or Complex Model when needed) on SI engines. In this section, data from a GCI engine were used to determine if the model remains valid when implementing it on a CI engine. As in the previous cases, Pmax values for this engine are normalized with respect to the highest registered value from the mean data of engine 4.

Figure 4.27 shows the experimental mean data available for this engine. It is easy to note the differences from the tests carried out for the previously analysed engines. As well known, CI combustion differs significantly when compared to SI combustion. Main control parameters such as Prail, injected quantity and intake pressure define the shape of combustion and consequentially Pmax.

For these reasons, to guarantee low combustion variation, the GCI engine was tested at 5 different loads at 2000 rpm. In each point, sweeps of MFB50, Prail and MAP have been performed. Many works in literature show that to guarantee a low GCI combustion variability, it is mandatory to select proper control parameters generating thermodynamics conditions able to achieve the auto-ignition of the gasoline. By the analysis of this data in terms of Coefficient of Variation of IMEP (CoV(IMEP)), we could distinguish stable engine operating points from unstable ones, in which any other considerations loose significance in terms of Pmax estimation.
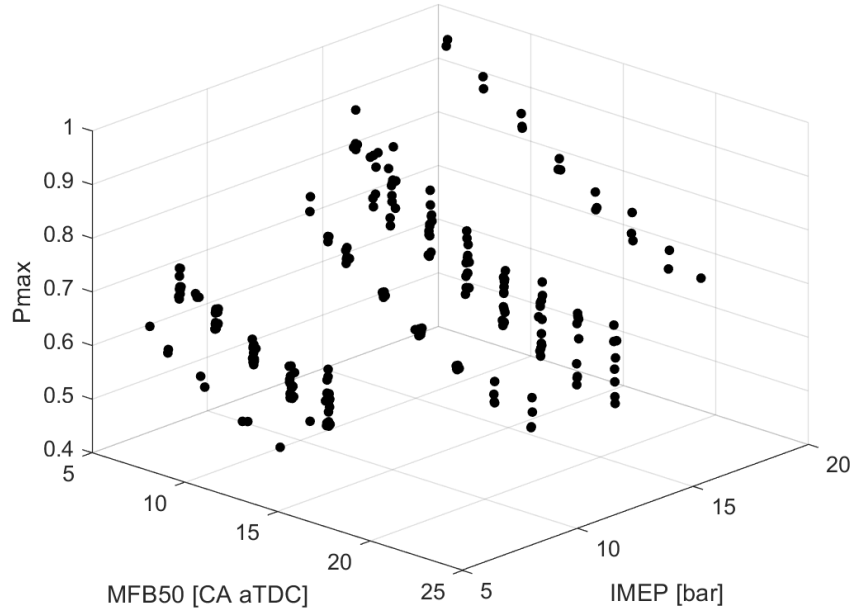
Figure 4.27 - Pmax from all experimental mean data as a function of MFB50 and NL for engine 4. Pmax values have been normalized with respect to the maximum Pmax value for each engine.

4.2.4.1 Complex Model variation and mean data validation

Because of the beforementioned varying parameters, the application of the Simple Model, as shown in Figure 4.28, results in a mean data validation RMSE = 5.2%, slightly over the imposed precision limit. This leads to the implementation of a Complex Model, but now with corrective functions that depend on either Prail, lambda or MAP. Equation (4.7) shows a form of Complex Model in which all three of these parameters are included formulas inputs. The validation results obtained when using such form of Complex Model are also displayed in Figure 4.28, showing a reduction in the Pmax error that allows obtaining a mean validation RMSE = 3%.

$$Pmax = (p_{00} + p_{10}MFB50 + p_{01}NL + p_{20}MFB50^2 + p_{11}MFB50 \cdot NL) \times (a_1 \qquad (4.7)$$
$$+ a_2 Prail) \times (b_1 + b_2\lambda) \times (c_1 + c_2 MAP)$$
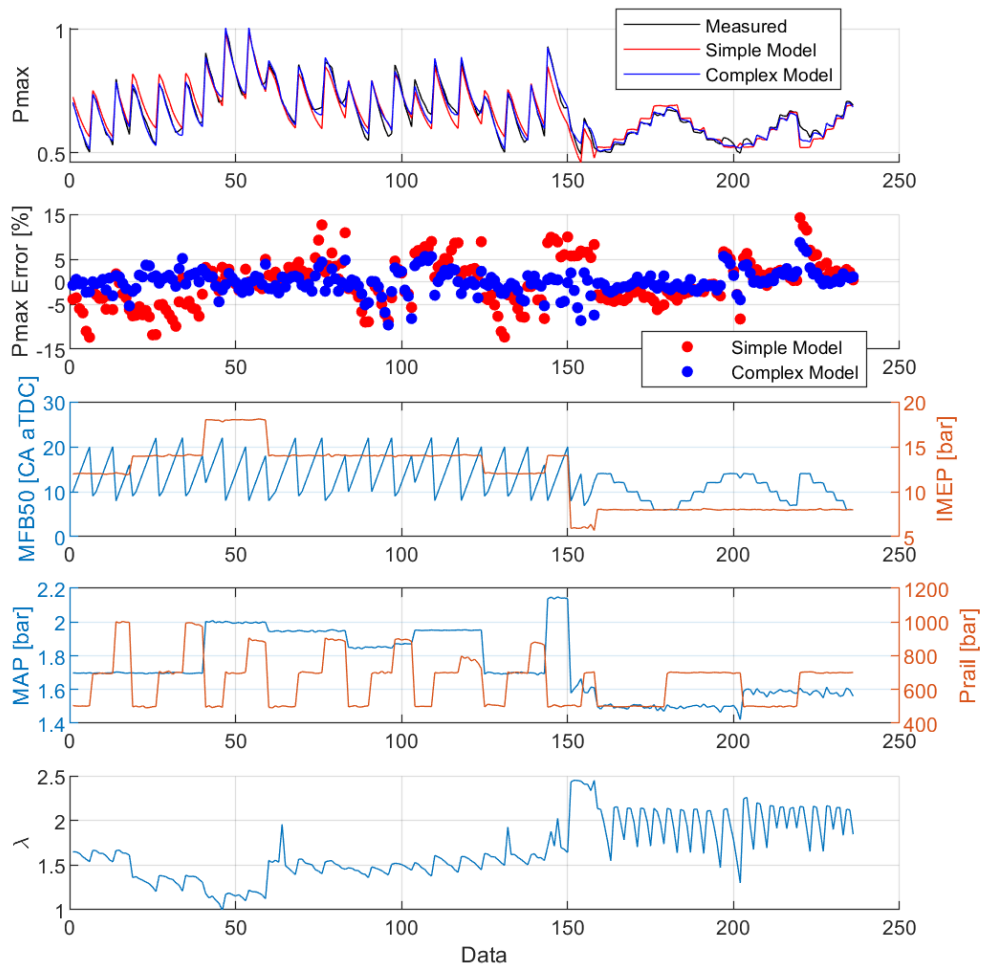
Figure 4.28 - Validation results of mean data of engine 4, using the Simple Model (RMSE = 5.2%) from Equation (4.1) and the Complex Model (RMSE = 2.6%) from Equation (4.7).

The improvement of validation results with the usage of the Complex Model in Equation (4.7) does not mean that all three variables must be included in the equation. A study has been conducted in which the corrective functions from Equation (4.7) have been used one at a time for the calibration and validation of the model. The results of this analysis are shown in Figure 4.29, where it is noted that adding a corrective function for MAP is the choice that improves results the most in terms of RMSE (apart from using all three), being capable of decreasing mean RMSE from 5.2% with the Simple Model to 3% with the MAP corrective function only. The validation results obtained with only the MAP corrective function are also close to those obtained when applying all three corrective functions. Opposite to Engine1, when Lambda generates deviations in terms of Pmax estimation, for CI engines the load index is directly related to lambda if intake pressure and the engine speed are constant.
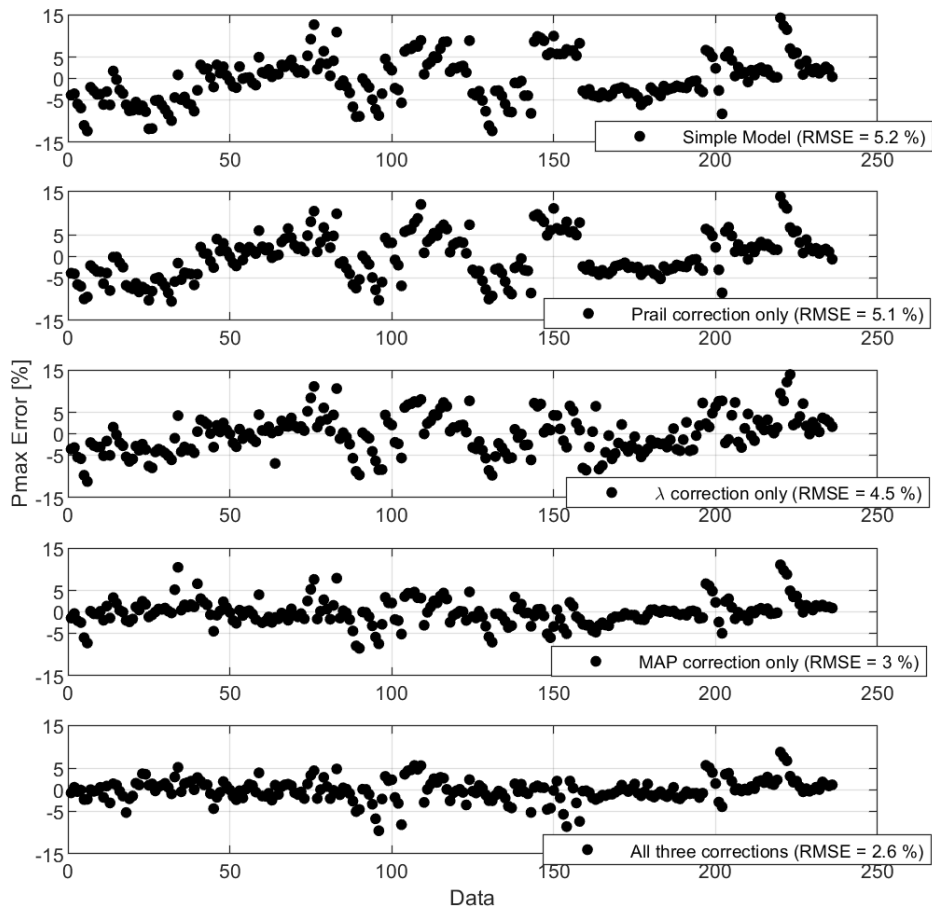
Figure 4.29 - Validation results of mean data of engine 4, using the Simple Model, three different variants of the Complex Model from Equation (4.7) and the complete Complex model from Equation (4.7).

Having already successfully validated the Pmax model over mean data for engine 4, the following step is to validate it over cycle-by-cycle data, for which the calibration from the Complex Model of Figure 4.28 (using Equation (4.7)) is used. Given the vast dimensions of such data, a selection of the most representative engine points has been done. Chosen points correspond to values of IMEP ranging from 12 bar up to 18 bar in which, as in the case of the mean data, parameters such as Prail, lambda and MAP still vary.

Figure 4.30 shows the validation of the aforementioned points, obtaining a mean RMSE = 5.2%, slightly over the imposed limit. The points of Figure 4.28 which exhibit the greatest error can be associated to the fact that, as mentioned before, the nature of the test from which this data come from includes situations in which GCI combustion was not stable. This can be observed for example in data points ranging from 1300 to 1800 in which IMEP is much less stable than data points ranging from 1 to 1300.
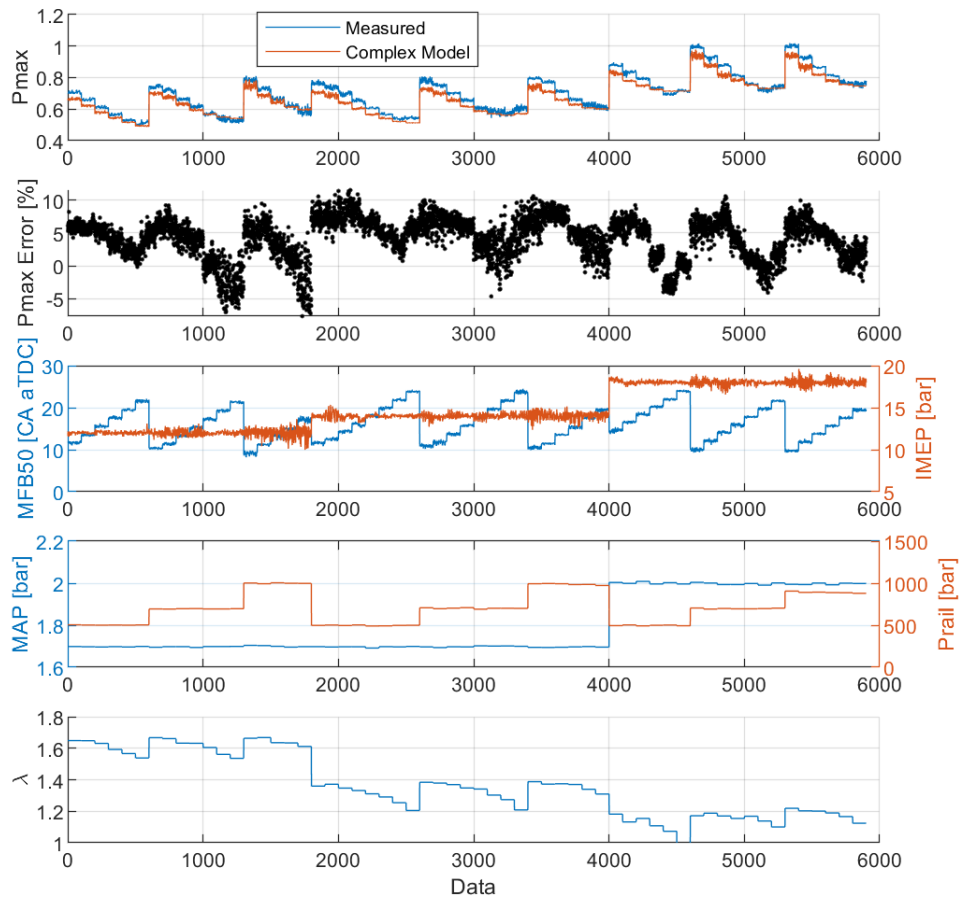
Figure 4.30 - Validation results of cycle-by-cycle data, using Equation (4.7). Mean RMSE = 5.2%.

During the previously shown validations of engine 4, all available engine points have been used for both calibration and validation, but as in the previous engines it is interesting to find the minimum amount of engine points needed for optimal validation results. This study has been carried out also for engine 4, considering the mean data available, and Figure 4.31 shows how as in the previous cases around 20 engine points are enough to obtain optimum results.
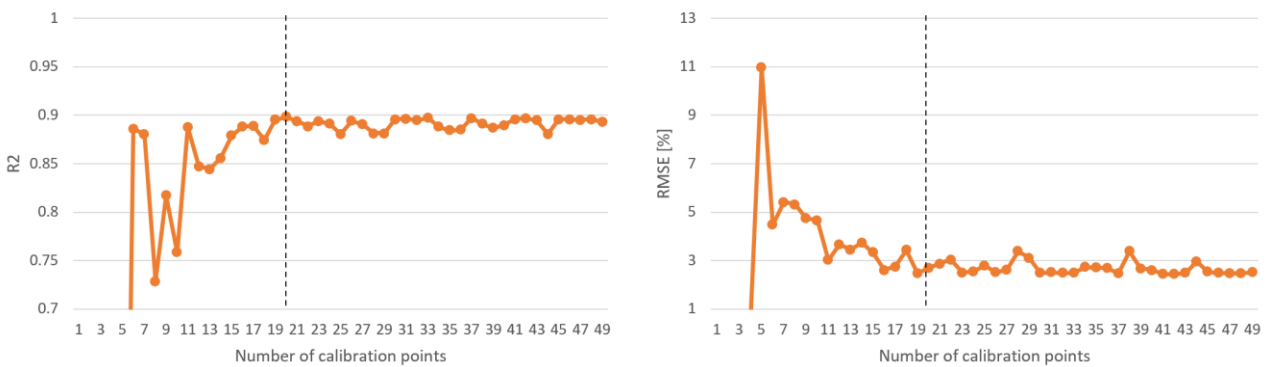
Figure 4.31 - Validation R2 and mean RMSE as a function of number of points used for calibration for engine 4. Minimum number of points for best performance is 20.

4.3   Conclusions

In this chapter, an black-box model to determine the maximum in-cylinder pressure has been developed and validated using the data from three SI engines and a GCI engine. Considering the three SI engines, two were turbocharged, one was equipped with WI and LP-EGR systems, and one was a NA. The fourth was a GCI engine that operated in lean conditions and had also a highly variable fuel injection pressure and intake manifold pressure (MAP). Initially, a simple model that used as inputs only load and MFB50 is used (called Simple Model). In some cases where variables such as lambda or Prail or MAP vary significantly, the model has been modified to also add these as inputs (called Complex Model). A self-imposed precision limit of mean validation RMSE of 5% has been used as performance index. This criterion was met during most of the validation of the available data for each engine.

In the first engine (2l Turbocharged GDI SI engine with EGR and WI) the Simple Model demonstrated to be able to reach an accuracy corresponding to a RMSE of 2.6% in the case of mean data and 3.6% in the case of cycle-by-cycle data. These successful validation results indicated the robustness of the Simple Model using as input engine load and MFB50, also in case when EGR and WI were used, without including them as inputs in the model. An additional experimental campaign was carried out with lambda sweeps towards lean mixtures at different SA, which highlighted the need to add lambda as a third input when this variable is used as a control parameter. Using a linear function that depends on lambda and multiplies the Simple Model, the model performance improves obtaining mean validation RMSE is of 2.5% in the case of mean data and 3.3% in the case of cycle-by-cycle data. Additionally, a study on the minimum amount of engine points needed for a calibration of the model that gives best results has been carried out and 20 has been identified as the number of points needed to produce an optimal calibration.

The application of the Simple Model on the second (0.9l Turbocharged SI) and third (1.0L Naturally Aspirated SI) engines, has also confirmed the robustness of this experimental approach. When calibrating a Simple Model for each of these engines separately, the mean validation results obtained have a RMSE of 1.9% for the second engine and 4.6% for the third engine. The reason why the third engine has a significantly higher error than the second one is that, being a NA engine, the values of maximum in-cylinder pressure are almost half of those of the second engine. On both these engines, 20 engine points have also been identified as the minimum amount of engine points needed to produce an optimal calibration with best performance.

On the fourth engine (1.3L Turbocharged GCI), given that no base calibration was present and the behaviour of CI combustion, especially fuelled with gasoline, variables such as lambda, Prail and MAP overgo significant changes and the Simple Model is not capable of complying with the RMSE limit of 5%. Linear corrective functions were added for each of these three variables (Complex Model), identifying MAP as the one with the greatest impact. When using this Complex Model, the model performance increases reaching a

RMSE of 2.6% for mean data and 5.2% for cycle-by-cycle data. In this engine it has also been identified that 20 is the minimum number of data points needed for an optimal calibration with best performance.

5 Conclusions

Knock, high EGT and high in cylinder pressures are the three most limiting factors for an internal combustion engine when trying to increase specific power production and reduce fuel consumption. This work has explored the technologies of WI and LP-EGR that serve to mitigate knock and reduce EGT, and the main novel contribution is the development of mathematical models and a control strategy capable of managing WI and LP-EGR to achieve maximum efficiency by reaching optimal or close to optimal combustion phase. On-board application of such results has always been a primary objective, reason why both the models and the control system have been created with simplicity and low computational requirements as a main goal, allowing for these to be implemented in a production ECU by using already available features such as lookup tables, PI controllers and signal filtering software.

At first, a prototype WI system was used to perform experimental tests that allowed to identify and model the main effects of WI on combustion, which are mainly to lengthen combustion duration (and thus retard combustion phase for a fixed SA) and lower EGT. These models were then used within a control strategy that was specifically designed to mitigate knock and achieve a combustion phase target for improved efficiency. Experimental tests to validate the controller have been carried out, demonstrating its capabilities most specifically when maintaining knock at a certain threshold and combustion phase at a given target. To make the application of the controller possible on board, an algorithm to estimate MFB50 using the accelerometric signal used for knock detection was also developed, obtaining satisfactory results as regards the accuracy needed by the controller. After an assessment of all the experimental work carried out on the WI system, it was concluded that WI is mostly effective for knock mitigation and achievement of stoichiometric operation, especially at high loads, but the high water quantities that are needed when considering these engine points might render the on-board application impractical. This latter statement is mainly based on the fact that the on-board application requires of a water tank that the user should not need to refill very often and also high water/fuel ratios could lead to oil dilution.

A similar analysis is carried out in an engine with a LP-EGR system, identifying the main effects on combustion and modelling them. In this case, the strength of the system when compared to WI was that it does not require any additional fluids like water and it was observed that similar cooling effects could be achieved. On the other hand, being EGR a gas that displaces the fresh air entering the cylinder, it was found that one of the main limitations of the system was that boost pressure had to be increased to maintain a given torque target, aspect that is not present in the case of WI. Experimental work has also been carried out in the search of a synergy between WI and LP-EGR but no synergy was found and the combined effects resulted equal their sum when used separately. A direct comparison was carried out between the traditional approach of mixture enrichment for knock mitigation and EGT cooling versus two stoichiometric calibrations that used WI and EGR respectively. The results demonstrated the great benefits of both technologies in terms of fuel savings

and identified WI as the technology that could achieve higher torque when compared to LP-EGR, because of the beforementioned fresh air displacing effects of LP-EGR.

Regarding the third variable that limits performance, the maximum in-cylinder pressure, a virtual sensor was developed and validated to be able to estimate this parameter on a cycle-by-cycle basis. For this, experimental work on a wide variety of engines was carried out, ranging from several turbocharged and naturally aspirated GDI engines to a GCI engine, demonstrating the wide applicability of the virtual sensor.

The various methods and models identified during the application of WI and LP-EGR systems as well as the Pmax virtual sensor have been validated on a wide variety of GDI engines, demonstrating the ample validity of these. As stated on the previous sections, each model requires a specific calibration for each engine and a general calibration that covers them all is not possible. At the same time, this work has also elaborated guidelines on how to reduce to a minimum the experimental work needed for calibration while ensuring the best model performance.

The result of this work has generated a wide variety of solutions that can be implemented on-board and contribute to the development of systems, models and control strategies that help reduce fuel consumption and comply with the current demands of the automotive industry. Considering the observed potential of the technologies that have been investigated in this work, it can be said that the research and development of ICEs is still highly relevant to the automotive industry and the world of mobility. ICEs do not necessarily have to be replaced by an electric alternative but can coexist with them to further overcome the economic and environmental challenges that a pure combustion or pure electric solution implies.

Bibliography

1. Khatri, J., Denbratt, I., Dahlander, P., and Koopmans, L., "Water Injection Benefits in a 3-Cylinder Downsized SI-Engine," 2019-01–0034, 2019, doi:10.4271/2019-01-0034.

2. Johnson, T.V., "Review of Vehicular Emissions Trends," *SAE Int. J. Engines* 8(3):1152–1167, 2015, doi:10.4271/2015-01-0993.

3. Liang, X., Wang, Y., Chen, Y., and Deng, S., "Advances in Emission Regulations and Emission Control Technologies for Internal Combustion Engines," *SAE Int. J. Sustain. Transp. Energy Environ. Policy* 2(2):13-02-02–0007, 2021, doi:10.4271/13-02-02-0007.

4. Police, G., Diana, S., Giglio, V., Iorio, B., and Rispoli, N., "Downsizing of SI Engines by Turbo-Charging," *Volume 4: Fatigue and Fracture, Heat Transfer, Internal Combustion Engines, Manufacturing, and Technology and Society*, ASMEDC, Torino, Italy, ISBN 978-0-7918-4251-5: 463–476, 2006, doi:10.1115/ESDA2006-95215.

5. Jung, D., Lee, B., Son, J., Woo, S., and Kim, Y., "Development of Gasoline Direct Injection Engine for Improving Brake Thermal Efficiency Over 44%," *J. Eng. Gas Turbines Power* 142(10):101005, 2020, doi:10.1115/1.4048152.

6. Lumsden, G., OudeNijeweme, D., Fraser, N., and Blaxill, H., "Development of a Turbocharged Direct Injection Downsizing Demonstrator Engine," *SAE Int. J. Engines* 2(1):1420–1432, 2009, doi:10.4271/2009-01-1503.

7. Sawant, P. and Bari, S., "Effects of Variable Intake Valve Timings and Valve Lift on the Performance and Fuel Efficiency of an Internal Combustion Engine," SAE Technical Paper: 2018-01–0376, 2018, doi:10.4271/2018-01-0376.

8. Knop, V. and Essayem, E., "Comparison of PFI and DI Operation in a Downsized Gasoline Engine," *SAE Int. J. Engines* 6(2):941–952, 2013, doi:10.4271/2013-01-1103.

9. Ferrey, P., Miehe, Y., Constensou, C., and Collee, V., "Potential of a Variable Compression Ratio Gasoline SI Engine with Very High Expansion Ratio and Variable Valve Actuation," *SAE Int. J. Engines* 7(1):468–487, 2014, doi:10.4271/2014-01-1201.

10. Schalk, C., "The 10 big problems with simply replacing fossil cars with electric," 2021.

11. Khan, A.F., Burluka, A., Neumeister, J., OudeNijeweme, D., Freeland, P., and Mitcalf, J., "Combustion and Autoignition Modelling in a Turbocharged SI Engine," *SAE Int. J. Engines* 9(4):2079–2090, 2016, doi:10.4271/2016-01-2234.

12. Ito, N., Ohta, T., Kono, R., Arikawa, S., and Matsumoto, T., "Development of a 4-Cylinder Gasoline Engine with a Variable Flow Turbo-charger," SAE Technical Paper: 2007-01–0263, 2007, doi:10.4271/2007-01-0263.

13. Ceschini, L., Morri, A., Balducci, E., Cavina, N., Rojo, N., Calogero, L., and Poggio, L., "Experimental observations of engine piston damage induced by knocking combustion," *Mater. Des.* 114:312–325, 2017, doi:10.1016/j.matdes.2016.11.015.

14.   Kumano, K. and Yamaoka, S., "Analysis of Knocking Suppression Effect of Cooled EGR in Turbo-Charged Gasoline Engine," SAE Technical Paper: 2014-01–1217, 2014, doi:10.4271/2014-01-1217.

15.   Siokos, K., Koli, R., Prucka, R., Schwanke, J., and Miersch, J., "Assessment of Cooled Low Pressure EGR in a Turbocharged Direct Injection Gasoline Engine," *SAE Int. J. Engines* 8(4):1535–1543, 2015, doi:10.4271/2015-01-1253.

16.   Lu, H., Deng, J., Hu, Z., Wu, Z., Li, L., Yuan, F., Xie, D., Yuan, S., and Shen, Y., "Study on Fuel Economy Improvement by Low Pressure Water-Cooled EGR System on a Downsized Boosted Gasoline Engine," SAE Technical Paper: 2016-01–0678, 2016, doi:10.4271/2016-01-0678.

17.   Zembi, J., Battistoni, M., Ranuzzi, F., Cavina, N., and De Cesare, M., "CFD Analysis of Port Water Injection in a GDI Engine under Incipient Knock Conditions," *Energies* 12(18):3409, 2019, doi:10.3390/en12183409.

18.   Paltrinieri, S., Mortellaro, F., Silvestri, N., Rolando, L., Medda, M., and Corrigan, D., "Water Injection Contribution to Enabling Stoichiometric Air-to-Fuel Ratio Operation at Rated Power Conditions of a High-Performance DISI Single Cylinder Engine," SAE Technical Paper: 2019-24–0173, 2019, doi:10.4271/2019-24-0173.

19.   Cordier, M., Lecompte, M., Malbec, L.-M., Reveille, B., Servant, C., Souidi, F., and Torcolini, N., "Water Injection to Improve Direct Injection Spark Ignition Engine Efficiency," SAE Technical Paper: 2019-01–1139, 2019, doi:10.4271/2019-01-1139.

20.   Cavina, N., Rojo, N., Businaro, A., Brusa, A., Corti, E., and De Cesare, M., "Investigation of Water Injection Effects on Combustion Characteristics of a GDI TC Engine," *SAE Int. J. Engines* 10(4):2209–2218, 2017, doi:10.4271/2017-24-0052.

21.   Görgen, M., Balazs, D.A., Nijs, D.M., Lehn, H., Scharf, D.J., Thewes, D.M., Böhmer, D.M., Alt, D.N., Claßen, J., and Sterlepper, S., "NEW LAMBDA = 1 GASOLINE POWERTRAINS NEW TECHNOLOGIES AND THEIR INTERACTION WITH CONNECTED AND AUTONOMOUS DRIVING," 16, 2018.

22.   Rodríguez, F., "Recommendations for post-Euro 6 standards for light-duty vehicles in the European Union," 54.

23.   Netzer, C., Franken, T., Seidel, L., Lehtiniemi, H., and Mauss, F., "Numerical Analysis of the Impact of Water Injection on Combustion and Thermodynamics in a Gasoline Engine Using Detailed Chemistry," *SAE Int. J. Engines* 11(6):1151–1166, 2018, doi:10.4271/2018-01-0200.

24.   Choi, M., Kwak, Y.-H., Roth, D.B., Jakiela, D., and Song, J., "Synergies of Cooled External EGR, Water Injection, Miller Valve Events and Cylinder Deactivation for the Improvement of Fuel Economy on a Turbocharged-GDI Engine; Part 2, Engine Testing," SAE Technical Paper: 2019-01–0242, 2019, doi:10.4271/2019-01-0242.

25.   Falfari, S., Bianchi, G.M., Cazzoli, G., Ricci, M., and Forte, C., "Water Injection Applicability to Gasoline Engines: Thermodynamic Analysis," SAE Technical Paper: 2019-01–0266, 2019, doi:10.4271/2019-01-0266.

26.   Berni, F., Breda, S., D'Adamo, A., Fontanesi, S., and Cantore, G., "Numerical Investigation on the Effects of Water/Methanol Injection as Knock Suppressor to Increase the Fuel Efficiency of a Highly Downsized GDI Engine," SAE Technical Paper: 2015-24–2499, 2015, doi:10.4271/2015-24-2499.

27.   Rahimi Boldaji, M., Sofianopoulos, A., Mamalis, S., and Lawler, B., "Effects of Mass, Pressure, and Timing of Injection on the Efficiency and Emissions Characteristics of TSCI Combustion with Direct Water Injection," SAE Technical Paper: 2018-01–0178, 2018, doi:10.4271/2018-01-0178.

28.   Pauer, T., Frohnmaier, M., Walther, J., Schenk, P., Hettinger, A., and Kampmann, S., "Optimierung von Ottomotoren durch Wassereinspritzung/Optimization of Gasoline Engines by Water Injection," in: Lenz, H. P., ed., *37th Internationales Wiener Motorensymposium*, 1st ed., VDI Verlag, Düsseldorf, ISBN 978-3-18-679912-8: II–18, 2016, doi:10.51202/9783186799128-II-18.

29.   Hoppe, F., Thewes, M., Seibel, J., Balazs, A., and Scharf, J., "Evaluation of the Potential of Water Injection for Gasoline Engines," *SAE Int. J. Engines* 10(5):2500–2512, 2017, doi:10.4271/2017-24-0149.

30.   Barros, S., Atkinson, W., and Piduru, N., "Extraction of Liquid Water from the Exhaust of a Diesel Engine," SAE Technical Paper: 2015-01–2806, 2015, doi:10.4271/2015-01-2806.

31.   Bargende, M., Reuss, H.-C., and Wiedemann, J., eds., "17. Internationales Stuttgarter Symposium: Automobil- und Motorentechnik," Springer Vieweg, Wiesbaden [Heidelberg], ISBN 978-3-658-16987-9, 2017.

32.   Energy and thermal management, air conditioning, waste heat recovery, Springer Berlin Heidelberg, New York, NY, ISBN 978-3-319-47195-2, 2016.

33.   Worm, J., Naber, J., Duncan, J., Barros, S., and Atkinson, W., "Water Injection as an Enabler for Increased Efficiency at High-Load in a Direct Injected, Boosted, SI Engine," *SAE Int. J. Engines* 10(3):951–958, 2017, doi:10.4271/2017-01-0663.

34.   Iacobacci, A., Marchitto, L., and Valentino, G., "Water Injection to Enhance Performance and Emissions of a Turbocharged Gasoline Engine under High Load Condition," *SAE Int. J. Engines* 10(3):928–937, 2017, doi:10.4271/2017-01-0660.

35.   Ranuzzi, F., Cavina, N., Brusa, A., De Cesare, M., and Panciroli, M., "Development and Software in the Loop Validation of a Model-based Water Injection Combustion Controller for a GDI TC Engine," SAE Technical Paper: 2019-01–1174, 2019, doi:10.4271/2019-01-1174.

36.   Ranuzzi, F., Cavina, N., Scocozza, G., Brusa, A., and De Cesare, M., "Experimental Validation of a Model-Based Water Injection Combustion Control System for On-Board Application," SAE Technical Paper: 2019-24–0015, 2019, doi:10.4271/2019-24-0015.

37.   Scocozza, G.F., Cavina, N., De Cesare, M., Panciroli, M., and Benedetti, C., "Experimental Investigation on the Effects of Cooled Low Pressure EGR and Water Injection on Combustion of a Turbocharged GDI Engine," SAE Technical Paper: 2020-24–0003, 2020, doi:10.4271/2020-24-0003.

38.   Battistoni, M., Grimaldi, C.N., Cruccolini, V., Discepoli, G., and De Cesare, M., "Assessment of Port Water Injection Strategies to Control Knock in a GDI Engine through Multi-Cycle CFD Simulations," SAE Technical Paper: 2017-24–0034, 2017, doi:10.4271/2017-24-0034.

39.   Finesso, R., Spessa, E., Yang, Y., Alfieri, V., and Conte, G., "HRR and MFB50 Estimation in a Euro 6 Diesel Engine by Means of Control-Oriented Predictive Models," *SAE Int. J. Engines* 8(3):1055–1068, 2015, doi:10.4271/2015-01-0879.

40.   Finesso, R. and Spessa, E., "A Feed-Forward Approach for the Real-Time Estimation and Control of MFB50 and SOI In Diesel Engines," *SAE Int. J. Engines* 7(1):528–549, 2014, doi:10.4271/2014-01-9046.

41.   Xiao, B., Wang, S., and Prucka, R.G., "A Semi-Physical Artificial Neural Network for Feed Forward Ignition Timing Control of Multi-Fuel SI Engines," SAE Technical Paper: 2013-01–0324, 2013, doi:10.4271/2013-01-0324.

42.   Hillion, M., Chauvin, J., and Petit, N., "Open-loop combustion timing control of a Spark-Ignited engine," *2008 47th IEEE Conference on Decision and Control*, IEEE, Cancun, Mexico, ISBN 978-1-4244-3123-6: 5635–5642, 2008, doi:10.1109/CDC.2008.4739262.

43.   Finesso, R., Spessa, E., Yang, Y., Conte, G., and Merlino, G., "Neural-Network Based Approach for Real-Time Control of BMEP and MFB50 in a Euro 6 Diesel Engine," SAE Technical Paper: 2017-24–0068, 2017, doi:10.4271/2017-24-0068.

44.   Shahlari, A.J. and Ghandhi, J.B., "A Comparison of Engine Knock Metrics," SAE Technical Paper: 2012-32–0007, 2012, doi:10.4271/2012-32-0007.

45.   Siano, D., Panza, M.A., and D'Agostino, D., "Knock Detection Based on MAPO Analysis, AR Model and Discrete Wavelet Transform Applied to the In-Cylinder Pressure Data: Results and Comparison," *SAE Int. J. Engines* 8(1):1–13, 2014, doi:10.4271/2014-01-2547.

46.   Leppard, W.R., "Individual-Cylinder Knock Occurence and Intensity in Multicylinder Engines," SAE Technical Paper: 820074, 1982, doi:10.4271/820074.

47.   De Bellis, V., Teodosio, L., Siano, D., Minarelli, F., and Cacciatore, D., "Knock and Cycle by Cycle Analysis of a High Performance V12 Spark Ignition Engine. Part 1: Experimental Data and Correlations Assessment," *SAE Int. J. Engines* 8(5):1993–2001, 2015, doi:10.4271/2015-24-2392.

48.   Corti, E., Forte, C., Bianchi, G.M., and Zoffoli, L., "A Control-Oriented Knock Intensity Estimator," *SAE Int. J. Engines* 10(4):2219–2229, 2017, doi:10.4271/2017-24-0055.

49.   Potteau, S., Lutz, P., Leroux, S., Moroz, S., and Tomas, E., "Cooled EGR for a Turbo SI Engine to Reduce Knocking and Fuel Consumption," SAE Technical Paper: 2007-01–3978, 2007, doi:10.4271/2007-01-3978.

50.   Tang, Q., Liu, J., Zhan, Z., and Hu, T., "Influences on Combustion Characteristics and Performances of EGR vs. Lean Burn in a Gasoline Engine," SAE Technical Paper: 2013-01–1125, 2013, doi:10.4271/2013-01-1125.

51.   Varde, K.S. and Manoharan, N.K., "Characterization of Exhaust Emissions in a SI Engine using E85 and Cooled EGR," SAE Technical Paper: 2009-01–1952, 2009, doi:10.4271/2009-01-1952.

52.   Svensson, E., Yin, L., Tunestal, P., and Tuner, M., "Combined Low and High Pressure EGR for Higher Brake Efficiency with Partially Premixed Combustion," SAE Technical Paper: 2017-01–2267, 2017, doi:10.4271/2017-01-2267.

53.   Chao, Y., Lu, H., Hu, Z., Deng, J., Wu, Z., Li, L., Shen, Y., and Yuan, S., "Comparison of Fuel Economy Improvement by High and Low Pressure EGR System on a Downsized Boosted Gasoline Engine," SAE Technical Paper: 2017-01–0682, 2017, doi:10.4271/2017-01-0682.

54.   Alger, T., Gukelberger, R., Gingrich, J., and Mangold, B., "The Impact of Cooled EGR on Peak Cylinder Pressure in a Turbocharged, Spark Ignited Engine," *SAE Int. J. Engines* 8(2):455–463, 2015, doi:10.4271/2015-01-0744.

55.	Kathirvelu, B. and Subramanian, S., "Performance and emission characteristics of biodiesel blends in a premixed compression ignition engine with exhaust gas recirculation," *Environ. Eng. Res.* 22(3):294–301, 2017, doi:10.4491/eer.2016.145.

56.	Hosseini, V. and Checkel, M.D., "Using Reformer Gas to Enhance HCCI Combustion of CNG in a CFR Engine," 2006-01–3247, 2006, doi:10.4271/2006-01-3247.

57.	Chen, L., Stone, R., and Richardson, D., "Effect of the valve timing and the coolant temperature on particulate emissions from a gasoline direct-injection engine fuelled with gasoline and with a gasoline–ethanol blend," *Proc. Inst. Mech. Eng. Part J. Automob. Eng.* 226(10):1419–1430, 2012, doi:10.1177/0954407012444966.

58.	Zhu, Q., Wang, S., Prucka, R., Prucka, M., and Dourra, H., "Model-Based Control-Oriented Combustion Phasing Feedback for Fast CA50 Estimation," *SAE Int. J. Engines* 8(3):997–1004, 2015, doi:10.4271/2015-01-0868.

59.	Johnson, R., Kaczynski, D., Zeng, W., Warey, A., Grover, R., and Keum, S., "Prediction of Combustion Phasing Using Deep Convolutional Neural Networks," SAE Technical Paper: 2020-01–0292, 2020, doi:10.4271/2020-01-0292.

60.	Aengeby, J., "Closed Loop Control of the Combustion Phase in SI Engines Using Alternative Fuels," *SAE Int. J. Adv. Curr. Pract. Mobil.* 3(1):312–319, 2020, doi:10.4271/2020-01-2088.

61.	Wang, S., Prucka, R., Zhu, Q., Prucka, M., and Dourra, H., "A Real-Time Model for Spark Ignition Engine Combustion Phasing Prediction," *SAE Int. J. Engines* 9(2):1180–1190, 2016, doi:10.4271/2016-01-0819.

62.	Zhu, Q., Prucka, R., Wang, S., Prucka, M., and Dourra, H., "Model-Based Optimal Combustion Phasing Control Strategy for Spark Ignition Engines," *SAE Int. J. Engines* 9(2):1170–1179, 2016, doi:10.4271/2016-01-0818.

63.	Businaro, A., Cavina, N., Corti, E., Mancini, G., Moro, D., Ponti, F., and Ravaglioli, V., "Accelerometer Based Methodology for Combustion Parameters Estimation," *Energy Procedia* 81:950–959, 2015, doi:10.1016/j.egypro.2015.12.152.

64.	Amezcua, E.R., Maldonado, B., Rothamer, D., Kim, K., Kweon, C.-B., and Stefanopoulou, A., "Accelerometer-Based Estimation of Combustion Features for Engine Feedback Control of Compression-Ignition Direct-Injection Engines," 2020-01–1147, 2020, doi:10.4271/2020-01-1147.

65.	Ponti, F., Ravaglioli, V., Corti, E., Moro, D., and De Cesare, M., "Remote Combustion Sensing Methodology for Non-Intrusive Cylinder Pressure Estimation in Diesel Engines," *IFAC Proc. Vol.* 46(21):353–359, 2013, doi:10.3182/20130904-4-JP-2042.00039.

66.	Nates, R.J. and Yates, A.D.B., "Knock Damage Mechanisms in Spark-Ignition Engines," 942064, 1994, doi:10.4271/942064.

67.	Brusa, A., Cavina, N., Rojo, N., Cucchi, M., and Silvestri, N., "Development and Validation of a Control-Oriented Analytic Engine Simulator," SAE Technical Paper: 2019-24–0002, 2019, doi:10.4271/2019-24-0002.

68.	Panzani, G., Ostman, F., and Onder, C.H., "Engine Knock Margin Estimation Using In-Cylinder Pressure Measurements," *IEEEASME Trans. Mechatron.* 22(1):301–311, 2017, doi:10.1109/TMECH.2016.2604920.

69.   Cavina, N., Brusa, A., Rojo, N., and Corti, E., "Statistical Analysis of Knock Intensity Probability Distribution and Development of 0-D Predictive Knock Model for a SI TC Engine," 2018-01–0858, 2018, doi:10.4271/2018-01-0858.

70.   Brusa, A., Cavina, N., Rojo, N., Mecagni, J., Corti, E., Ravaglioli, V., Cucchi, M., and Silvestri, N., "Development and Experimental Validation of an Adaptive, Piston-Damage-Based Combustion Control System for SI Engines: Part 1—Evaluating Open-Loop Chain Performance," *Energies* 14(17):5367, 2021, doi:10.3390/en14175367.

71.   Brusa, A., Cavina, N., Rojo, N., Mecagni, J., Corti, E., Moro, D., Cucchi, M., and Silvestri, N., "Development and Experimental Validation of an Adaptive, Piston-Damage-Based Combustion Control System for SI Engines: Part 2—Implementation of Adaptive Strategies," *Energies* 14(17):5342, 2021, doi:10.3390/en14175342.

72.   Kulah, S., Donkers, T., and Willems, F., "Virtual Cylinder Pressure Sensor for Transient Operation in Heavy-Duty Engines," *SAE Int. J. Engines* 8(3):1029–1040, 2015, doi:10.4271/2015-01-0872.

73.   Rugland, C. and Stenlaas, O., "Knock Sensor Based Virtual Cylinder Pressure Sensor," 2019-01–0040, 2019, doi:10.4271/2019-01-0040.

74.   Bellone, M., Faghani, E., and Karayiannidis, Y., "Comparison of CNN and LSTM for Modeling Virtual Sensors in an Engine," SAE Technical Paper: 2020-01–0735, 2020, doi:10.4271/2020-01-0735.

75.   Jorques Moreno, C., Stenlaas, O., and Tunestal, P., "Cylinder Pressure-Based Virtual Sensor for In-Cycle Pilot Mass Estimation," *SAE Int. J. Engines* 11(6):1167–1182, 2018, doi:10.4271/2018-01-1163.

76.   Scocozza, G.F., Silvagni, G., Brusa, A., Cavina, N., Ponti, F., Ravaglioli, V., De Cesare, M., Panciroli, M., and Benedetti, C., "Development and Validation of a Virtual Sensor for Estimating the Maximum in-Cylinder Pressure of SI and GCI Engines," SAE Technical Paper: 2021-24–0026, 2021, doi:10.4271/2021-24-0026.